

UC Berkeley

UC Berkeley Electronic Theses and Dissertations

Title

Characterization of Calcium (Alumino)Silicate Hydrate Phases with Synchrotron-Based Techniques

Permalink

<https://escholarship.org/uc/item/9v01t3bx>

Author

Li, Jiaqi

Publication Date

2019

Peer reviewed|Thesis/dissertation

Characterization of Calcium (Alumino)Silicate Hydrate Phases with Synchrotron-Based
Techniques

By

Jiaqi Li

A dissertation submitted in partial satisfaction of the
requirements for the degree of

Doctor of Philosophy

in

Engineering - Civil and Environmental Engineering

in the

Graduate Division

of the

University of California, Berkeley

Committee in charge:

Professor Paulo J. M. Monteiro, Chair
Professor Shaofan Li
Professor Hans-Rudolf Wenk

Fall 2019

Abstract

Characterization of Calcium (Alumino)Silicate Hydrate Phases with Synchrotron-Based Techniques

by

Jiaqi Li

Doctor of Philosophy in Civil and Environmental Engineering

University of California, Berkeley

Professor Paulo J.M. Monteiro, Chair

Concrete is the most consumed manufactured commodity by mass in the world. The manufacturing of Portland cement, the binder of modern concrete, is responsible for 8-9% of global anthropogenic carbon dioxide (CO₂) emission, and 2-3% of primary energy consumption. Study of green cement and concrete can provide efficient solutions to reduce the environmental burden of this commodity in the construction industry.

Most concrete is produced using calcium silicate hydrate (C-S-H)-based binder. Understanding the structure of C-S-H based phases is essential to designing a more sustainable cement and concrete. Dicalcium silicate (C₂S) is a common clinker compound in both Portland cement and belite-ye'elite-ferrite cement. The formation of C₂S is less energy intensive and yields less CO₂. C-S-H is the primary hydration product in hydrated C₂S. Incorporation of aluminum-rich industrial by-product is a common method to reduce the environmental impact of concrete production, the principal binding phase of this blended cement-based concrete is calcium aluminosilicate hydrate (C-A-S-H). Sodium hydroxide and sodium silicate activated ground granulated blast-furnace slag are promising cementitious materials alternative to Portland cement due to their lower CO₂ emission, the principal binding phase in these alkali-activated materials is sodium incorporated calcium aluminosilicate hydrate (C-N-A-S-H).

This thesis aims to understand different calcium (alumino)silicate hydrates at multi-scale. The characterization of C-S-H and its derivatives, C-A-S-H and sodium incorporated calcium (alumino) silicate hydrate (C-N-(A-)S-H), is reported. There are three main gaps in the current state-of-the art that need to be investigated: (1) β -C₂S is the most common C₂S polymorph in cement, yet the hydration of other polymorphs (e.g., α' _H-C₂S) has rarely been studied, the molecular structure of C-S-H in hydrated α' _H-C₂S has not been reported; (2) the structure of synthetic C-S-H has extensively studied, however the influences of aluminum incorporation on the coordination environment of Ca and Si in C-A-S-H have not been well understood; (3) the influences of calcium to silicate molar ratio and aluminum induced cross-linking sites on the nanomechanical properties C-S-H have been understood. However, the molecular structure and influence of sodium incorporation of nanomechanical properties of C-N-(A-)S-H have not been resolved.

The studies described in this thesis uses synchrotron radiation-based X-ray techniques to provide new information of the above-mentioned questions. X-ray spectromicroscopy coupled with soft

X-ray ptychographic imaging is used to compare the hydration of two polymorphs of dicalcium silicate (β -C₂S and α' _H-C₂S) and to determine the structure of hydration product C-S-H at atomic to microscale. The coordination environments of Ca and Si of C-S-H in the hydrated C₂S are studied. Wide-angle X-ray scattering, X-ray spectromicroscopy, and soft X-ray ptychographic imaging are utilized to investigate the atomic to micro-structure of C-S-H and C-A-S-H. The influences of Ca/Si and Al/Si ratios on the coordination chemistry and morphology of C-A-S-H are investigated. High-pressure X-ray diffraction is used to investigate the anisotropic mechanical properties of sodium incorporate C-S-H and C-A-S-H.

The experimental results indicated that C-S-H formed in hydrated β -C₂S and α' _H-C₂S exhibited similar coordination symmetry of Ca. The silicate chains of C-S-H formed in hydrated α' _H-C₂S polymerize faster than those in hydrated β -C₂S. The aluminum incorporation has no significant influences on the coordination symmetry of Ca of synthetic C-S-Hs, while aluminum incorporation increases their silicate polymerization. The morphology of synthetic C-(A-)S-Hs at the nanoscale is independent of the aluminum incorporation and their Ca/Si ratio at temperature of 7-50 °C. The foil of C-A-S-H is significantly coarser at synthesis temperature of 80 °C. Under hydrostatic pressure up to ~10 GPa, the sodium incorporated C-A-S-H exhibit significantly higher incompressibility along the c-axis than sodium incorporated C-S-H and alkali-free C-A-S-H along the c-axis. The experimental results in this thesis improve the understanding of the chemistry of C-S-H and its derivatives (C-A-S-H and C-N-(A-)S-H). The work is important for providing evidence to design high-performance C-S-H based concrete using a bottom-up approach.

Table of Contents

1.Introduction.....	1
1.1 Challenges in cement industry	1
1.2 Structure of this thesis.....	2
1.3 References.....	3
2. A Brief literature review	6
2.1 Portland cement	6
2.2 Calcium aluminosilicate hydrate- a binding phase in hardened blended Portland cement concrete	9
2.3 Alkali incorporated calcium (alumino) silicate hydrate- a binding phase in hardened concrete	12
2.4 References.....	14
3.Materials and methods	21
3.1 Materials	21
3.2 Experimental methods	22
3.3 References.....	24
4. Hydration of belite polymorphs.....	26
4.1 Ca coordination of anhydrous β -C ₂ S and hydrated β -C ₂ S at 17 days.....	26
4.2. Ca coordination of anhydrous α' _H -C ₂ S and hydrated α' _H -C ₂ S at 10 days	29
4.3 Si environment of anhydrous β -C ₂ S and hydrated β -C ₂ S at 17 days.....	31
4.4 Si environment of hydrated β -C ₂ S for 51 days	34
4.5 Si environment of anhydrous and hydrated α' _H -C ₂ S for 10 days	36
4.6 Si environment of hydrated α' _H -C ₂ S for 40 days.....	38
4.7 Conclusions.....	40
4.8 References.....	41
5.Chemistry and structure of calcium (alumino) silicate hydrate.....	45
5.1 Ca coordination of calcium (alumino) silicate hydrate.....	45
5.2 Chemical environment of Si	51
5.3 Morphology of C-(A-)S-H.....	58
5.4 A molecular-to-nanoscale model of C-A-S-H	66

5.5 Conclusion	68
5.6 References.....	68
6.Mechanical properties of alkali incorporated C-(A-)S-H	73
6.1 HP-XRD of alkali incorporated C-(A-)S-H.....	73
6.2 Conclusions.....	80
6.3 References.....	81
7. Concluding Remarks	83
8.Appendix.....	85
8.1 Supplementary images and algorithm.....	85
8.2 References.....	87

Acknowledgement

I would like to express my deepest appreciation to my advisor, Prof. Paulo J.M. Monteiro, who offered the greatest opportunity in my academic career. His insightful advices, warm encouragement, and continuous support to me are invaluable.

I appreciate the valuable information regarding mineralogy and crystallography from Prof. Hans-Rudolf Wenk throughout my PhD study. I have also greatly benefited from Dr. Guoqing Geng and Dr. Rupert Myers starting from my early PhD study.

I sincerely appreciate the considerable research support from Prof. Roya Maboudian, Prof. Carlo Carlos, Jiahao Zhu, Xiaokun Lv, and David Gardner in the College of Chemistry.

I'm grateful to the following researchers at the Advanced Light Source for providing technical support and insightful advises: Dr. Matthew Marcus, Dr. Martin Kunz, Dr. Jinyuan Yan, Dr. David Kilcoyne, Dr. David Shapiro, and Dr. Young-Sang Yu.

I greatly acknowledge people in the materials group at Berkeley for valuable discussion and help: Wenxin Zhang, Dr. Cruz Carlos Jr., Dr. Carlos Orozco Rios, Daniela Martinez Lopez, Dr. Kemal Celik, Juan Carvajal Vinasco, Dr. Will Nguyen, Dr. Rotana Hay, Dr. Jacob Duncan, Dr. Parham Aghdasi, Chen Li, and Panod Viseshchitra.

I would like to express my gratitude to the following researchers from the European cement community for their valuable samples and discussion: Dr. Delphine Marchon, Dr. Barbara Lothenbach, and Dr. Krassimir Garbev.

Lastly, I would like to express my thanks to my parents for everything.

1.Introduction

1.1 Challenges in cement industry

Concrete is the second most consumed material in the world by mass after water [1]. Portland cement (PC) is the main binder of concrete, the annual production of PC was about 4.1 billion metric tonnes in 2017 according to United States Geological Survey [2]. Considering typical material constituents in PC-based modern concrete [3], the yearly consumption of concrete is at least 26 billion metric tonnes, which is also attributed to yearly consumption of about 19 billion metric tonnes of aggregate and about 2-3 billion metric tonnes of fresh water. The considerable consumption of raw materials and associated massive production result in significant environmental impacts globally.

PC manufacturing dominates the environmental impact (e.g., CO₂ emission) and primary energy use among all process in concrete production [4]. The CO₂ emission of PC manufacturing per metric tonne amounts to about 0.8 metric tonne due to its high calcination temperature (~1450 °C) and decomposition of limestone (mainly calcium carbonate) in the raw materials [5]. Due to the massive production of PC, the manufacture of PC approximately contributes to 8-9% anthropogenic CO₂ emission and 2-3% primary energy consumption [6]. Thus, the construction community is under increasing pressure to lower the environmental impact of PC and PC-based concrete productions.

To tackle this environmental challenge from concrete production, both the industry and scientific communities currently look for solutions to lowering the environmental impact of the binder used in concrete. Calcium silicate hydrate (C-S-H), the principal binding phase, in PC concrete is a reaction product between water and calcium silicate compounds (tricalcium silicate (Ca₃SiO₅, also termed C₃S, following the cement chemistry notation where C=CaO, S=SiO₂, A=Al₂O₃, H=H₂O, N=Na₂O, and K=K₂O) and dicalcium silicate (Ca₂SiO₄, also termed C₂S; or belite as stoichiometric impure C₂S)) [7]. Although the hydration of C₃S and C₂S both yield C-S-H, the formation of C₃S generates more CO₂ than that of C₂S (579 kg/tonne for C₃S versus 512 kg/tonne for C₂S) [8]. Production of C₂S-rich PC at the expense of C₃S is an approach to reducing the environmental impact of PC manufacturing since the formation of C₂S yields less CO₂ than that of C₃S [9]. In addition, belite-ye'elinite-ferrite (BYF) cement is a promising alternative to PC since the manufacturing of BYF lowers 30% of CO₂ emission and 20% of primary energy consumption relative to those of PC [10]. The roles of belite in designing green PC-based cementitious materials and BYF cement-based materials are both significant [11]. However, the hydration of belite, particularly the more reactive polymorph α_H-C₂S is not well understood. The lack of understanding of belite hydration limits the development of belite-rich cements.

Partial replacement of PC clinker by supplementary cementitious materials (SCMs) is the most common strategy to reduce the environmental impact of the manufacture of concrete [12]. These SCMs are mainly human-made (industrial by-products) or naturally-occurring amorphous (alumino)silicates [13]. The most widely used SCMs are ground granulated blast-furnace slag (GGBFS) and fly ash (FA) [14] [15]. The principal binding phase in GGBFS and/or FA

incorporated PC-based concrete is calcium (alumino) silicate hydrate (C-(A-)S-H) [16], a poorly crystalline phase with variable chemical compositions [17, 18]. Despite that many atomic simulations and bulk characterizations of C-A-S-H have been reported [19-23], its chemistry and structure were rarely investigated at the nano-scale. The lack of chemical and structural information of C-A-S-H at the nano-scale restricts the understanding and designing of C-A-S-H-based cementitious materials and limits the substitution level of SCMs in PC-based concrete.

Unlike the above-mentioned conventional clinker-based cementitious materials, which requires high calcination temperature (i.e., above 1200 °C) during clinker manufacturing, alkali-activated materials (AAMs) are mainly made of mixing alkali activator solutions or solid with (calcium) aluminosilicate solid precursors (e.g., GGBFS and FA), typically at evaluated temperature (e.g., 50-80 °C) [24, 25]. Moreover, the solid precursor in AAM can be completely waste-stream materials [26]. The CO₂ emission during the production of AAMs-based concrete is approximately 80% lower compared to that of PC concrete [10]. Alkali incorporated calcium alumino silicate hydrate (e.g., sodium incorporated calcium (alumino) silicate hydrate, termed as C-N-(A-)S-H) is one of the main binding phases of AAMs, in addition to sodium alumino silicate (hydrate) gel [27]. There is a burgeoning interest in the characterization and development of AAMs since the mechanical properties and durability of AAMs are both comparable to or higher than those of PC-based cementitious materials [28]. The reported superior mechanical properties of porous AAMs have been experimentally determined at the micro-to-macro scales and simulated at molecular scale [29-31]. The mechanical properties of pore-free alkali incorporated C-A-S-H has not been experimentally validated yet. The lack of experimental evidence at molecular-to-nano scale restricts the design and understanding of AAMs. Such missing gap should be filled before modelling more realistic molecular structures of alkali incorporated C-A-S-H.

The issues stated above are representative challenges that limit the understanding and design of modern green cementitious materials at a fundamental level. Despite their significance in the development of green C-S-H-based cementitious materials [32], the insight in chemistry, structure, and mechanical properties of calcium (sodium) (alumino)silicate hydrate (C-(N)-(A-)S-H) phase is needed to be investigated at nano and atomistic scale. Therefore, to tackle the current environmental challenges of the cement industry, synchrotron radiation-based X-ray techniques are applied to solve the above-mentioned issues, which are difficult to be addressed using conventional experimental techniques. The success in the use of these state-of-the-art techniques can advance a deeper understanding of the structure and performance of C-S-H based construction materials and contributes to the development of green cementitious materials.

1.2 Structure of this thesis

This thesis aims to develop a more fundamental understanding of the chemistry of green construction materials, with a particular focus on C-S-Hs based cementitious materials. The understanding of the chemistry and nanostructure of the C-S-H based materials is achieved by the use of synchrotron-based X-ray techniques. The new insights of the chemistry and nanostructure of C-S-H and its derivatives unveiled in this work may inspire the prospective studies on the advances in cement chemistry as well as the development of green cementitious

materials. This work is presented in three chapters in addition to the literature review summarized in Chapter 2.

Chapter 3 presents an overview of the materials and experimental methodologies used in this thesis. Detailed descriptions of the samples used in the thesis, C₂S and laboratory-synthesized C-S-H, C-A-S-H, and C-N-(A-)S-H products, are presented.

Chapter 4 describes the hydration of two C₂S polymorphs using X-ray scanning transmission x-ray microscopy (STXM) coupled with soft X-ray ptychographic imaging. The work aims to understand the Ca coordination of C-S-H in two hydrated C₂S polymorphs and their local change in the coordination environment of Si in C-S-H (inner and outer products).

Chapter 5 presents the structure of C-(A-)S-H at the atomic, nano-, and micro scales also mainly using STXM and with soft X-ray ptychographic imaging. The experimental study aims to understand the influences of Ca/Si molar ratio, aluminum incorporation, and equilibrium temperature on the structure of C-S-H. The potential speciation of the third aluminate hydrate in C-A-S-H is discussed.

Chapter 6 presents the HP-XRD results that are used to determine the influence of alkali incorporation on the mechanical properties of C-(A-)S-H. The strains along each lattice direction of sodium incorporated C-(A-)S-H are investigated as functions of hydrostatic pressure, which yields the bulk modulus at ambient pressure and anisotropic incompressibility along each direction. The role of sodium incorporation and Al-induced crosslinking in reinforcing the nanomechanical properties of C-S-H is discussed.

Chapter 7 highlights the major concluding remarks in this thesis. Potential future studies are also discussed.

Chapter 8 lists an appendix of additional images and data of samples studied in this thesis and schemes for data analysis.

1.3 References

1. Myers, R.J., G. Geng, J. Li, E.D. Rodriguez, J.Y. Ha, P. Kidkhunthod, G. Sposito, L.N. Lammers, A.P. Kirchheim and P.J.M. Monteiro, Role of adsorption phenomena in cubic tricalcium aluminate dissolution. *Langmuir*, 2017. **33**(1): p. 45-55.
2. Li, J., W. Zhang, C. Li and P.J.M. Monteiro, Green concrete containing diatomaceous earth and limestone: workability, mechanical properties, and life-cycle assessment. *Journal of Cleaner Production*, 2019. **223**: p. 662-679.
3. Miller, S.A., A. Horvath and P.J.M. Monteiro, Readily implementable techniques can cut annual CO₂ emissions from the production of concrete by over 20%. *Environmental Research Letters*, 2016. **11**(7).
4. Gartner, E., Industrially interesting approaches to "low-CO₂" cements. *Cement and Concrete Research*, 2004. **34**(9): p. 1489-1498.
5. Gartner, E.M. and D.E. Macphee, A physico-chemical basis for novel cementitious binders. *Cement and Concrete Research*, 2011. **41**(7): p. 736-749.

6. Bae, S., R. Taylor, D. Hernandez-Cruz, S. Yoon, D. Kilcoyne and P.J.M. Monteiro, Soft x-ray spectromicroscopic investigation of synthetic c-s-h and c3s hydration products. *Journal of the American Ceramic Society*, 2015. **98**(9): p. 2914-2920.
7. Taylor, H.F.W., *Cement chemistry*. Thomas Telford, 1997.
8. Mehta, P.K. and P.J.M. Monteiro, *Concrete: microstructure, properties, and materials*. New York: McGraw-Hill, 2014.
9. Lee, B.Y. and K.E. Kurtis, Proposed acceleratory effect of TiO₂ nanoparticles on Belite hydration: preliminary results. *Journal of the American Ceramic Society*, 2012. **95**(1): p. 365-368.
10. Juenger, M.C.G., F. Winnefeld, J.L. Provis and J.H. Ideker, Advances in alternative cementitious binders. *Cement and Concrete Research*, 2011. **41**(12): p. 1232-1243.
11. Cuesta, A., E.R. Losilla, M.A. Aranda, J. Sanz and G. Ángeles, Reactive belite stabilization mechanisms by boron-bearing dopants. *Cement and Concrete Research*, 2012. **42**(4): p. 598-606.
12. Juenger, M.C. and R. Siddique, Recent advances in understanding the role of supplementary cementitious materials in concrete. *Cement and Concrete Research*, 2015. **78**: p. 71-80.
13. Snellings, R., G. Mertens and J. Elsen, Supplementary cementitious materials. *Applied Mineralogy of Cement & Concrete*, 2012. **74**: p. 211-278.
14. Lothenbach, B., K. Scrivener and R. Hooton, Supplementary cementitious materials. *Cement and Concrete Research*, 2011. **41**(12): p. 1244-1256.
15. Scrivener, K.L., B. Lothenbach, N. De Belie, E. Gruyaert, J. Skibsted, R. Snellings and A. Vollpracht, TC 238-SCM: hydration and microstructure of concrete with SCMs state of the art on methods to determine degree of reaction of SCMs. *Materials and Structures*, 2015. **48**(4): p. 835-862.
16. L'Hôpital, E., B. Lothenbach, G. Le Saout, D. Kulik and K. Scrivener, Incorporation of aluminium in calcium-silicate-hydrates. *Cement and Concrete Research*, 2015. **75**: p. 91-103.
17. Richardson, I.G., The calcium silicate hydrates. *Cement and Concrete Research*, 2008. **38**(2): p. 137-158.
18. Myers, R.J., E. L'Hopital, J.L. Provis and B. Lothenbach, Effect of temperature and aluminium on calcium (alumino)silicate hydrate chemistry under equilibrium conditions. *Cement and Concrete Research*, 2015. **68**: p. 83-93.
19. Richardson, I.G., Model structures for C-(A)-SH (I). *Acta Crystallographica Section B: Structural Science, Crystal Engineering and Materials*, 2014. **70**(6): p. 903-923.
20. Skibsted, J. and M.D. Andersen, The effect of alkali ions on the incorporation of aluminum in the calcium silicate hydrate (C-S-H) phase resulting from Portland cement hydration studied by ²⁹Si MAS NMR. *Journal of the American Ceramic Society*, 2013. **96**(2): p. 651-656.
21. L'Hôpital, E., B. Lothenbach, K. Scrivener and D. Kulik, Alkali uptake in calcium alumina silicate hydrate (CASH). *Cement and Concrete Research*, 2016. **85**: p. 122-136.
22. Pardal, X., F. Brunet, T. Charpentier, I. Pochard and A. Nonat, ²⁷Al and ²⁹Si solid-state NMR characterization of calcium-aluminosilicate-hydrate. *Inorganic chemistry*, 2012. **51**(3): p. 1827-1836.

23. Manzano, H., J.S. Dolado, M. Griebel and J. Hamaekers, A molecular dynamics study of the aluminosilicate chains structure in Al-rich calcium silicate hydrated (C-S-H) gels. *Physica Status Solidi a-Applications and Materials Science*, 2008. **205**(6): p. 1324-1329.
24. Myers, R.J., S.A. Bernal, R. San Nicolas and J.L. Provis, Generalized structural description of calcium–sodium aluminosilicate hydrate gels: the cross-linked substituted tobermorite model. *Langmuir*, 2013. **29**(17): p. 5294-5306.
25. Myers, R.J., E. L'Hopital, J.L. Provis and B. Lothenbach, Composition-solubility-structure relationships in calcium (alkali) aluminosilicate hydrate (C-(N,K-)A-S-H). *Dalton Transactions*, 2015. **44**(30): p. 13530-13544.
26. Myers, R.J., S.A. Bernal and J.L. Provis, Phase diagrams for alkali-activated slag binders. *Cement and Concrete Research*, 2017. **95**: p. 30-38.
27. Ozcelik, V.O. and C.E. White, Nanoscale charge-balancing mechanism in alkali-substituted calcium-silicate-hydrate gels. *Journal of Physical Chemistry Letters*, 2016. **7**(24): p. 5266-5272.
28. Brough, A. and A. Atkinson, Sodium silicate-based, alkali-activated slag mortars: part I. Strength, hydration and microstructure. *Cement and Concrete Research*, 2002. **32**(6): p. 865-879.
29. Richardson, I., A. Brough, G. Groves and C. Dobson, The characterization of hardened alkali-activated blast-furnace slag pastes and the nature of the calcium silicate hydrate (CSH) phase. *Cement and Concrete Research*, 1994. **24**(5): p. 813-829.
30. Puertas, F., M. Palacios, H. Manzano, J.S. Dolado, A. Rico and J. Rodriguez, A model for the C-A-S-H gel formed in alkali-activated slag cements. *Journal of the European Ceramic Society*, 2011. **31**(12): p. 2043-2056.
31. Fernandez-Jimenez, A., N. Cristelo, T. Miranda and A. Palomo, Sustainable alkali activated materials: precursor and activator derived from industrial wastes. *Journal of Cleaner Production*, 2017. **162**: p. 1200-1209.
32. Richardson, I.G., The nature of the hydration products in hardened cement pastes. *Cement & Concrete Composites*, 2000. **22**(2): p. 97-113.

2. A Brief literature review

2.1 Portland cement

The binder of most modern cementitious materials, including concrete, is Portland cement (PC)-based [1] [2]. The PC mainly consists of tricalcium silicate (Ca_3SiO_5 , also termed C_3S in cement chemistry notation, or alite as foreign-ion doped C_3S), dicalcium silicate (Ca_2SiO_4 , also termed C_2S ; or belite as foreign-ion doped C_2S), tricalcium aluminate (C_3A , $\text{Ca}_3\text{Al}_2\text{O}_6$), tetracalcium aluminoferrite (C_4AF , $\text{Ca}_2\text{AlFeO}_5$, also termed ferrite or brownmillerite), and calcium sulfates (CaSO_4) [3]. The reactions between C_3A and calcium sulfates (alternatively, calcium sulfate hemihydrate and calcium sulfate dihydrate) and between C_4AF and calcium sulfates (alternatively, calcium sulfate hemihydrate and calcium sulfate dihydrate) both yields needle-like ettringite crystallites, contributing to the setting and hardening of concrete, but barely contributing to the strength development of concrete. The hydration of C_3S and C_2S (the reaction between water and these calcium silicates) at ambient temperature both yields portlandite ($\text{Ca}(\text{OH})_2$) micro crystallites and calcium silicate hydrate (C-S-H), the latter is the principal binding phase in hardened PC concrete [4]. The C-S-H is highly porous at mesoscale. This C-S-H phase is poorly crystalline in the hydration system of plain PC and C_3S , and typically X-ray amorphous [5], often known as C-S-H gel. The building blocks of this C-S-H phase in a well-known CM-II colloidal model are nano globules with particle size of ~ 3.5 nm [6] [7]. The building blocks pack together in two different packing densities, named as low-density C-S-H and high density C-S-H. The low-density C-S-H often refers to the outer product C-S-H in the originally water-filled spaces, and high density C-S-H refers to the inter product C-S-H within the spaces originally occupied by C_3S or C_2S grains [5]. These globules have an internal layered structure with voids and defects [7].

The well-accepted molecular model of C-S-H (Figure 2.1) in the hydration system of plain PC is created by modifying a non-cross-linked tobermorite ($\text{Ca}_5\text{Si}_6\text{O}_{16}(\text{OH})_2 \cdot 4(\text{H}_2\text{O})$ or $\text{Ca}_5\text{H}_2\text{Si}_6\text{O}_{18} \cdot 6(\text{H}_2\text{O})$) structure [8] with defected dreierketten-type silicate tetrahedron chains, which consist of bridging (Q^2_{B}) and paired tetrahedra (Q^2_{P}), flanked on Ca-O sheets to form negative-charged calcium silicate basal layers [9]. The adjacent basal layers are charge-balanced by hydrated Ca species ($[\text{Ca}(\text{H}_2\text{O})_6]^{2+}$ and/or $[\text{Ca}(\text{OH})(\text{H}_2\text{O})_5]^+$) [10]. At high Ca/Si ratios, more bridging silicate tetrahedra are replaced by Ca atom, leading to a shorter chain of silicate tetrahedra. The large amount of interlayer Ca acts as a barrier to long-range ordering of the stacked layers of C-S-H. During the hydration of C_3S and C_2S , the Ca-to-Si molar ratio (Ca/Si) of C-S-H ranges from 1.2 to 2.1 [10], and the mean Ca/Si molar ratio of C-S-H is relatively constant over curing age of concrete with a mean value of ~ 1.7 [11]. However, the mean chain length (MCL) of silicate tetrahedra in C-S-H during the hydration of PC systematically increases from ~ 2 to ~ 5 over time [12].

When PC or C_3S is blended with high volume of amorphous siliceous materials (e.g, silica fume, mainly SiO_2), the amorphous siliceous phases reacts with lime-rich pore solution of the blends, reducing the concentration of Ca in the pore solution, the quantity of portlandite and Ca/Si ratio of C-S-H. A reduced Ca/Si ratio favors the formation of C-S-H with long-range ordering of stacked layers along the c-axis. These nanocrystalline C-S-H is known as C-S-H(I) [13]. The bulk Ca/Si molar ratio of these nanocrystalline C-S-H(I) typically varies from 0.8 to 1.5. Ca/Si

ratio below 0.8 favors the precipitation of amorphous silica as a secondary product while Ca/Si ratio above 1.5 favors the formation of portlandite as a secondary product. At high Ca/Si ratios, Ca atoms occupy the bridging sites in C-S-H(I), results in discontinuous dimers on the calcium silicate basal layer. Such positive-charge bridging Ca species attract the negative-charge calcium silicate basal layer, leading to a smaller interlayer spacing of C-S-H(I) at a high Ca/Si ratio. At low Ca/Si ratios, the structure of C-S-H(I) is more similar to tobermorite, with more bridging sites occupied by silicate tetrahedra instead of Ca, leading to a longer continuous chain of the silicate tetrahedron [14]. Such long silicate chains can be constituted by tens of silicate tetrahedra at Ca/Si ratio of ~ 0.8 [13]. The inversion correlation between mean silicate chain length and the bulk Ca/Si ratio of C-S-H(I) was also evidenced by X-ray absorption near-edge structure (XANES) spectroscopy [15]. The coordination symmetry of the Si-O in C-S-H(I) is independent of Ca/Si molar ratio, and the Si-O is always highly tetrahedrally symmetric. Besides, the coordination symmetry of Ca-O in C-S-H(I) seems independent of its Ca/Si ratio, always a distorted octahedral-like structure. The symmetry status of Ca in C-S-H(I) is similar to that of Ca in C-S-H in hydrated plain PC [15].

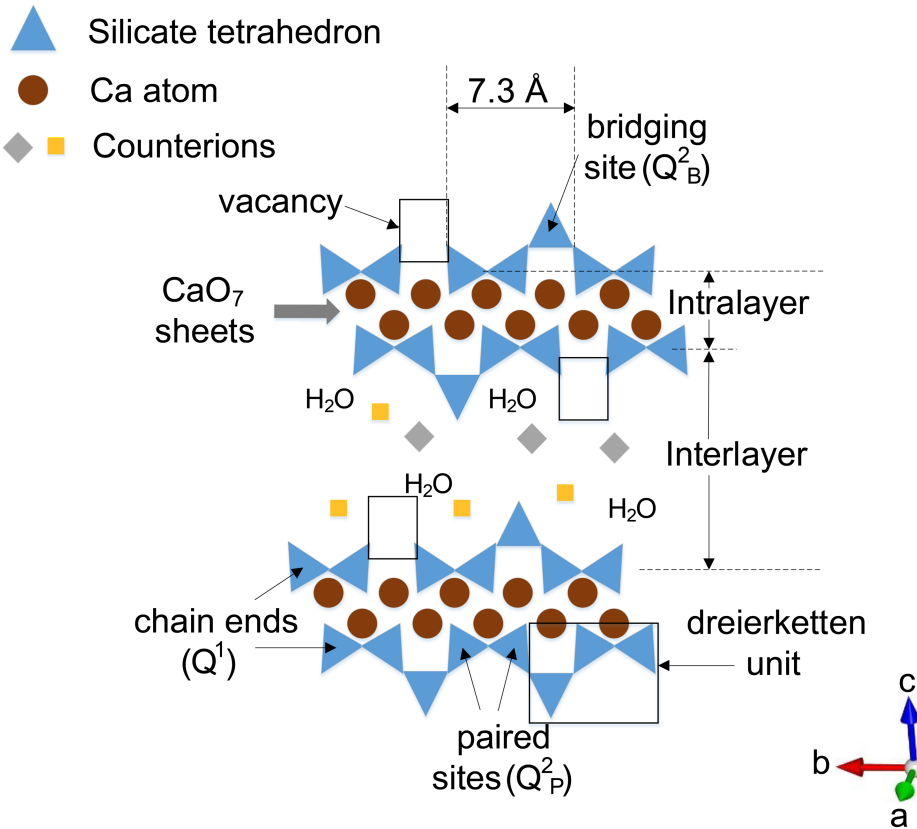


Figure 2.1. Schematic of the molecular structure of C-S-H based on non-cross-linked tobermorite. The brown circles are Ca species in the CaO₇ sheet, and blue triangles represent silicate tetrahedra at paired sites and bridging sites. The grey diamonds and yellow squares represent sites which can be occupied by cations that charge-balance the structure as a whole (e.g., Ca²⁺ and CaOH⁺) [14].

The hydration of C_2S yields more C-S-H and less portlandite relative to that of C_3S due to the lower Ca content in C_2S . The formation of C_2S requires less energy and generates less CO_2 relative to that of C_3S due to lower kilning temperature and lower Ca content of C_2S [16] [17]. Thus, many belite-rich cements (e.g., high belite cement and belite-ye'elimite-ferrite cement) have been developed and are expected to contribute lower environmental impacts from their manufacture [16]. However, C_2S generally exhibits lower hydraulic reactivity compared to C_3S [18]. Therefore, the hydration of these belite-rich cements typically exhibits lower compressive strength relative to ordinary Portland cement [19].

The most common C_2S in PC is β type C_2S , and the hydraulic reactivity and hydration of β - C_2S have been intensively studied. The higher reactivity of monoclinic C_3S relative to monoclinic β - C_2S can be explained by the abundant ionic oxygen atoms in C_3S and the absence of such ionic oxygen atoms in β - C_2S . These ionic oxygen atoms are loosely bond with Ca atom with bond lengths of 2.38-2.46 Å [20]. Thus, the ionic oxygen atoms can easily form oxide with electrophile cations (e.g., H^+ and Ca^{2+}). It is also important to investigate the hydraulic reactivity of other C_2S polymorphs, α , α'_H , α'_L , and γ types [21]. The polymorphic transformation of C_2S are shown in Figure 2.2. α - C_2S is thermodynamically unfavorable at ambient temperature, this polymorph normally transforms into β type during cooling process and is not observed in the final product of cement [22]. γ - C_2S scarcely reacts with water at ambient temperature [23]. β - C_2S is also metastable at ambient temperature with certain degree of hydraulic reactivity [24]. To stabilize the formation of β - C_2S at ambient temperature, dopants such as Na and K are often introduced to induce strains and dislocation of the lattice structure of β - C_2S [25]. α'_H - C_2S is more hydraulically reactive than β - C_2S and is reasonably easy to stabilize by the addition of dopants, e.g., B^{3+} , K^+ , P^{5+} , and Na^+ [26]. Particularly, boron has been proved as a successful stabilizer, and boron-doped β - C_2S exhibits the highest hydration rate [19] [27]. However, boron is relatively expensive so it is unrealistic to produce belite-rich cement with boron-doped α'_H - C_2S for general construction purpose. The investigation of inexpensive dopants, e.g., phosphorus, in C_2S is needed to develop a reactive belite-rich cement.

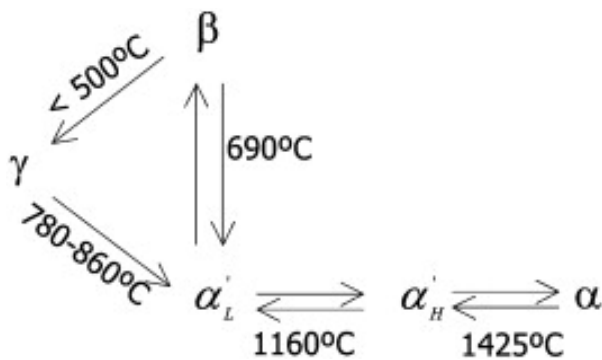


Figure 2.2 Polymorphic transformations of stoichiometric C_2S at different calcination temperatures. [18]

Recent advances in synchrotron-based X-ray techniques have significantly improved the ability to directly obtain morphological and chemical information of hydrated triclinic C_3S systems: coupling state-of-the-art soft X-ray ptychographic imaging and scanning transmission X-ray

microscopy (STXM) with X-ray absorption near-edge fine structure (XANES) spectroscopy now enables transmission imaging at spatial resolution of about 10 nm and chemical information at spatial resolution of about 60 nm, respectively [28] [29] [30]. This method is promising to the understanding of the micro-chemistry and morphology of the hydration of different C₂S polymorphs at a fine scale.

2.2 Calcium aluminosilicate hydrate- a binding phase in hardened blended Portland cement concrete

Portland cement is often partially substituted by supplementary cementitious materials (SCMs), e.g., fly ash, ground granulated blast furnace slag (GGBFS), and calcined clay [31] [32] [33]. The partial substitution of cement by SCMs exhibits many advantages, the primary purposes of the partial substitution include: (1) improve the long term mechanical properties and durability of hardened concrete by refined its microstructure; (2) decrease the temperature rise during adiabatic process of concrete; (3) decrease the CO₂ emission and primary energy consumption during the manufacture of concrete; (4) reduce the cost of concrete manufacture if these SCMs are locally available [34] [35] [36] [37].

Pozzolanic reaction [38] between the aluminosilicate-bearing SCMs and calcium hydroxide, which is generated during cement hydration, yields more calcium aluminosilicate hydrate (C-A-S-H), and possible generates other secondary products (e.g., katoite (Ca₃Al₂(OH)₁₂ and stratlingite (Ca₂Al₂O₅.8H₂O)) [2]. The mean Ca/Si molar ratio of calcium silicate hydrate decreases from ~1.7 in plain Portland cement to below 1.5 in blended Portland cement containing fly ash, GGBFS, or calcined clay (e.g., mainly metakaolin) [39]. As mentioned earlier, unlike the nanostructure of C-S-H in hydrated plain Portland cement, where lacks the layer stacking ordering along the c-axis and is X-ray amorphous [40], the C-A-S-H in hydrated blended Portland cement is often more ordered along the c-axis with the appearance of a basal peak at d-spacing of 9-14 Å [41]. The C-A-S-H phase is structurally similar to tobermorite and is also analogous to synthetic C-A-S-H [42], which can be readily obtained by mixing lime or calcium hydroxide and amorphous aluminosilicate with water [43]. The molecular structures of C-A-S-H are shown in Figure 2.3.

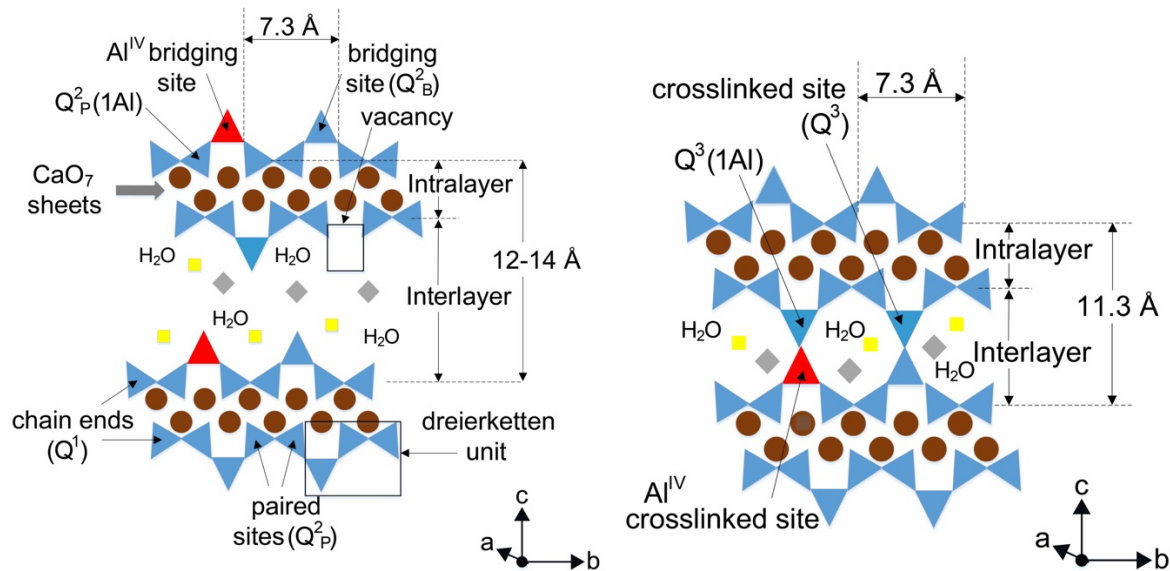


Figure 2.3 Schematic of the molecular structure of C-A-S-H based on (left) non-cross-linked tobermorite; (right) cross-linked tobermorite. The brown circles are Ca species in the CaO_7 sheet, and blue triangles represent silicate tetrahedra at paired sites and bridging sites. The red triangles represent aluminate tetrahedra at bridging sites and cross-linking sites. The grey diamonds and yellow squares represent sites which can be occupied by cations that charge-balance the structure as a whole (e.g., Ca^{2+} and CaOH^+).

At curing temperature below $80\text{ }^\circ\text{C}$, the widely proposed molecular structure of C-S-H is similar to that of 14 \AA tobermorite [8]. The molecular structure of non cross-linked C-A-S-H is similar to non cross-linked C-S-H, but the aluminate tetrahedron (four-fold coordinated aluminum, Al4) is incorporated in the “dreierketten” silicate chain of C-S-H at bridging sites, since the incorporation of aluminate at paired sites is thermodynamically unfavorable [44]. The partial substitution of silicate tetrahedra by aluminate tetrahedra yields a more negative charged basal layer, which requires more cations to charge-balance the entire structure compared to C-S-H [45]. Such substitution induces a longer aluminosilicate chain of C-A-S-H relative to C-S-H [46]. At curing temperature of $80\text{ }^\circ\text{C}$ or higher, the molecular structure of C-A-S-H is similar to 11 \AA Al-tobermorite [47] [48], where two bridging sites are cross-linked, forming double chains of aluminosilicate tetrahedra in cross-linked C-A-S-H [49]. Due to the formation of cross-linking sites (Q^3 and $\text{Q}^3(1\text{Al})$, see Figure 2.3), the basal spacing of cross-linked C-A-S-H is often fixed at about 11.3 \AA [50].

In addition to four-fold coordinated Al, five-fold (Al5) and six-fold (Al6) coordinated Al are also present in the C-A-S-H products [51]. Also, the higher aluminum and calcium concentrations favor the precipitation of katoite (C_3AH_6), and strätlingite (C_2ASH_8) as secondary products [52]. Previous ^{27}Al nuclear magnetic resonance (NMR) spectroscopy studies have shown two distinct environments of six-fold coordinated Al, which are positioned at different chemical shifts in ^{27}Al NMR spectra [46] [43] [53]. The Al6 positioned at a more positive chemical shift (Al6-a) is assigned to six-fold coordinated Al which occurs in the interlayer of C-A-S-H, while at higher Ca/Si molar ratio (i.e., $\text{Ca/Si} > 1.2$) or higher Al/Si molar ratio (i.e., $\text{Al/Si} > 0.1$), Al6 is also positioned at a less positive chemical shift (Al6-b), which is assigned to an amorphous aluminate

hydrate [54]. This phase is named as third aluminate hydrate (TAH, the first and second aluminate hydrates in hydrated cements are ettringite and monosulfoaluminate hydrate, respectively) [55]. No consensus exists with respect to the location of TAH in C-A-S-H products and its Al chemical environment. Andersen et al. [54] proposed that the TAH forms as separate phase(s) or on the external surface of C-A-S-H, and its Al coordination is similar to AFm phases (hydrocalumite-like structure) or ettringite. L'Hôpital et al. [51] [56] [57] reported the precipitation of abundant aluminum hydroxide gel-like complex or phase in C-A-S-H products. Renaudin et al. [58] [59] proposed that the presence of TAH in the interlayer of C-A-S-H leads to an increase of basal spacing. This increase in basal spacing in C-A-S-H was also confirmed by L'Hôpital et al. particularly at high Ca/Si molar ratios (i.e., $Ca/Si > 1.0$) (see Figure 2.4). Further study is clearly needed to clarify the speciation and location of TAH in C-A-S-H products. In addition, limited existing results described the effect of synthesis temperature on the local environment of Al, which also needs further investigation.

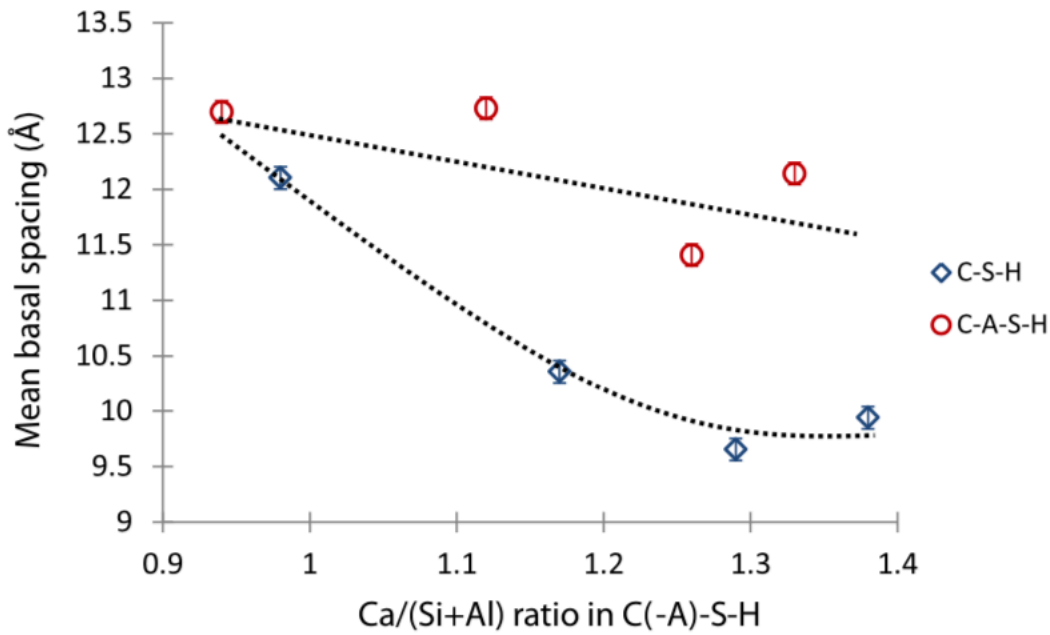


Figure 2.4 Variation of the basal spacing (d_{002}) as a function of the initial bulk $Ca/(Si + Al)$ ratio in synthetic C-S-H and C-A-S-H (initial bulk $Al/Si = 0.05$) synthesized at 20C. The basal spacing was determined by lab-XRD with the use of anatase as an internal standard. Dot lines are intended as eye guides only [56].

One major debate in existing C-S-H models [60] [61] [62] [63] is the coordination environment of Ca when C-S-H is synthesized with various Ca/Si ratios and under different synthesis conditions. Extended X-ray Absorption Fine Structure (EXAFS) spectroscopy study showed that Ca is octahedrally coordinated in C-S-H at Ca/Si of 0.7-1.4, 11Å tobermorite, and 14Å tobermorite [60]. Kirkpatrick et al. [61] reported distinct values of the coordination number of Ca-O: 5.5-6.2 for synthetic C-S-H, 6.1 for 11Å tobermorite, and 6.9 for 14Å tobermorite. Pair distribution function (PDF) study showed that the coordination number of Ca-O in synthetic C-S-H systematically decreases from 7.1 to 6.0 as Ca/Si ratio increases [62]. The coordination number of Ca-O in 35 crystalline calcium silicate hydrate minerals and related minerals is mainly either six or seven, with a small number of eight-fold coordinated Ca atoms [64].

Transmission electron microscopy (TEM) studies have shown that the outer product C-S-H (formed in spaces where were originally filled with water) is fibrillar in hardened plain PC paste, while the outer product C-S-H is foil-like when GGBFS is blended with Portland cement [65] [10]. The morphology of C-S-H with various Ca/Si molar ratios and synthesis conditions varies from foil to fiber-like [66] at the microscale. However, the effects of chemical compositions and synthesis temperatures on the morphology of synthetic C-A-S-H have not been extensively studied. C-(A-)S-H is very vulnerable to high vacuum condition and electron beam. The sample preparation and high accelerating voltage of TEM may alter the nature of C-(A-)S-H samples [22]. Degradation of C-(A-)S-H is often observed in TEM studies, particularly when the magnification level is high.

The existing studies mainly concentrated on the structure of C-S-H at atomic-to-micro scale, the unclear influences of Al incorporation and synthesis temperature on the structure of C-S-H at atomic to micro scale remain to be investigated. Ptychographic imaging using synchrotron-radiation soft X-ray has been recently reported in the morphological study of cement-based systems [67] [68]. It generates the least amount of radiation damage since the incident beam energy is much lower (~800 eV). Such soft X-ray allows the penetration of hydrate samples with thickness of a few micron, which is significantly higher than the capacity of TEM (tens to hundreds of nanometers). Coupled with scanning transmission X-ray microscopy (STXM), it enables a nanometer-resolved spectroscopic investigation. This method is promising to understand the atomic-to-micro structure of C-A-S-H systematically. Preliminary studies have presented a strong correlation between degree of polymerization of silicate chain of both synthetic and hydration product C-S-Hs and X-ray absorption near edge fine structure (XANES) around Si K-edge [13] [29], yet more experimental studies are needed to provide XANES spectra of C-(A-)S-H covering the full range of chemical compositions and synthesis temperatures. Moreover, the experimental setup also provides the capacity to understand the influences of aluminum incorporation and synthesis temperature on the coordination environment of Ca in C-(A-)S-H.

2.3 Alkali incorporated calcium (alumino) silicate hydrate- a binding phase in hardened concrete

As outlined in the previous chapters, the main binding phase in hydrated plain PC-based cementitious materials is calcium silicate hydrate (C-S-H), a complex gel or nanocrystalline phase, which governs the physical, mechanical and durability properties of concrete [69] [70]. Plain PC typically contains up to ~1wt.% alkali (Na_2O and K_2O), thus a large number of charge-balanced sites of C-S-H is capable of incorporating Na^+ and/or K^+ [71]. Most of common SCMs, e.g., fly ash, contains at least 1wt.% alkali. Bio-mass and agriculture byproducts (e.g., rice husk ash), which are also incorporated in concrete, contain even higher amounts of alkali [72] [73]. Thus, Na and/or K are incorporated in C-S-H when PC is blended with these SCMs. In addition, alkali activators (e.g., sodium hydroxide, potassium hydroxide, and sodium metasilicate) used for alkali-activated materials (e.g., alkali-activated GGBFS and alkali activated fly ash) are also Na- or K- rich [74]. Thus, the principal binding phase in PC-based cementitious materials and alkali-activated materials is essentially alkali-incorporated calcium (alumino) silicate hydrate, which is

also termed C-N,K-(A-)S-H [75]. The Na and K ions are very likely adsorbed on the surface of C-(A-)S-H nano grains, and also charge-balanced in the interlayer of C-(A-)S-H. The presence of such alkali species facilitates the formation of cross-linking in the presence of Al, lowering the equilibrium temperature for cross-linking from $>80\text{ }^{\circ}\text{C}$ in alkali-free C-A-S-H to $\sim 50\text{ }^{\circ}\text{C}$ in the presence of alkalis [76]. Thus, alkali incorporated C-A-S-H is the key phase in hardened PC-based concrete as well as alkali activated GGBFS. Such alkaline C-A-S-H (C-N,K-A-S-H) is also the major binding phase in ~ 2000 -year-old ancient Roman concrete, an important geological material [77] [78]. Moreover, the alkali content in the binder provides a highly alkaline environment ($\text{pH} > 13$) to stabilize the passive film of steel rebars in reinforced concrete and to provide higher sensitivity to carbonation from atmospheric CO_2 [2]. Thus, the incorporation of alkali in C-S-H and C-A-S-H is critical to the physical and mechanical properties and long-term performance of concrete structures.

The relationship between structure and micromechanical properties of C-S-H and C-A-S-H has been extensively studied using nanoindentation; however, the reliability of experimental results using nanoindentation is often influenced by the defects and pores near sample surface [79] [70]. The uncertainty of the phases underneath the nano-indentations also makes the results of mechanical properties using nano-indentation questionable [80]. Using high-pressure X-ray diffraction (HP-XRD), the influence of defects and pores at nano-to-macro scale on the nanomechanical properties of mesoporous phases can be avoided since the all pore can be filled with a pressure-transmitting medium (e.g., methanol-ethanol solution and silicone oil) [81]. Thus, HP-XRD is ideal for determining the mechanical properties of crystalline or nanocrystalline phases, such as nanocrystalline C-S-H(I) and C-A-S-H, at the lowest hierarchical level. Geng et al. demonstrated that the densification of the interlayer of C-S-H, instead of the defects at silicate chains (i.e., the mean length of the silicate chains), governs the mechanical properties of C-S-H synthesized at $20\text{ }^{\circ}\text{C}$ at the bulk Ca/Si ratio of 0.8-1.4 under hydrostatic pressure [82]. Namely, the densification of interlayer of C-S-H governs its bulk modulus, and bulk modulus decreases with an increased basal spacing of C-S-H. Interestingly, the incompressibility along the c-axis of C-S-H increases with a decreased interlayer spacing, while the incompressibility along the a- and b-axes is independent of Ca/Si molar ratio. Another study by Geng et al. demonstrated that Al-induced cross-linking sites in C-A-S-H synthesized at $80\text{ }^{\circ}\text{C}$ increase its incompressibility along the c-axis and bulk modulus, but the influences of Al-induced cross-linking sites on the incompressibility along the a and b-axes were negligible [83]. The cross-linking sites act as supporting columns for resisting the deformation along the c-axis. Recent molecular dynamics studies of the nanomechanical properties of C-S-H and C-A-S-H agreed with the experimental work using HP-XRD [49]. The nanomechanical properties of tobermorite have also been determined using HP-XRD. The bulk moduli of tobermorite systematically decreased with an increased basal spacing (from 9, 11, to 14 \AA) [84], which can be also explained by the densification of their interlayer. The same trend between nanomechanical properties and basal spacing was reported in a first-principle study [85].

The HP-XRD technique has been successfully applied to study the nanomechanical properties of many phases in cementitious materials (e.g., strätlingite, katoite, C_3A , ye'elimite, and zeolite) [86-90]. However, the mechanical properties of Na or K incorporated C-S-H and C-A-S-H at molecular-to-nano scale, have rarely been investigated in experimental studies. Oh et al. found that the bulk modulus of Na-incorporated C-A-S-H (C-N-A-S-H) from NaOH activated GGBFS

is comparable to that of water-cured C-S-H [86], despite that the Al/Si ratio and Na content of C-N-A-S-H was not reported. Puertas et al. suggested that Al incorporation enhanced the mechanical properties of Na-based activated GGBFS using nanoindentation and molecular dynamics simulation with different tobermorite models [91]. However, the influence of nanopores in alkali-activated slag on the mechanical properties of C-N-S-H and C-N-A-S-H was omitted. The investigation of alkali incorporated C-S-H and C-A-S-H using HP-XRD can provide more reliable experimental evidence on their nanomechanical properties, which will be critical in designing high performance (e.g., high-strength) blended PC-based concrete and alkali-activated materials using a bottom-up approach.

2.4 References

1. Taylor, H.F.W., Cement chemistry. Thomas Telford, 1997.
2. Mehta, P.K. and P.J.M. Monteiro, Concrete: microstructure, properties, and materials. New York: McGraw-Hill, 2006.
3. Scrivener, K.L. and A. Nonat, Hydration of cementitious materials, present and future. Cement and Concrete Research, 2011. **41**(7): p. 651-665.
4. Bullard, J.W., H.M. Jennings, R.A. Livingston, A. Nonat, G.W. Scherer, J.S. Schweitzer, K.L. Scrivener and J.J. Thomas, Mechanisms of cement hydration. Cement and Concrete Research, 2011. **41**(12): p. 1208-1223.
5. Richardson, I.G., The nature of the hydration products in hardened cement pastes. Cement & Concrete Composites, 2000. **22**(2): p. 97-113.
6. Skinner, L. B., Chae, S. R., Benmore, C. J., Wenk, H. R., and Monteiro, P. J. M. Nanostructure of calcium silicate hydrates in cements. Physical review letters, 2010, **104**(19), 195502.
7. Jennings, H. M. Refinements to colloid model of CSH in cement: CM-II. Cement and Concrete Research, 2008, **38**(3), 275-289.
8. Bonaccorsi, E., S. Merlino and A.R. Kampf, The crystal structure of tobermorite 14 A (Plombierite), a C-S-H phase. Journal of the American Ceramic Society, 2005. **88**(3): p. 505-512.
9. Richardson, I.G., Tobermorite/jennite- and tobermorite/calcium hydroxide-based models for the structure of C-S-H: applicability to hardened pastes of tricalcium silicate, beta-dicalcium silicate, Portland cement, and blends of Portland cement with blast-furnace slag, metakaolin, or silica fume. Cement and Concrete Research, 2004. **34**(9): p. 1733-1777.
10. Richardson, I.G., The calcium silicate hydrates. Cement and Concrete Research, 2008. **38**(2): p. 137-158.
11. Richardson, I.G. and G.W. Groves, Microstructure and Microanalysis of Hardened Ordinary Portland-Cement Pastes. Journal of Materials Science, 1993. **28**(1): p. 265-277.
12. Taylor, R., I.G. Richardson and R.M.D. Brydson, Composition and microstructure of 20-year-old ordinary Portland cement-ground granulated blast-furnace slag blends containing 0 to 100% slag. Cement and Concrete Research, 2010. **40**(7): p. 971-983.
13. Tajuelo Rodriguez, E., Richardson, I. G., Black, L., Boehm-Courjault, E., Nonat, A., and Skibsted, J. . Composition, silicate anion structure and morphology of calcium silicate hydrates (CSH) synthesised by silica-lime reaction and by controlled hydration of tricalcium silicate (C3S). Advances in Applied Ceramics, 2015, 114(7), 362-371.

14. Li, J., G. Geng, W. Zhang, Y.-S. Yu, D.A. Shapiro and P.J. Monteiro, The hydration of β - and α' -dicalcium silicates: an x-ray spectromicroscopic study. *ACS Sustainable Chemistry & Engineering*, 2019. **7**(2): p. 2316-2326.
15. Bae, S., R. Taylor, D. Hernandez-Cruz, S. Yoon, D. Kilcoyne and P.J.M. Monteiro, Soft x-ray spectromicroscopic investigation of synthetic C-S-H and C3S hydration products. *Journal of the American Ceramic Society*, 2015. **98**(9): p. 2914-2920.
16. Juenger, M.C.G., F. Winnefeld, J.L. Provis and J.H. Ideker, Advances in alternative cementitious binders. *Cement and Concrete Research*, 2011. **41**(12): p. 1232-1243.
17. Gartner, E., Industrially interesting approaches to "low-CO₂" cements. *Cement and Concrete Research*, 2004. **34**(9): p. 1489-1498.
18. Cuesta, A., E.R. Losilla, M.A. Aranda, J. Sanz and G. Angeles, Reactive belite stabilization mechanisms by boron-bearing dopants. *Cement and Concrete Research*, 2012. **42**(4): p. 598-606.
19. Kim, Y.M. and S.H. Hong, Influence of minor ions on the stability and hydration rates of beta-dicalcium silicate. *Journal of the American Ceramic Society*, 2004. **87**(5): p. 900-905.
20. Durgun, E., H. Manzano, R. J. M. Pellenq, and Jeffrey C. Grossman. Understanding and controlling the reactivity of the calcium silicate phases from first principles. *Chemistry of Materials*, 2012, **24**(7): 1262-1267.
21. Hewlett, P., *Lea's chemistry of cement and concrete*. Butterworth-Heinemann, 2003.
22. Chen, J.H., Y.Y. Wang, C.C. Wan and D.C. Liou, Mas Nmr-Studies of the Hydration Process of Beta-C₂S in the Presence of Chromium. *Cement and Concrete Research*, 1994. **24**(2): p. 319-324.
23. Jelenic, I. and A. Bezjak, On the hydration kinetics of alpha'-modifications and beta-modifications of dicalcium silicate. *Cement and Concrete Research*, 1981. **11**(3): p. 467-471.
24. Black, L., A. Stumm, K. Garbev, P. Stemmermann, K.R. Hallam and G.C. Allen, X-ray photoelectron spectroscopy of the cement clinker phases tricalcium silicate and beta-dicalcium silicate. *Cement and Concrete Research*, 2003. **33**(10): p. 1561-1565.
25. Ishida, H., Y. Okada and T. Mitsuda, Highly reactive β -dicalcium silicate: II, hydration behavior at 25° C followed by ²⁹Si nuclear magnetic resonance. *Journal of the American Ceramic Society*, 1992. **75**(2): p. 359-363.
26. Ghose, A., S. Chopra and J.F. Young, Microstructural characterization of doped dicalcium silicate polymorphs. *Journal of Materials Science*, 1983. **18**(10): p. 2905-2914.
27. Müller, R., J. Neubauer and F. Götz-Neunhoeffler, Effects of phosphate rich raw materials on the crystallographic and hydraulic properties of dicalcium silicate. *Proceedings of the 11th Int. Cong. On the Chem. of Cement, Durban, South Africa*, 2003: p. 1045-1053.
28. Bae, S., R. Taylor, D. Shapiro, P. Denes, J. Joseph, R. Celestre, S. Marchesini, H. Padmore, T. Tyliczszak and T. Warwick, Soft x-ray ptychographic imaging and morphological quantification of calcium silicate hydrates (C-S-H). *Journal of the American Ceramic Society*, 2015. **98**(12): p. 4090-4095.
29. Li, Q.G., Y.; Geng, G.; Bae, S.; Monteiro, P. J. M.; CaCl₂-accelerated hydration of tricalcium silicate: a STXM study combined with ²⁹Si MAS NMR. *Journal of Nanomaterials*, 2015. **2015**: p. 1-10.

30. Geng, G., Myers, R. J., Yu, Y. S., Shapiro, D. A., Winarski, R., Levitz, P. E., Kilcoyne, D.A. and Monteiro, P. J. M. Synchrotron X-ray nanotomographic and spectromicroscopic study of the tricalcium aluminate hydration in the presence of gypsum. *Cement and Concrete Research*, 2018, 111, 130-137.
31. Snellings, R., G. Mertens and J. Elsen, Supplementary cementitious materials. *Applied Mineralogy of Cement & Concrete*, 2012. **74**: p. 211-278.
32. Lothenbach, B., K. Scrivener and R. Hooton, Supplementary cementitious materials. *Cement and Concrete Research*, 2011. **41**(12): p. 1244-1256.
33. Scrivener, K.L., B. Lothenbach, N. De Belie, E. Gruyaert, J. Skibsted, R. Snellings and A. Vollpracht, TC 238-SCM: hydration and microstructure of concrete with SCMs state of the art on methods to determine degree of reaction of SCMs. *Materials and Structures*, 2015. **48**(4): p. 835-862.
34. Miller, S.A., A. Horvath, P.J.M. Monteiro and C.P. Ostertag, Greenhouse gas emissions from concrete can be reduced by using mix proportions, geometric aspects, and age as design factors. *Environmental Research Letters*, 2015. **10**(11).
35. Fan, C. and S.A. Miller, Reducing greenhouse gas emissions for prescribed concrete compressive strength. *Construction and Building Materials*, 2018. **167**: p. 918-928.
36. Juenger, M.C. and R. Siddique, Recent advances in understanding the role of supplementary cementitious materials in concrete. *Cement and Concrete Research*, 2015. **78**: p. 71-80.
37. Snellings, R., A. Salze and K.L. Scrivener, Use of x-ray diffraction to quantify amorphous supplementary cementitious materials in anhydrous and hydrated blended cements. *Cement and Concrete Research*, 2014. **64**: p. 89-98.
38. Snellings, R. and K.L. Scrivener, Rapid screening tests for supplementary cementitious materials: past and future. *Materials and Structures*, 2016. **49**(8): p. 3265-3279.
39. Richardson, I.G. and G.W. Groves, Microstructure and microanalysis of hardened cement pastes involving ground granulated blast-furnace slag. *Journal of Materials Science*, 1992. **27**(22): p. 6204-6212.
40. Allen, A.J., J.J. Thomas and H.M. Jennings, Composition and density of nanoscale calcium-silicate-hydrate in cement. *Nature materials*, 2007. **6**(4): p. 311-316.
41. Faucon, P., A. Delagrave, J. Petit, C. Richet, J. Marchand and H. Zanni, Aluminum incorporation in calcium silicate hydrates (CSH) depending on their Ca/Si ratio. *The Journal of Physical Chemistry B*, 1999. **103**(37): p. 7796-7802.
42. Bae, S., C. Meral, J.-e. Oh, J. Moon, M. Kunz and P.J. Monteiro, Characterization of morphology and hydration products of high-volume fly ash paste by monochromatic scanning x-ray micro-diffraction (μ -SXRD). *Cement and Concrete Research*, 2014. **59**: p. 155-164.
43. Pardal, X., F. Brunet, T. Charpentier, I. Pochard and A. Nonat, ^{27}Al and ^{29}Si solid-state NMR characterization of calcium-aluminosilicate-hydrate. *Inorganic chemistry*, 2012. **51**(3): p. 1827-1836.
44. Manzano, H., J.S. Dolado, M. Griebel and J. Hamaekers, A molecular dynamics study of the aluminosilicate chains structure in Al-rich calcium silicate hydrated (C-S-H) gels. *Physica Status Solidi a-Applications and Materials Science*, 2008. **205**(6): p. 1324-1329.
45. Qomi, M.J.A., F.J. Ulm and R.J.M. Pellenq, Evidence on the dual nature of aluminum in the calcium-silicate-hydrates based on atomistic simulations. *Journal of the American Ceramic Society*, 2012. **95**(3): p. 1128-1137.

46. Andersen, M.D., H.J. Jakobsen and J. Skibsted, Characterization of white Portland cement hydration and the C-S-H structure in the presence of sodium aluminate by Al-27 and Si-29 MAS NMR spectroscopy. *Cement and Concrete Research*, 2004. **34**(5): p. 857-868.
47. Jackson, M.D., J. Moon, E. Gotti, R. Taylor, S.R. Chae, M. Kunz, A.H. Emwas, C. Meral, P. Guttman, P. Levitz, H.R. Wenk and P.J.M. Monteiro, Material and elastic properties of Al-tobermorite in ancient Roman seawater concrete. *Journal of the American Ceramic Society*, 2013. **96**(8): p. 2598-2606.
48. Merlino, S., E. Bonaccorsi and T. Armbruster, The real structure of tobermorite 11 angstrom: normal and anomalous forms, OD character and polytypic modifications. *European Journal of Mineralogy*, 2001. **13**(3): p. 577-590.
49. Yang, J., D. Hou and Q. Ding, Structure, dynamics and mechanical properties of cross-linked calcium aluminosilicate hydrate: a molecular dynamics study. *ACS Sustainable Chemistry & Engineering*, 2018.
50. Myers, R.J., E. L'Hopital, J.L. Provis and B. Lothenbach, Composition-solubility-structure relationships in calcium (alkali) aluminosilicate hydrate (C-(N,K)-A-S-H). *Dalton Transactions*, 2015. **44**(30): p. 13530-13544.
51. L'Hôpital, E., B. Lothenbach, G. Le Saout, D. Kulik and K. Scrivener, Incorporation of aluminium in calcium-silicate-hydrates. *Cement and Concrete Research*, 2015. **75**: p. 91-103.
52. Pardal, X., I. Pochard and A. Nonat, Experimental study of Si–Al substitution in calcium-silicate-hydrate (CSH) prepared under equilibrium conditions. *Cement and Concrete Research*, 2009. **39**(8): p. 637-643.
53. Sun, G., J.F. Young and R.J. Kirkpatrick, The role of Al in C–S–H: NMR, XRD, and compositional results for precipitated samples. *Cement and Concrete Research*, 2006. **36**(1): p. 18-29.
54. Andersen, M.D., H.J. Jakobsen and J. Skibsted, A new aluminium-hydrate species in hydrated Portland cements characterized by 27 Al and 29 Si MAS NMR spectroscopy. *Cement and Concrete Research*, 2006. **36**(1): p. 3-17.
55. Quillin, K., Performance of belite-sulfoaluminate cements. *Cement and Concrete Research*, 2001. **31**(9): p. 1341-1349.
56. L'Hôpital, E., B. Lothenbach, D. Kulik and K. Scrivener, Influence of calcium to silica ratio on aluminium uptake in calcium silicate hydrate. *Cement and Concrete Research*, 2016. **85**: p. 111-121.
57. L'Hôpital, E., B. Lothenbach, K. Scrivener and D. Kulik, Alkali uptake in calcium alumina silicate hydrate (CASH). *Cement and Concrete Research*, 2016. **85**: p. 122-136.
58. Renaudin, G., J. Russias, F. Leroux, F. Frizon and C. Cau-dit-Coumes, Structural characterization of C–S–H and C–A–S–H samples—part I: long-range order investigated by Rietveld analyses. *Journal of Solid State Chemistry*, 2009. **182**(12): p. 3312-3319.
59. Renaudin, G., J. Russias, F. Leroux, C. Cau-dit-Coumes and F. Frizon, Structural characterization of C–S–H and C–A–S–H samples—part II: local environment investigated by spectroscopic analyses. *Journal of Solid State Chemistry*, 2009. **182**(12): p. 3320-3329.
60. Lequeux, N., A. Morau, S. Philippot and P. Boch, Extended X-ray absorption fine structure investigation of calcium silicate hydrates. *Journal of the American Ceramic Society*, 1999. **82**(5): p. 1299-1306.

61. Kirkpatrick, R.J., G.E. Brown, N. Xu and X.D. Cong, Ca X-ray absorption spectroscopy of C-S-H and some model compounds. *Advances in Cement Research*, 1997. **9**(33): p. 31-36.
62. Soyer-Uzun, S., S.R. Chae, C.J. Benmore, H.R. Wenk and P.J.M. Monteiro, Compositional evolution of calcium silicate hydrate (C-S-H) Structures by total x-ray scattering. *Journal of the American Ceramic Society*, 2012. **95**(2): p. 793-798.
63. Moudrakovski, I.L., R. Alizadeh and J.J. Beaudoin, Natural abundance high field ^{43}Ca solid state NMR in cement science. *Physical Chemistry Chemical Physics*, 2010. **12**(26): p. 6961-6969.
64. Richardson, I.G., Model structures for C-(A)-SH (I). *Acta Crystallographica Section B: Structural Science, Crystal Engineering and Materials*, 2014. **70**(6): p. 903-923.
65. Richardson, I., A. Brough, G. Groves and C. Dobson, The characterization of hardened alkali-activated blast-furnace slag pastes and the nature of the calcium silicate hydrate (CSH) phase. *Cement and Concrete Research*, 1994. **24**(5): p. 813-829.
66. Rodriguez, E.T., I.G. Richardson, L. Black, E. Boehm-Courjault, A. Nonat and J. Skibsted, Composition, silicate anion structure and morphology of calcium silicate hydrates (C-S-H) synthesised by silica-lime reaction and by controlled hydration of tricalcium silicate (C3S). *Advances in Applied Ceramics*, 2015. **114**(7): p. 362-371.
67. Geng, G., J. Li, Y.-S. Yu, D.A. Shapiro, D.A. Kilcoyne and P.J. Monteiro, Nanometer-resolved spectroscopic study reveals the conversion mechanism of $\text{CaO} \cdot \text{Al}_2\text{O}_3 \cdot 10\text{H}_2\text{O}$ to $2\text{CaO} \cdot \text{Al}_2\text{O}_3 \cdot 8\text{H}_2\text{O}$ and $3\text{CaO} \cdot \text{Al}_2\text{O}_3 \cdot 6\text{H}_2\text{O}$ at an elevated temperature. *Crystal Growth & Design*, 2017. **17**(8): p. 4246-4253.
68. Geng, G., R.J. Myers, Y.S. Yu, D.A. Shapiro, R. Winarski, P.E. Levitz, D.A.L. Kilcoyne and P.J.M. Monteiro, Synchrotron X-ray nanotomographic and spectromicroscopic study of the tricalcium aluminate hydration in the presence of gypsum. *Cement and Concrete Research*, 2018. **111**: p. 130-137.
69. Yu, P., R.J. Kirkpatrick, B. Poe, P.F. McMillan and X.D. Cong, Structure of calcium silicate hydrate (C-S-H): near-, mid-, and far-infrared spectroscopy. *Journal of the American Ceramic Society*, 1999. **82**(3): p. 742-748.
70. Trtik, P., B. Munch and P. Lura, A critical examination of statistical nanoindentation on model materials and hardened cement pastes based on virtual experiments. *Cement & Concrete Composites*, 2009. **31**(10): p. 705-714.
71. Skibsted, J. and M.D. Andersen, The effect of alkali ions on the incorporation of aluminum in the calcium silicate hydrate (C-S-H) phase resulting from Portland cement hydration studied by ^{29}Si MAS NMR. *Journal of the American Ceramic Society*, 2013. **96**(2): p. 651-656.
72. Suraneni, P., M. Palacios and R.J. Flatt, New insights into the hydration of slag in alkaline media using a micro-reactor approach. *Cement and Concrete Research*, 2016. **79**: p. 209-216.
73. Bernal, S.A., J.L. Provis, B. Walkley, R. San Nicolas, J.D. Gehman, D.G. Brice, A.R. Kilcullen, P. Duxson and J.S. van Deventer, Gel nanostructure in alkali-activated binders based on slag and fly ash, and effects of accelerated carbonation. *Cement and Concrete Research*, 2013. **53**: p. 127-144.
74. Lothenbach, B., G. Le Saout, M. Ben Haha, R. Figi and E. Wieland, Hydration of a low-alkali CEM III/B-SiO₂ cement (LAC). *Cement and Concrete Research*, 2012. **42**(2): p. 410-423.

75. Myers, R.J., S.A. Bernal, J.D. Gehman, J.S. Deventer and J.L. Provis, The role of Al in cross-linking of alkali-activated slag cements. *Journal of the American Ceramic Society*, 2015. **98**(3): p. 996-1004.
76. Myers, R.J., S.A. Bernal, R. San Nicolas and J.L. Provis, Generalized structural description of calcium–sodium aluminosilicate hydrate gels: the cross-linked substituted tobermorite model. *Langmuir*, 2013. **29**(17): p. 5294-5306.
77. Jackson, M.D., S.R. Chae, S.R. Mulcahy, C. Meral, R. Taylor, P. Li, A.-H. Emwas, J. Moon, S. Yoon and G. Vola, Unlocking the secrets of Al-tobermorite in Roman seawater concrete. *American Mineralogist*, 2013. **98**(10): p. 1669-1687.
78. Jackson, M.D., E.N. Landis, P.F. Brune, M. Vitti, H. Chen, Q. Li, M. Kunz, H.-R. Wenk, P.J. Monteiro and A.R. Ingraffea, Mechanical resilience and cementitious processes in Imperial Roman architectural mortar. *Proceedings of the National Academy of Sciences*, 2014. **111**(52): p. 18484-18489.
79. Pelisser, F., P.J.P. Gleize and A. Mikowski, Effect of the Ca/Si molar ratio on the micro/nanomechanical properties of synthetic C-S-H measured by nanoindentation. *Journal of Physical Chemistry C*, 2012. **116**(32): p. 17219-17227.
80. Foley, E.M., J.J. Kim and M.M.R. Taha, Synthesis and nano-mechanical characterization of calcium-silicate-hydrate (C-S-H) made with 1.5 CaO/SiO₂ mixture. *Cement and Concrete Research*, 2012. **42**(9): p. 1225-1232.
81. Geng, G.Q., J.Q. Li, Y. Zhou, L. Liu, J.Y. Yan, M. Kunz and P.J.M. Monteiro, A high-pressure X-ray diffraction study of the crystalline phases in calcium aluminate cement paste. *Cement and Concrete Research*, 2018. **108**: p. 38-45.
82. Geng, G.Q., R.J. Myers, M.J.A. Qomi and P.J.M. Monteiro, Densification of the interlayer spacing governs the nanomechanical properties of calcium-silicate-hydrate. *Scientific Reports*, 2017. **7**.
83. Geng, G., R.J. Myers, J. Li, R. Maboudian, C. Carraro, D.A. Shapiro and P.J. Monteiro, Aluminum-induced dreierketten chain cross-links increase the mechanical properties of nanocrystalline calcium aluminosilicate hydrate. *Scientific Reports*, 2017. **7**: p. 44032.
84. Oh, J.E., S.M. Clark, H.R. Wenk and P.J.M. Monteiro, Experimental determination of bulk modulus of 14 angstrom tobermorite using high pressure synchrotron X-ray diffraction. *Cement and Concrete Research*, 2012. **42**(2): p. 397-403.
85. Shahsavari, R., M.J. Buehler, R.J.M. Pellenq and F.J. Ulm, First-principles study of elastic constants and interlayer interactions of complex hydrated oxides: case study of tobermorite and jennite. *Journal of the American Ceramic Society*, 2009. **92**(10): p. 2323-2330.
86. Oh, J.E., S.M. Clark and P.J.M. Monteiro, Does the Al substitution in C-S-H(I) change its mechanical property? *Cement and Concrete Research*, 2011. **41**(1): p. 102-106.
87. Moon, J., Oh, J. E., Balonis, M., Glasser, F. P., Clark, S. M., and Monteiro, P. J. High pressure study of low compressibility tetracalcium aluminum carbonate hydrates 3CaO· Al₂O₃· CaCO₃· 11H₂O. *Cement and Concrete Research*, 2012, **42**(1), 105-110.
88. Moon, J., Yoon, S., Wentzcovitch, R. M., Clark, S. M., and Monteiro, P. J. Elastic properties of tricalcium aluminate from high-pressure experiments and first-principles calculations. *Journal of the American Ceramic Society*, 2012, **95**(9), 2972-2978.
89. Oh, J. E., Moon, J., Mancio, M., Clark, S. M., & Monteiro, P. J. Bulk modulus of basic sodalite, Na₈ [AlSiO₄]₆ (OH)₂· 2H₂O, a possible zeolitic precursor in coal-fly-ash-based geopolymers. *Cement and Concrete Research*, 2011, **41**(1), 107-112.

90. Hargis, C. W., Moon, J., Lothenbach, B., Winnefeld, F., Wenk, H. R., & Monteiro, P. J. Calcium sulfoaluminate sodalite ($\text{Ca}_4\text{Al}_6\text{O}_{12}\text{SO}_4$) crystal structure evaluation and bulk modulus determination. *Journal of the American Ceramic Society*, 2014, 97(3), 892-898.
91. Puertas, F., M. Palacios, H. Manzano, J.S. Dolado, A. Rico and J. Rodriguez, A model for the C-A-S-H gel formed in alkali-activated slag cements. *Journal of the European Ceramic Society*, 2011. **31**(12): p. 2043-2056.

3. Materials and methods

3.1 Materials

Preparation of belite and its hydration system. Reagent grade SiO_2 , CaCO_3 , and K_2CO_3 powders were stoichiometrically mixed according to the composition of $1.8\text{CaO}-0.1\text{K}_2\text{O}-\text{SiO}_2$ to prepare monoclinic $\beta\text{-C}_2\text{S}$ [1]. The mixed powder was sintered at about $1500\text{ }^\circ\text{C}$ for three hours in a furnace and followed by air cooling. For the preparation of $\alpha'_\text{H}\text{-C}_2\text{S}$, reagent grade Ca_2SiO_4 and $\text{Ca}_3(\text{PO}_4)_2$ powders were mixed according to stoichiometric composition of $1.946\text{CaO}-0.892\text{SiO}_2-0.054\text{P}_2\text{O}_5$ [2]. The mixed powder was calcined at about $1450\text{ }^\circ\text{C}$ for six hours, then cooled in air. Note that, the calcination temperature used in this laboratory synthesis was much higher than the typical calcination temperature for belite-rich cement (e.g., $1250\text{ }^\circ\text{C}$ for belite-ye'elite-ferrite cement), because the higher calcination temperature favors the fast formation of phase-pure β - and α'_H - types of C_2S . The cooled C_2S pellets were then grounded into fine powders.

For ptychographic imaging and scanning transmission X-ray microscopy (STXM) study, anhydrous C_2S powders were mixed with deionized water ($18.2\text{ M}\Omega\cdot\text{cm}$) at a water-to-solid mass ratio (w/s) of 10. Such a high w/s ratio leads to the dispersion of anhydrous particles so that the thickness of the sample after drop-casting satisfied the saturation limit in the STXM [3]. The hydrated samples were sealed in polyethylene vials filled with N_2 gas (99.99%) at $25\pm 1\text{ }^\circ\text{C}$ to minimize carbonation. The $\alpha'_\text{H}\text{-C}_2\text{S}$ samples were cured at $25\text{ }^\circ\text{C}$ for 10 days and 40 days; while $\beta\text{-C}_2\text{S}$ samples were cured at $25\text{ }^\circ\text{C}$ for 17 days and 51 days. The suspension of $\sim 0.5\text{ }\mu\text{L}$ was dropped onto the center of a silicon frame ($5\text{ mm} \times 5\text{ mm}$, $100\text{ }\mu\text{m}$ thick), where a 100-nm -thick SiN membrane window ($1\text{ mm} \times 1\text{ mm}$) is in the center. The suspension was carefully and immediately absorbed using a tip of clean KimWipesTM on the edge of the Si wafer frame. The suspension removal procedure was monitored under an optical microscope to ensure that the particles remain on the SiN window. For the anhydrous C_2S , the powder was re-ground down to $1\text{-}5\text{ }\mu\text{m}$ by hand and then directly dusted on the SiN membrane windows. These windows were then placed on a stainless-steel sample stage for STXM inside a vacuum chamber.

Preparation of nanocrystalline C-(A-)S-H. C-(A-)S-H samples were synthesized with initial bulk molar Ca/Si ratios (Ca/Si^*) of 0.6, 0.8, 1.0, 1.2, 1.4 and 1.6, initial bulk molar Al/Si ratios (Al/Si^*) of 0 and 0.05. The stoichiometric amounts of nano silica fume (SiO_2 , Aerosil 200, Evonik), CaO (prepared by calcining calcite (Merck Millipore) at $1000\text{ }^\circ\text{C}$ for 12 h) and $\text{CaO}\cdot\text{Al}_2\text{O}_3$ were mixed with Millipore water with w/s of 45 in a N_2 -filled glove box [4] [5]. These sample were equilibrated at $20\text{ }^\circ\text{C}$ for 182 days. Additional samples with $\text{Ca/Si}^* = 1$ and Al/Si^* of 0, 0.05 and 0.1 were water bathed at $7\text{ }^\circ\text{C}$ for one year, and at $50\text{ }^\circ\text{C}$ and $80\text{ }^\circ\text{C}$ for 56 days. Except $80\text{ }^\circ\text{C}$ samples which were cured in Teflon bottles, all other samples were cured in high-density polyethylene (HDPE) bottles. The solids were vacuum filtered in a N_2 -filled glove box using $0.45\text{ }\mu\text{m}$ nylon filters, rinsed with a 50% v/v ethanol / Millipore water solution, then with 94 vol.% ethanol solution, and freeze-dried for seven days. The dry solids were then stored in N_2 -filled desiccators in the presence of saturated CaCl_2 solutions at relative humidity (RH) of about 30%.

For ptychographic and STXM studies, the C-(A-)S-H solid samples were mixed and dispersed with isopropanol (>99.5%, Fisher Chemical) at a liquid-to-solid mass ratio of 10 in polystyrene weighing boats (Fisherbrand). The suspension of 0.5 μL was also dropped in onto a silicon frame and sandwiched by another frame on top. The edge of two silicon frames were sealed with epoxy. The protocol was used to stabilize the samples on the windows and reserve their morphology.

Preparation of nanocrystalline C-N-(A-)S-H. Similar to the preparation of C-(A-)S-H, nanocrystalline C-N-(A-)S-H samples were synthesized at an initial bulk molar Ca/Si ratio of 1 and initial bulk molar Al/Si ratios of 0 to 0.1 using 0.5 M NaOH solution (Merck Millipore). The solid precursors CaO, SiO₂ (Aerosil 200, Evonik), and CaO·Al₂O₃ were stoichiometrically mixed with NaOH solution in a N₂-filled glovebox at a liquid-to-solid mass ratio of 45 [6]. The samples were equilibrated at 50 °C in polyethylene vials for 56 days and shaken twice per week. Then the samples were vacuum filtered in a N₂-filled glovebox using 0.45 μm nylon filters and freeze-dried for seven days. Subsequently, the dry solids were stored in N₂-filled desiccators in the presence of saturated CaCl₂ solutions at ~30% RH. The degree of superficial carbonation of the samples was measured to be less than 2 wt.%. The mean silicate chain lengths of the C-N-S-H and C-N-A-S-H samples were measured to be ~3 and ~7, respectively, by ²⁹Si NMR.

3.2 Experimental methods

Scanning Transmission X-ray Microscopy. The STXM experiments were conducted at the bending magnet beamlines 5.3.2.2 (Ca L_{2,3}-edge) and 5.3.2.1 (Si K-edge) at the Advanced Light Source (ALS) at Lawrence Berkeley National Laboratory (LBNL). The STXM beamlines use brilliant synchrotron X-ray radiation as the incident beam (~500 mA current). The monochromatic X-ray is focused using a zone plate onto the samples that are mounted on a multi-motor stage inside a vacuum chamber (base pressure of 200 mTorr) [7] [8]. In the range of Ca L_{2,3}-edge, the X-ray beam was scanned from 342 eV to 360 eV with an energy step of 0.1 eV to obtain X-ray absorption near edge structure (XANES) spectra; around Si K-edge, the beam was scanned from 1830 to 1880 eV with an energy step size of 0.1 eV from 1842 to 1870 eV and step size of 0.3 eV in the other energy ranges. The dwell time was 3-4 ms used in area-unidirectional mode, 4 ms for line scan unidirectional mode, and 30-50 ms for line scan point-by-point mode.

Image contrast maps were achieved by differential measurements at two energies, below and on the edge at a spatial resolution down to 25 nm. Image stacks were collected by scanning the same sample area at each point of the pre-defined energy ranges depending on expected feature sharpness [9]. Image stack can provide a XANES spectrum of each pixel on the whole region of interest (ROI). Each data point on a XANES spectrum represents an averaged normalized optical density (OD) at a specific photon energy value of all pixels contained in a ROI. Brightness, or OD, is governed by the composition, density, and thickness of the samples. It is calculated at each pixel via the Beer-Lambert law, as a linear log of the ratio between the averaged transmitted photon intensity of background and the transmitted X-ray photon intensity [10]. Axis 2000 program was used to align image stacks, to compute element maps, and to process XANES spectra. The RGB overlay maps which visualize and quantify phases containing various

chemical compositions were drawn by using singular value decomposition (SVD) based on the reference spectra [11].

X-ray Ptychography. Soft X-ray ptychographic images were collected at ~ 800 eV at bending magnet beamline 5.3.2.1 at ALS, using the same STXM setup mentioned above but a fast CCD camera was used [12]. The scanning step size 40 nm was smaller than the beam spot size 60 nm, leading to greatly overlapped areas among the adjacent illuminated spots. The ptychographic images were pre-processed and reconstructed using cluster-based codes for both the real and imaginary parts of the transmitted beam. Magnitude images were yielded with pixel size of ~ 5 nm. The estimated effective spatial resolution of the images was ~ 10 nm [13].

For the quantification of the morphological information obtained from X-ray ptychographic magnitude images, small angle scattering (SAS) pattern was calculated using an ImageJ plugin code [14]. A Guinier–Porod lamellar model was used to fit the SAS patterns, which provide the sizes of the synthetic C-(A-)S-H nano-globule [15]. More details are available in the appendix (Chapter 8).

ImageJ was also used to obtain the width and length of C-S-H fiber/foil in ptychographic images (magnitude mode) by measuring the number of pixels of each morphological feature (fibers or foils).

Wide Angle X-ray Scattering. Wide Angle X-ray Scattering (WAXS) experiment was carried out at the Beamline 1.3W at Synchrotron Light Research Institute (SLRI), Thailand. The X-ray beam energy was 9 keV (wavelength of ~ 1.378 Å), with a current of ~ 100 mA. Two pieces of Kapton film was glued between a stainless-steel sample holder (1 cm by 1 cm aperture with thickness of ~ 0.5 mm.), and dry C-A-S-H samples were evenly sandwiched between the Kapton films. A blank sample holder with two pieces of Kapton films was measured for the subtraction of the background scattering from Kapton film. The sample-to-detector distance of WAXS experiment was 0.094 m with effective Q-range of 4.38 – 32.12 nm $^{-1}$.

High-pressure X-ray diffraction. High-pressure X-ray diffraction (HP-XRD) experiment was conducted at superbend beamline 12.2.2 at ALS. A synchrotron-source X-ray beam with energy of 25 keV (wavelength of 0.4959 Å) was used. The sample-to-detector distance and beam wavelength was calibrated with CeO₂ powder standard. Two-dimensional diffraction patterns were recorded on a MAR345 high-resolution CCD detector, with an exposure time of 480 s to 960 s under laboratory conditions. Each C-N-(A-)S-H powder sample was compressed using two tungsten carbide cubes by hand, and then loaded into a chamber (150 μ m diameter and 80 μ m thickness) in a stainless-steel gasket [16]. 1-3 ruby (α -Al₂O₃ doped with 0.05 wt.% Cr³⁺) fine spheres as a gauge of hydrostatic pressure were then placed on the diamond culet. The chamber was then immersed by a drop of pressure-transmitting medium (4:1 v/v methanol/ethanol solution) in the chamber before the closure of two diamond anvils [17]. The hydrostatic pressure ranged from 0 GPa to ~ 10 GPa with an increment of 1-2 GPa. The hydrostatic pressure of sample at each pressure point was determined using ruby fluorescence method. A BX90 diamond anvil cell was used in this study for pressurized samples. At ambient pressure (~ 0 GPa), samples were loaded in borosilicate glass capillaries (0.3-0.7 mm diameter). The two-dimensional

diffraction data were first integrated using Dioptas. Then diffraction patterns were processed using XFIT, Celref, and MAUD [18, 19].

Both the third-order (Equation 3.1) and the second-order (Equation 3.2) Birch–Murnaghan equations of state (BM-EoS), can be used to fit the correlation between the applied hydrostatic pressure and the volume of unit cell of the samples. The second-order BM-EoS is more often used to calculate the initial bulk moduli (K_0) of cementitious materials in the HP-XRD studies because 1) the pressure derivative K'_0 for many materials often approaches four; 2) the use of the third-order BM-EoS for low-pressure range (typically below 10 GPa) often yields unrealistic calculated K'_0 (e.g., too high, too low, or even negative values) [20].

$$P = \frac{3}{2} K_0 [(1 - \varepsilon_V)^{-\frac{7}{3}} - (1 - \varepsilon_V)^{-\frac{5}{3}}] [1 + \frac{3}{4} (K'_0 - 4)(\varepsilon_V^{-\frac{2}{3}} - 1)] \quad \text{Equation 3.1}$$

$$P = \frac{3}{2} K_0 [(1 - \varepsilon_V)^{-\frac{7}{3}} - (1 - \varepsilon_V)^{-\frac{5}{3}}] \quad \text{Equation 3.2}$$

where P is the hydrostatic pressure applied to a sample (GPa), ε_V is the volumetric strain of a unit cell ($\text{\AA}^3/\text{\AA}^3$, unitless), K_0 is the initial bulk modulus at ambient pressure (GPa), K'_0 is the pressure derivative of bulk modulus at ambient pressure (unitless), and K'_0 is fixed at four in the second-order BM-EoS (Equation 3.2).

3.3 References

1. Jost, K.H., et al., Redetermination of the structure of beta-dicalcium silicate. *Acta Crystallographica Section B: Structural Crystallography and Crystal Chemistry*, 1977. **33**(6): p. 1696-1700.
2. Jelenic, I. and A. Bezjak, On the Hydration Kinetics of Alpha-'-Modifications and Beta-Modifications of Dicalcium Silicate. *Cement and Concrete Research*, 1981. **11**(3): p. 467-471.
3. Bae, S., R. Taylor, D. Hernandez-Cruz, S. Yoon, D. Kilcoyne and P.J.M. Monteiro, Soft X-ray Spectromicroscopic Investigation of Synthetic C-S-H and C3S Hydration Products. *Journal of the American Ceramic Society*, 2015. **98**(9): p. 2914-2920.
4. Myers, R.J., E. L'Hopital, J.L. Provis and B. Lothenbach, Effect of temperature and aluminium on calcium (aluminosilicate) hydrate chemistry under equilibrium conditions. *Cement and Concrete Research*, 2015. **68**: p. 83-93.
5. L'Hôpital, E., B. Lothenbach, D. Kulik and K. Scrivener, Influence of calcium to silica ratio on aluminium uptake in calcium silicate hydrate. *Cement and Concrete Research*, 2016. **85**: p. 111-121.
6. Myers, R.J., E. L'Hopital, J.L. Provis and B. Lothenbach, Composition-solubility-structure relationships in calcium (alkali) aluminosilicate hydrate (C-(N,K-)A-S-H). *Dalton Transactions*, 2015. **44**(30): p. 13530-13544.
7. Shapiro, D.A., Y.-S. Yu, T. Tyliczszak, J. Cabana, R. Celestre, W. Chao, K. Kaznatcheev, A.D. Kilcoyne, F. Maia and S. Marchesini, Chemical composition mapping with nanometre resolution by soft X-ray microscopy. *Nature Photonics*, 2014. **8**(10): p. 765-769.
8. Kilcoyne, A.L.D., T. Tyliczszak, W.F. Steele, S. Fakra, P. Hitchcock, K. Franck, E. Anderson, B. Harteneck, E.G. Rightor, G.E. Mitchell, A.P. Hitchcock, L. Yang, T.

- Warwick and H. Ade, Interferometer-controlled scanning transmission X-ray microscopes at the Advanced Light Source. *Journal of Synchrotron Radiation*, 2003. **10**: p. 125-136.
9. Kilcoyne, D., et al., A new scanning transmission X-ray Microscope at the ALS for operation up to 2500 eV. *AIP Conference Proceedings*, 2010: p. 465.
 10. Geng, G., R.J. Myers, A.L. Kilcoyne, J. Ha and P.J. Monteiro, Ca L2, 3-edge near edge X-ray absorption fine structure of tricalcium aluminate, gypsum, and calcium (sulfo) aluminate hydrates. *American Mineralogist*, 2017. **102**(4): p. 900-908.
 11. Li, Q.G., Y.; Geng, G.; Bae, S.; Monteiro, P. J. M.; CaCl₂-Accelerated Hydration of Tricalcium Silicate: A STXM Study Combined with ²⁹Si MAS NMR. *Journal of Nanomaterials*, 2015. **2015**: p. 1-10.
 12. Geng, G., J. Li, Y.-S. Yu, D.A. Shapiro, D.A. Kilcoyne and P.J. Monteiro, Nanometer-Resolved Spectroscopic Study Reveals the Conversion Mechanism of CaO· Al₂O₃· 10H₂O to 2CaO· Al₂O₃· 8H₂O and 3CaO· Al₂O₃· 6H₂O at an Elevated Temperature. *Crystal Growth & Design*, 2017. **17**(8): p. 4246-4253.
 13. Geng, G., R.J. Myers, Y.S. Yu, D.A. Shapiro, R. Winarski, P.E. Levitz, D.A.L. Kilcoyne and P.J.M. Monteiro, Synchrotron X-ray nanotomographic and spectromicroscopic study of the tricalcium aluminate hydration in the presence of gypsum. *Cement and Concrete Research*, 2018. **111**: p. 130-137.
 14. Geng, G., R.J. Myers, J. Li, R. Maboudian, C. Carraro, D.A. Shapiro and P.J. Monteiro, Aluminum-induced dreierketten chain cross-links increase the mechanical properties of nanocrystalline calcium aluminosilicate hydrate. *Scientific Reports*, 2017. **7**: p. 44032.
 15. Hammouda, B., A new Guinier–Porod model. *Journal of Applied Crystallography*, 2010. **43**(4): p. 716-719.
 16. Geng, G.Q., R.J. Myers, M.J.A. Qomi and P.J.M. Monteiro, Densification of the interlayer spacing governs the nanomechanical properties of calcium-silicate-hydrate. *Scientific Reports*, 2017. **7**.
 17. Moon, J.H., J.E. Oh, M. Balonis, F.P. Glasser, S.M. Clark and P.J.M. Monteiro, Pressure induced reactions amongst calcium aluminate hydrate phases. *Cement and Concrete Research*, 2011. **41**(6): p. 571-578.
 18. Martorana, A., Gerbasi, R., Marigo, A., and Zannetti, R. XFIT: A package for simulating and fitting x-ray powder diffraction patterns. *Computer Physics Communications*, 1984. **34**(1-2): p. 145-151
 19. Lutterotti, L., and Bortolotti, M. Object oriented programming and fast computation techniques in Maud, a program for powder diffraction analysis written in java. *IUCr: Compcomm Newsletter*, 2003. 1, p. 43-50.
 20. Gatta, G.D., Does porous mean soft? On the elastic behaviour and structural evolution of zeolites under pressure. *Zeitschrift Fur Kristallographie*, 2008. **223**(1-2): p. 160-170.

4. Hydration of belite polymorphs

Belite (C_2S) is a clinker mineral in both Portland cement and belite-ye'elinite-ferrite (BYF) cement [1] [2]. BYF mainly contains belite (C_2S), ye'elinite ($Ca_4Al_6O_{12}SO_3$), ferrialuminate ($Ca_4Al_2Fe_2O_{10}$), and gypsum or calcium sulfate. The reactions between gypsum and ye'elinite and between gypsum and ferrialuminate in the BYF cement both yield ettringite needles and aluminite hydroxide gel, forming an Al-rich pore solution. The hydraulic reactivity of C_2S is lower than that of hydration of ye'elinite. The hydration of C_2S in such Al-rich environment may not generate C-S-H, but the reaction contributes to the precipitation of stratlingite ($Ca_2Al_2O_5 \cdot 8H_2O$) plate-like crystallites. The reactions in the multiphase cement hydration system is very complicate, thus understanding the reaction of C_2S can be the first step to study the hydration of BYF cement.

The hydraulic reactivity of β - C_2S (the most common polymorph of C_2S) is significantly lower than that of C_3S [3]. The low reactivity of β - C_2S limits the development of high-belite Portland cement and BYF cement. α'_H - C_2S is a more hydraulically reactive polymorph relative to β - C_2S , but the stabilization and formation of α'_H - C_2S during and after calcination rely on foreign ions (e.g., boron and phosphorus) [4]. Existing literature mainly focuses on the stability and hydraulic relativity of anhydrous C_2S polymorphs [5] [6]. There is a lack of studies on the morphology and chemistry of their hydration products, particularly for those of α'_H - C_2S . In this chapter, the chemical environments of Ca and Si of C-S-H in hydration system of β - C_2S and α'_H - C_2S are studied. The morphological difference between the two hydration systems is compared.

4.1 Ca coordination of anhydrous β - C_2S and hydrated β - C_2S at 17 days

Figure 4.1 shows the Ca $L_{2,3}$ -edge XANES spectra, which consist of two major peaks, L_3 $2P_{3/2}$ (a_2) and L_2 $2P_{1/2}$ (b_2) measured at beamline 5.3.2.2 at ALS. The major peaks are attributed to the degeneracy loss of 2p orbitals of Ca by spin-orbital interactions, along with three minor leading peaks, a_0 , a_1 , and b_1 , in order of an increased photon energy [7]. The energy difference between major and minor peaks (a_2 - a_1 (ΔL_3) and b_2 - b_1 (ΔL_2), also termed splitting energy) and the intensity of the minor peaks are controlled by the symmetry of Ca in the first coordination shell and its structural ordering at atomic scale [8] [9] [10].

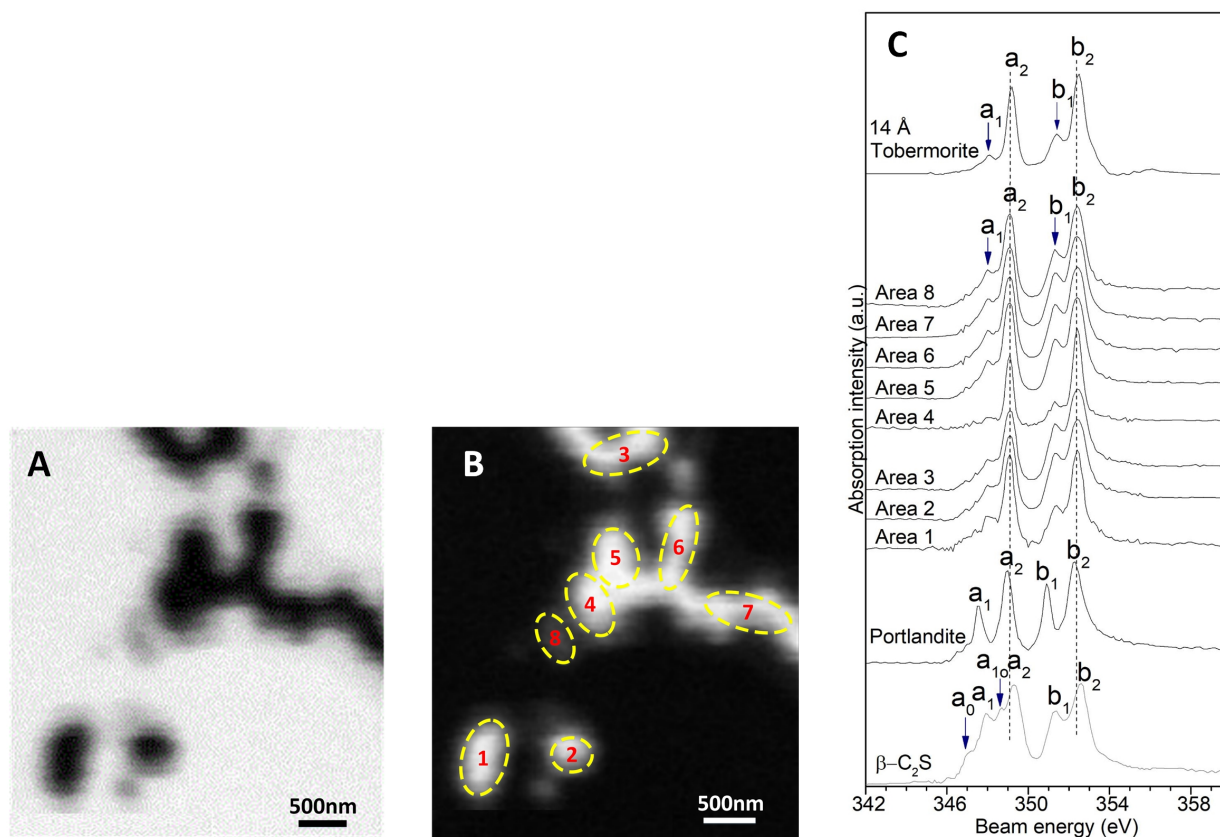


Figure 4.1. Hydrated β -C₂S cured at 25 °C for 17 days: (A) Transmission image of the ROI taken at 349 eV; (B) Ca element mapping with the selected areas for the XANES spectra; (C) Ca L_{2,3}-edge XANES spectra extracted from different areas specified in (B).

The Ca L_{2,3}-edge XANES spectrum of anhydrous monoclinic β -C₂S is shown in Figure 4.1 (C). The Ca atoms in anhydrous β -C₂S results in a tiny peak a_{10} located between a_1 and a_2 , and the peak energy differences of $a_2 - a_1$ and $b_2 - b_1$ are 1.54 and 1.2 eV, respectively. These large energy differences and the existence of a_{10} peak in β -C₂S suggest a typical cubic-like symmetry of Ca [11]. β -C₂S contains seven-fold and eight-fold coordinated Ca, which are denoted as Ca1 and Ca2 in Figure 4.2. The equatorial plane of Ca1 is parallel to (10 $\bar{1}$) plane and Ca-O bond lengths of Ca1 ranges from 2.273 to 2.892 Å with an average value of 2.528 Å [12]. The five equatorial O atoms (O1, O2, O3, and O4) are not exactly coplanar. The Ca2 has a distorted cubic symmetry, where the two trapezoids formed of the top four O atoms (O1, O2, O3, and O4) and bottom four O atoms (O1, O2, O3, and O4) are misaligned along the diagonal direction of each other by $\sim 55^\circ$. The Ca-O bond length of Ca2 shell ranges from 2.40 to 2.676 Å with an average value of 2.503 Å. The superposition of the complex coordination of Ca1 and Ca2 atoms in anhydrous β -C₂S contributes to a weak cubic-like crystal field splitting effect [7].

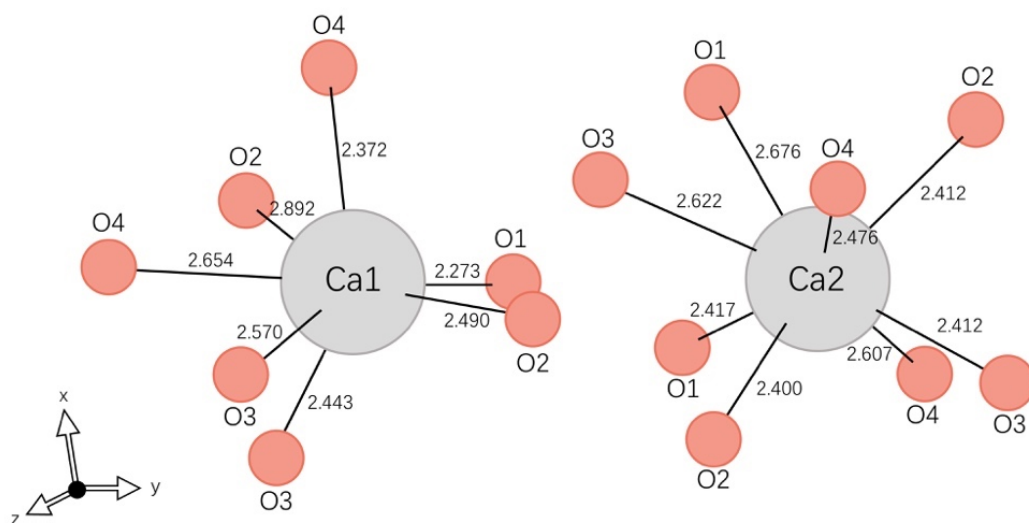


Figure 4.2 Coordination environment of Ca in anhydrous β -C₂S. Bond length of Ca-O pairs is given in angstrom.

Ca L_{2,3}-edge at \sim 349 eV only allows a low transmission depth, thus, to avoid X-ray absorption saturation, only particles with grain size below 1 μ m (see Figure 4.1B) were measured for the Ca L_{2,3}-edge. The Ca L_{2,3}-edge XANES spectra of all hydrated β -C₂S particles cured at 25 $^{\circ}$ C for 17 days exhibited mostly identical peak positions and an equivalent splitting energy. The similar spectroscopic features indicated that the bulk Ca in all particles exhibits a comparable atomic structure. a₂ and b₂ peaks in the selected areas are \sim 0.1 eV lower than those of anhydrous β -C₂S, suggesting that the oxidation degree of Ca in C-S-H in hydrated β -C₂S is lower than that of anhydrous β -C₂S, namely coordination number of Ca-O of C-S-H is lower than that of anhydrous β -C₂S. The splitting energies of hydrated β -C₂S at 17 days are 1.05-1.1 eV, suggesting a distorted octahedral-like symmetry of Ca in hydrated β -C₂S [9]. The X-ray absorption features (i.e., peak positions and splitting energy) resemble those of 14 \AA tobermorite (Ca₅Si₆O₁₆(OH)₂ · 7H₂O) [13], suggesting that Ca environment in C-S-H precipitated in β -C₂S hydration system is similar to that of 14 \AA tobermorite.

The ratios of relative intensity of peak a₁-to-a₂ (I(a₁)/I(a₂)) and b₁-to-b₂ (I(b₁)/I(b₂)) of hydrated β -C₂S are 0.021-0.041 and 0.050-0.077, respectively, which are lower than those of synthetic C-S-H equilibrated at 20 $^{\circ}$ C (0.05-0.15 for I(a₁)/I(a₂) and 0.07-0.15 for I(b₁)/I(b₂)) [14]. The details in the calculation of relative intensity of these peaks are shown in Figure S1 (Appendix). Synthetic C-S-Hs typically possess a much longer range of ordering than hydration product C-S-H in the β -C₂S hydration along the c-axis [15]. The lower relative intensity ratio suggests a shorter range of ordering for Ca in β -C₂S hydration system relative to synthetic C-S-H. Besides, the contribution of portlandite was not observed in the XANES spectra, suggesting that C-S-H does not intermix with portlandite at the 25 nm-scale, and the interlayer six-fold coordinated Ca of hydration product C-S-H is also highly distorted. Otherwise, the splitting energy of the selected areas would be much higher. Thus, the Ca environment of C-S-H in β -C₂S hydration system is short-range-ordered and tobermorite-like. Portlandite micro crystallites were clearly observed in this dilute hydration system in Figure 4.3.

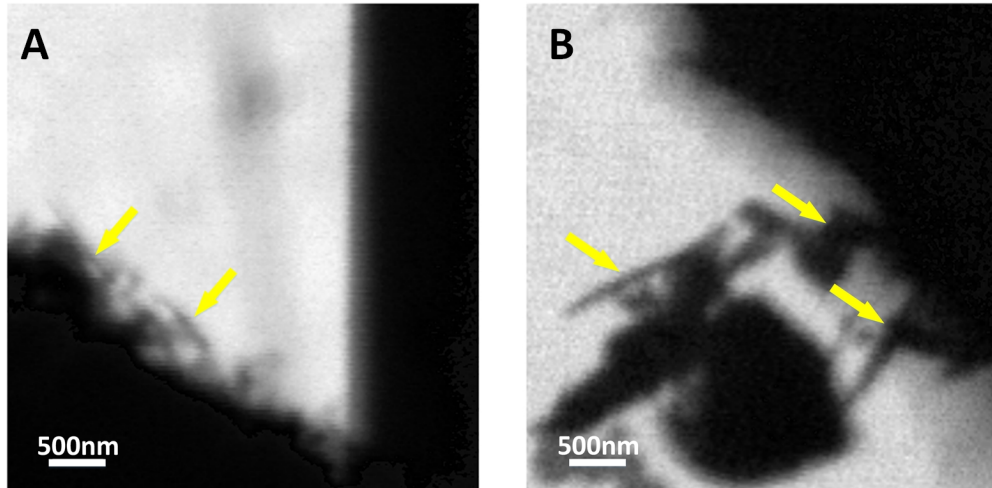


Figure 4.3 Transmission images taken at 349 eV, (A) hydrated β -C₂S at 17 days, the right dark area is the edge of Si₃N₄ membrane; (B) hydrated α' _H-C₂S at 10 days. Portlandite crystallites are indicated by yellow arrows.

Previous study of hydrated C₃S at 17 days also exhibited similar energy positions of peaks, splitting energies, and peak intensity ratios at Ca L_{2,3}-edge in XANES spectra [16], suggesting that the Ca environment of C-S-H in C₃S hydration system is comparable to hydrated β -C₂S. An extended X-ray absorption fine structure study indicated that the Ca coordination of hydrated β -C₂S is similar to 11 Å tobermorite, while the coordination number of Ca and Ca-O bond length of C-S-H could not be fitted due to the Ca contribution from intermixed portlandite [17]. An ¹⁷O nuclear magnetic resonance study suggested that Ca-OH sites exist in C-S-H in β -C₂S hydration system [18]. Richardson [19] proposed that the C-S-H molecular structure contains six- and seven-fold coordinated Ca in the interlayer and calcium silicate basal layer, respectively. Gartner et al. [20] suggested that the interlayer Ca of C-S-H in both hydration systems of β -C₂S and C₃S are six-fold coordinated. The highly distorted six-fold coordinated Ca in the interlayer of C-S-H in β -C₂S hydration system fits both above-mentioned models.

4.2. Ca coordination of anhydrous α' _H-C₂S and hydrated α' _H-C₂S at 10 days

Figure 4.4 shows the XANES spectrum of anhydrous orthorhombic α' _H-C₂S Ca L_{2,3}-edge. The spectrum with splitting energy a₂-a₁ of 1.57 eV and b₂-b₁ of 1.25 eV and a₁₀ peak suggested a cubic-like symmetry of Ca in anhydrous α' _H-C₂S [9]. Anhydrous α' _H-C₂S has two Ca sites with nine- and eight-fold coordination, which are denoted as Ca1 and Ca2 in Figure 4.4 [5]. The Ca-O bond lengths of Ca1 range from 2.214 to 3.175 Å with an average value of 2.708 Å, and Ca-O bond lengths of Ca2 range from 2.292 to 2.927 Å with an average value of 2.545 Å. The superposition of complex coordination of α' _H-C₂S yields a cubic-like crystal field splitting. The splitting energy of anhydrous α' _H-C₂S was slightly higher relative to anhydrous β -C₂S, indicating that Ca-O complexes in α' _H-C₂S are more similar to cubic-like symmetry (less distorted) than in those in β -C₂S. This is because Ca1 in β -C₂S is coordinated with seven O atoms, which are incapable of allowing an ideal cubic symmetry for anhydrous β -C₂S.

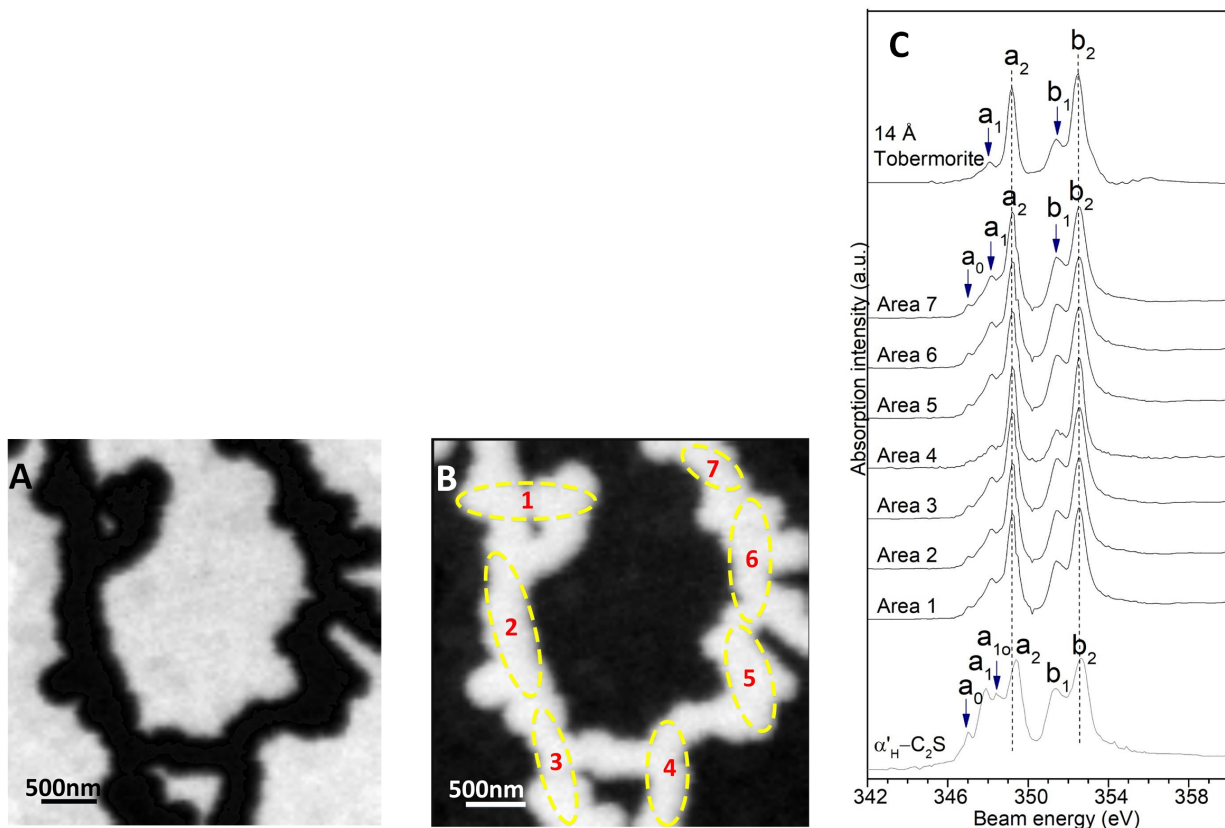


Figure 4.4 Hydrated $\alpha'_H\text{-C}_2\text{S}$ cured at 25 °C for 10 days: (A) Transmission image of the ROI taken at 349 eV; (B) Ca element mapping with the selected areas for the XANES spectra; (C) Ca L_{2,3}-edge XANES spectra extracted from different areas specified in (B).

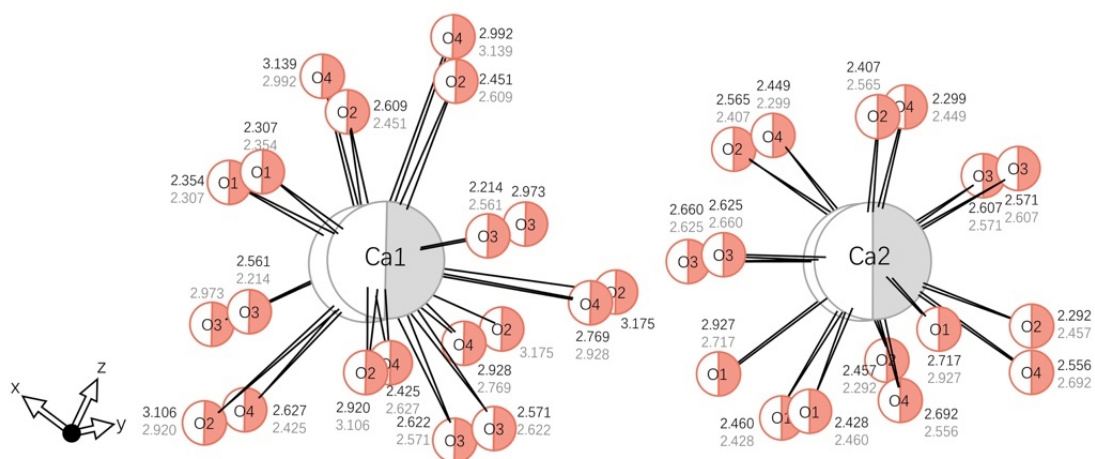


Figure 4.5 Coordination environment of Ca in anhydrous $\alpha'_H\text{-C}_2\text{S}$. Bond length of Ca-O pairs are all in angstrom.

Portlandite was not observed in this ROI for hydrated $\alpha'_H\text{-C}_2\text{S}$ cured at 25 °C for 10 days at 25 nm scale. The Ca L_{2,3}-edge XANES spectra of all hydrated $\alpha'_H\text{-C}_2\text{S}$ particles at 10 days exhibited mostly identical peak positions and an equivalent splitting energy. Peaks a₂ and b₂ in the selected areas are ~ 0.1 eV lower than those of hydrous $\alpha'_H\text{-C}_2\text{S}$, and the peak positions are 0.05 eV higher than for hydrated $\beta\text{-C}_2\text{S}$. The splitting energies of hydrated $\alpha'_H\text{-C}_2\text{S}$ are ~0.1 eV lower than those of $\alpha'_H\text{-C}_2\text{S}$ but ~0.05 eV higher than hydrated $\beta\text{-C}_2\text{S}$. This fact suggested that the Ca-O bond strength of C-S-H in hydrated $\alpha'_H\text{-C}_2\text{S}$ is slightly higher than C-S-H in hydrated $\beta\text{-C}_2\text{S}$; namely, more six-fold coordinated Ca is present in the $\alpha'_H\text{-C}_2\text{S}$ hydration system. The lower content of interlayer Ca in hydrated $\beta\text{-C}_2\text{S}$ relative to that of hydrated $\alpha'_H\text{-C}_2\text{S}$ can be explained by the incorporation of K (from the dissolution of dopant K in anhydrous $\beta\text{-C}_2\text{S}$) in the interlayer of hydration product C-S-H in hydration of $\beta\text{-C}_2\text{S}$. The relative intensity ratios of peaks in hydrated $\alpha'_H\text{-C}_2\text{S}$ are 0.018-0.038 and 0.037-0.067, which are also lower than those of anhydrous $\alpha'_H\text{-C}_2\text{S}$ but similar to or slightly lower than C-S-H in hydrated $\beta\text{-C}_2\text{S}$. These absorption features suggested that the coordination symmetry of Ca of C-S-H in hydrated $\alpha'_H\text{-C}_2\text{S}$ system is also tobermorite-like, but its ordering of Ca is slightly weaker than that in hydrated $\beta\text{-C}_2\text{S}$ at 17 days.

4.3 Si environment of anhydrous $\beta\text{-C}_2\text{S}$ and hydrated $\beta\text{-C}_2\text{S}$ at 17 days

Figure 4.6C shows the XANES spectra around the Si K-edge of anhydrous $\beta\text{-C}_2\text{S}$ and hydrated $\beta\text{-C}_2\text{S}$ at 17 days. The Si K-edge of $\beta\text{-C}_2\text{S}$ is attributed to the electronic excitation from 1s to the antibonding 3p-like state orbital (t_2) of four-fold coordinated Si [21] [22]. Pre-edge peak a₀ is assigned to the dipole-forbidden transition of 1s orbital to the antibonding 3s-like states [23]. This forbidden peak appears due to the mixing of s- and p- states when the tetrahedral coordination of Si is highly distorted. Thus, the intense a₀ peak of anhydrous $\beta\text{-C}_2\text{S}$ suggested a strong distortion of silicate tetrahedron. The minor peak of a₂ is assigned to the multiple-scattering effect from more distant coordination shells through a photoelectron interaction; a₂ peak position is governed by the structural complexity and interatomic distance [24].

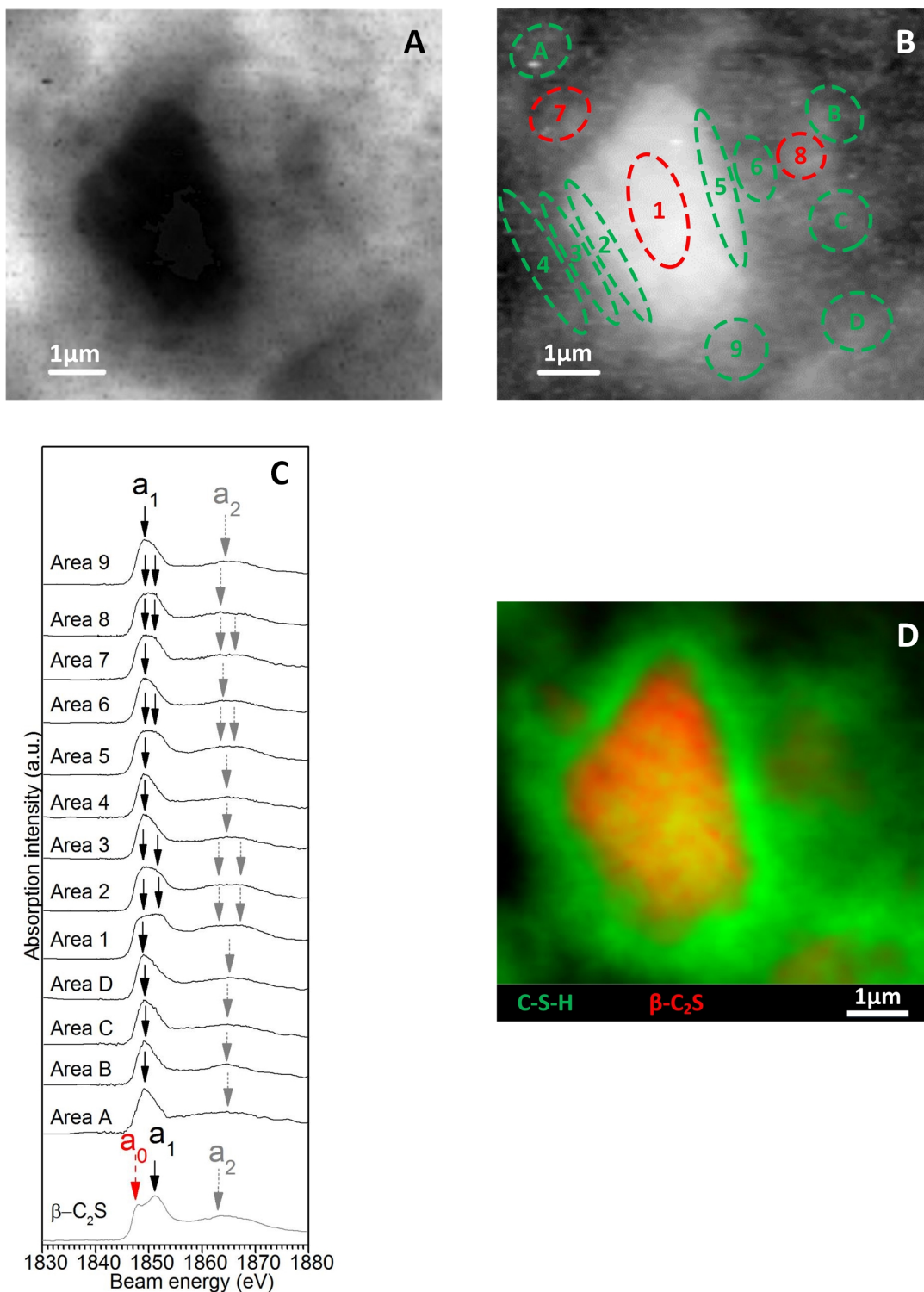


Figure 4.6 Hydrated β -C₂S cured at 25 °C for 17 days: (A) Transmission image of the ROI taken at 1849 eV; (B) selected areas in the Si element mapping from the XANES spectra; (C) Si K-edge XANES spectra extracted from different areas specified in (B); (D) RGB overlay map using XANES spectra obtained from the C-S-H (Area 4, green) marked in (B) and reference spectrum of anhydrous β -C₂S (red). More RGB over maps can be found in Appendix.

At 17 days, the interface between anhydrous β -C₂S core and the hydration product layer is well distinguished (Figure 4.6A), indicating changes in the optical density. The OD of the hydration product layer slightly decreases with an increased distance from the interface, which is associated with several small brighter regions. Compared to C₃S hydration system [16], the C-S-H of hydrated β -C₂S is more dispersed, and C-S-H fibrils are not present at this age and at this resolution (Figure 4.6A).

Peak a_1 is not shown at ~ 1851.1 eV in areas 3, 4, 6 but a single a_1 peak is observed at 1848.8 eV in these areas (Figure 4.6C), suggesting that C-S-H is the only siliceous phase in these areas. The absorption features of C-S-H in hydrated β -C₂S resemble those of C-S-H in hydration system of C₃S [16] [25] [26]. The Si K-edge (a_1 peak) at 1848.8 eV of C-S-H is ~ 2.2 eV lower than that of β -C₂S due to the longer Si-O bond of the C-S-H relative to anhydrous β -C₂S [27] [28]. Li et al. [21] concluded that although there is significant overlapping for silicate minerals with different polymerization types, the Si K-edge generally shifts to higher energy with an increased degree of silicate polymerization. Thus, in this case, the Si-O bond length, instead of the polymerization degree, dominates the energy shift of Si K-edge.

The energy difference between a_1 and a_2 , Δa_2-a_1 , is often used to evaluate the degree of silicate polymerization of C-S-H [14] [26] [16] [25]. The values of Δa_2-a_1 for areas 3 and 4 are equivalent, suggesting that the degree of silicate polymerization of the C-S-H here is comparable. The energy positions of multiple scattering peaks (i.e., a_2) are affected by the Si interatomic distances, while the intensity and number of resonances are heavily dependent on the bond angle, site symmetry, and number of nearest neighboring oxygen atoms (Si species in most cement phases are four-fold coordinated, except thaumasite (Ca₃Si(OH)₆(CO₃)(SO₄) · 12H₂O), where Si atoms are six-fold coordinated) [29]. Two a_2 peaks are distinguished in the XANES spectra in areas 2 and 5. In these areas, a peak at 1848.8 eV and a broad hump/shoulder at ~ 1851.1 eV were observed, the peak is assigned to the a_1 peak of C-S-H, and the hump/shoulder is assigned to the contribution of a_1 peak (at 1851.0 eV) of anhydrous β -C₂S. These absorption features suggest that areas 2 and 5 are mixtures of C-S-H and anhydrous β -C₂S, and the hydration here is not complete. Similarly, areas 7 and 8 are mixtures of C-S-H and anhydrous β -C₂S, indicating that fine β -C₂S grains exist in these areas. This fact is consistent with the original granulometry result of β -C₂S, $\sim 10\%$ of β -C₂S was below 1 μm . Note that a weak contribution of C-S-H to the spectrum at ~ 1848.8 eV is observed in area 1 since C-S-H layer surrounds the entire grain. Δa_2-a_1 of area 6 is 0.9 eV lower than those of areas 3 and 4 (~ 15.7 eV), suggesting a lower degree of silicate polymerization of C-S-H in area 6. The difference in local polymerization degree can be explained by the different dissolution rates on the crystal faces and by different numbers of surface defects of foreign ion (in this case K) doped β -C₂S [30]; multiple crystal faces with low hydraulic reactivity occur in area 6. Note that, hydraulic reactivity of all faces of pure anhydrous β -C₂S is similar; the dopant changes the local reactivity of β -C₂S crystals [31]. Similarly, the value of Δa_2-a_1 of C-S-H in area 9 is 0.7 eV lower than for C-S-H in the unconstrained space. The RGB overlay map (Figure 4.6D) shows that the C-S-H surrounds the unreacted core, which is consistent with the analysis above. The values of Δa_2-a_1 for C-S-H among different grains (Areas A- D) are 15.6-16.1 eV, indicating a distinction in degree of silicate polymerization due to the interference of other grains and the hydration rate. In addition, the contribution of cross-linking sites to the spectra is not observed in the typical range at 1853-

1854 eV [32] since the calcium silicate basal layers of C-S-H are separated by interlayer $[\text{Ca}(\text{H}_2\text{O})_6]^{2+}$ or $[\text{Ca}(\text{OH})(\text{H}_2\text{O})_5]^+$ [20]. ^{29}Si NMR studies showed that the mean silicate chain lengths of C-S-H of hydrated $\beta\text{-C}_2\text{S}$ for 7-12 months are still lower than 3.5 [33]. This suggests that the proportion of long silicate chains (octamer or even longer) in this C-S-H is relatively low. Therefore, the C-S-H of hydrated $\beta\text{-C}_2\text{S}$ at 17 days is mainly a mixture of dimer and pentamer C-S-Hs.

It is well known that the degree of silicate polymerization of synthetic C-S-H increases as mean Ca/Si ratio decreases [34] [35]. Although the degree of silicate polymerization of hydrated $\beta\text{-C}_2\text{S}$ progressively increases over time [18] [6], there is no significant variation in the mean Ca/Si molar ratio of Op (excluding intermixed portlandite) with age [36]. Thus, it is difficult to estimate the local degree of silicate polymerization merely based on Ca/Si ratio. STXM is a more reliable technique to locally probe the variation in silicate polymerization of the heterogenous C-S-H without considering intermixed microcrystalline portlandite in the hydrous regions [33] and unreacted $\beta\text{-C}_2\text{S}$.

4.4 Si environment of hydrated $\beta\text{-C}_2\text{S}$ for 51 days

Two distinct optical densities were observed in hydrated $\beta\text{-C}_2\text{S}$ cured at 25 °C for 51 days (Figure 4.7A). Double a_1 peaks are not observed in Figure 4.6B, and only a single a_1 peak at 1848.9-1849.1 eV occurs. The peak energy difference $\Delta a_2\text{-}a_1$ for areas 5, 6, 7, 8, 9, and B is 16.7-17.0 eV, and 15.8-16.2 eV for areas 1, 2, 3, and 4; two distinct ranges of $\Delta a_2\text{-}a_1$ were observed. Thus, the two distinct ODs indicate the existence of Ip (dark region) and Op (light region) in Figure 4.6A. Areas 5, 6, 7, 8, and 9 are Ip dominant, while the areas 1, 2, 3, and 4 are Op dominant. The energies of Si K-edge (a_1) and $\Delta a_2\text{-}a_1$ of Ip are both lower compared to those of Op, indicating a lower degree of silicate polymerization and a slightly longer Si-O bond length for Ip. The value of $\Delta a_2\text{-}a_1$ and Si K-edge energy for Op at 51 days are slightly both higher than at 17 days, suggesting that the Op polymerizes over time. The lower $\Delta a_2\text{-}a_1$ value for area 10 and area A may be explained by an impingement from adjacent grains. Similarly, contribution of cross-linking sites to the spectra was also not observed due to the abundant interlayer Ca between calcium silicate basal layers of C-S-H [20]. Thus, both Op and Ip are very likely mixtures of dimer and pentamer C-S-Hs with very limited amounts of octamer and longer chains. The values of $\Delta a_2\text{-}a_1$ for Op and Ip are higher compared to those of synthetic C-S-H with a bulk Ca/Si molar ratio of 1.4 [14], suggesting that the electron shielding from cations on Si from in hydration product C-S-H is weaker. This fact can be explained by the highly distorted Ca atom in $[\text{Ca}(\text{OH})(\text{H}_2\text{O})_5]^+$ in the interlayer of C-S-Hs; and the partial replacement of divalent Ca by monovalent K from the dopant [37]. Moreover, peak a_0 at 1847.9 eV was not observed, suggesting a fully hydrated grain (see Figure 4.8).

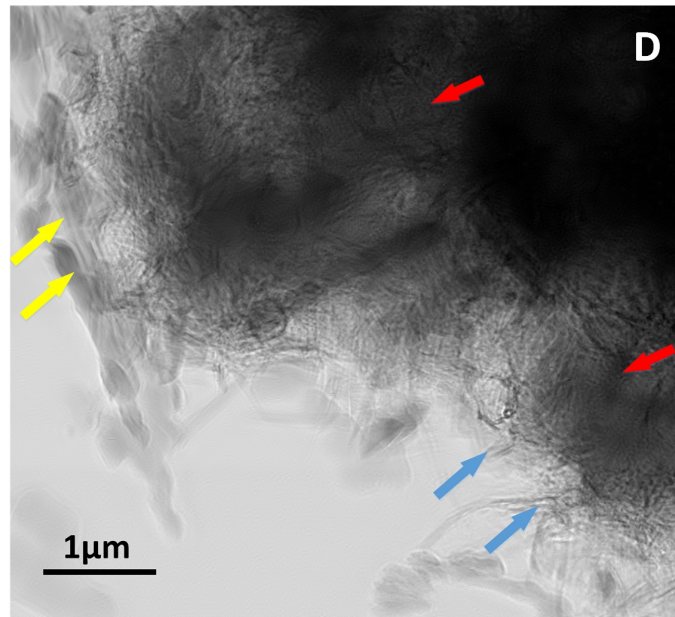
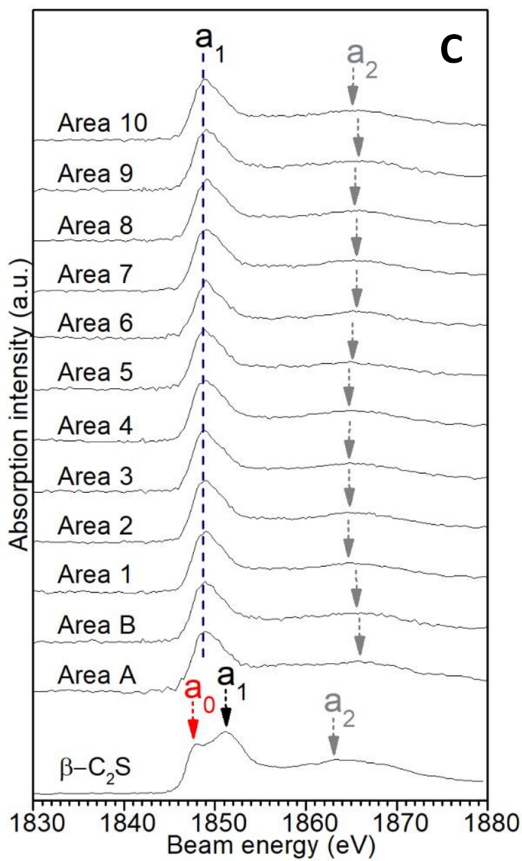
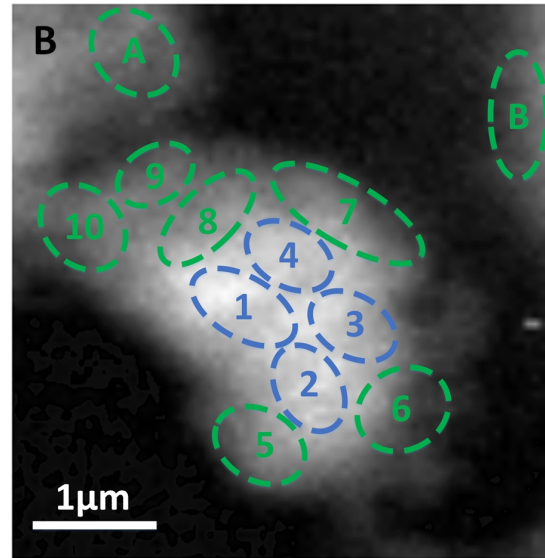
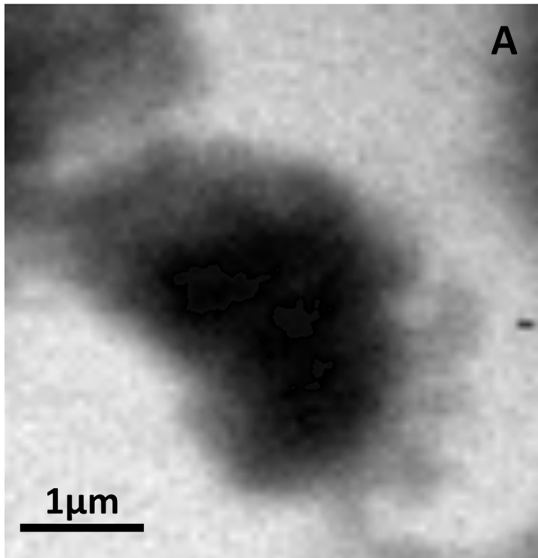


Figure 4.7 Hydrated β - C_2S cured at 25 °C for 51 days: (A) Transmission image of the ROI at 1849 eV; (B) selected areas in the Si element mapping for the XANES spectra; (C) Si K-edge XANES spectra extracted from different areas specified in (C); (D) ptychographic image of another area at the same age. Op is indicated by blue arrows, Ip is indicated by red arrows, and portlandite is indicated by yellow arrows.

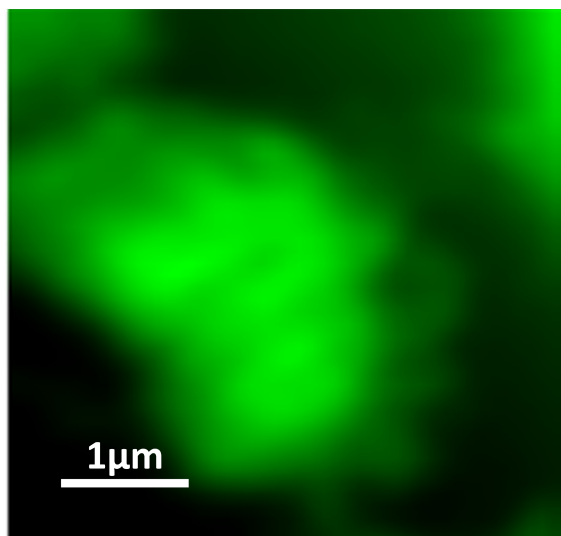


Figure 4.8 RGB overlay map of hydrated β -C₂S cured at 25 °C for 51 days in Figure 4.7 Green area is obtained based on Si K-edge XANES spectrum of C-S-H (area 2), and reference spectrum of anhydrous β -C₂S is used to obtain red area. The absence of red area suggests a fully hydrated particle.

The ptychographic image shown in Figure 4.7D presents the fibrillar Op of another hydrated β -C₂S particle at 51 days; the width of fibers presents a distribution of 11-25 nm, which is thinner than the Op of in triclinic C₃S hydration system [38]. The Ip of hydrated β -C₂S exhibits a dense aggregated structure, while the Ip of hydrated triclinic C₃S at the same water-to-solid ratio exhibits a less dense nanostructure with aggregated globules. The morphological difference between the Ips in β -C₂S and C₃S hydration systems can be explained by the lower hydraulic reactivity of β -C₂S. Geng et al. [25] reported that Ip and Op in C₃S hydration system exhibit an identical Si K-edge but with a higher energy for the a₂ peaks of Op, indicating that Ip of hydrated C₃S has a lower degree of silicate polymerization. Portlandite micro-crystallites that intermix with Op is observed, which is consistent with the transmission electron microscopy (TEM) study by Richardson [39].

4.5 Si environment of anhydrous and hydrated α' _H-C₂S for 10 days

Similar to anhydrous β -C₂S, pre-edge peak a₀ was also observed in anhydrous α' _H-C₂S as shown in Figure 4.9, suggesting a slight distortion of the silicate tetrahedron of anhydrous α' _H-C₂S. The Si K-edge energy of anhydrous α' _H-C₂S is 0.2 eV higher than that of anhydrous β -C₂S, suggesting a slightly shorter Si-O bond length of α' _H-C₂S relative to β -C₂S, which is consistent with results of Rietveld refinement of anhydrous α' _H-C₂S and β -C₂S [27].

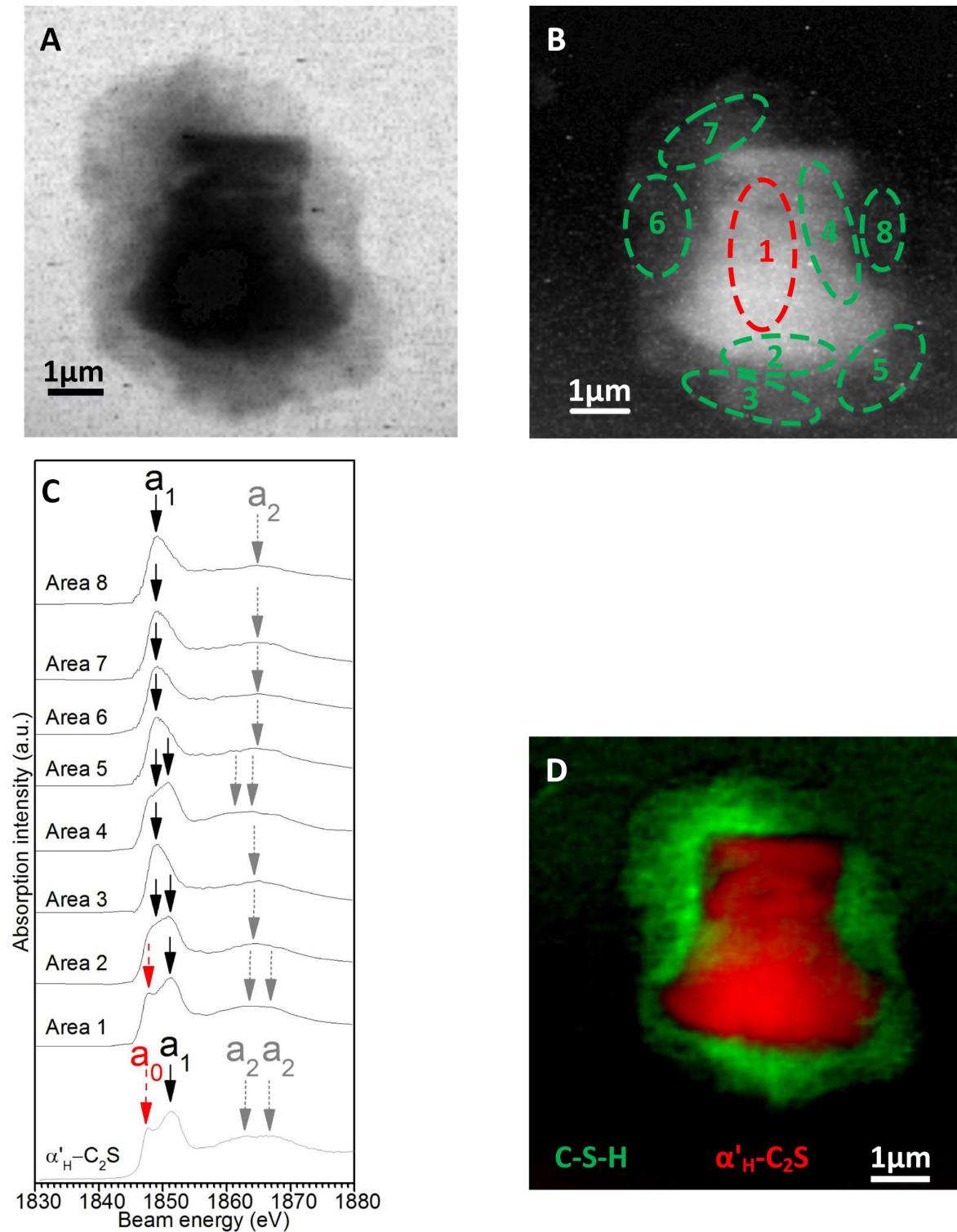


Figure 4.9 Hydrated $\alpha'_H\text{-C}_2\text{S}$ cured at 25 °C at 10 days: (A) Transmission image of the ROI taken at 1849 eV; (B) selected areas in the Si element map for the XANES spectra; (C) Si K-edge XANES spectra extracted from different areas specified in (B); (D) RGB overlay map using XANES spectra obtained from the C-S-H (area 7, green) marked in (B) and reference spectrum of anhydrous $\alpha'_H\text{-C}_2\text{S}$ (red).

Similar to β -C₂S hydration, the interface between non-fibrillar Op and α' _H-C₂S was observed at 10 days with this spatial resolution (~60 nm). The Si K-edge and Δa_2-a_1 of hydrated α' _H-C₂S at 10 days are equivalent to or 0.2-0.3 eV higher than those in hydrated β -C₂S at 17 days. Thus, the chemical environment of Si in hydrated α' _H-C₂S is similar to that in β -C₂S hydration at 17 days with a comparable degree of silicate polymerization but at an earlier age. The polymerization degree of the Op is more homogeneous since the Δa_2-a_1 values of all C-S-Hs here are ~15.9 eV. Again, cross-linking sites are not present in Op area, suggesting that the Op is still mainly a mixture of dimer and pentamer units [40]. Thus, α' _H-C₂S exhibits a higher hydraulic reactivity relative to β -C₂S. This work is consistent with experimental and simulation studies on the reactivity [4] [41] [42] but provides new details on the rate of silicate polymerization of α' _H-C₂S hydration.

4.6 Si environment of hydrated α' _H-C₂S for 40 days

The C-S-H of α' _H-C₂S curd at 25 °C for 40 days is fibrillar, as shown in Figure 4.10. There is no interface between its Ip and Op in the fully hydrated particle (see Figure 4.11) observed. The values of Δa_2-a_1 for all the areas range from 16.7 to 17.0 eV, suggesting a relatively uniform degree of silicate polymerization. This is a primary difference compared to the Si environment in β -C₂S hydration system. The Si K-edge (a_1) of all areas is comparable, suggesting similar Si coordination in these areas. The comparable degree of silicate polymerization of the interfaces between different particles suggests that the silicate polymerization of C-S-H is not obviously impinged by the adjacent particles. Additionally, the C-S-Hs of hydrated α' _H-C₂S at 40 days are mainly mixtures of dimer and pentamer units, and a cross-linking effect was not observed in the spectra. Compared to the Op of hydrated β -C₂S at 51 days, hydrated α' _H-C₂S at 40 days exhibited a comparable degree of silicate polymerization but at an earlier age. This confirms the higher hydraulic reactivity of α' _H-C₂S compared with β -C₂S.

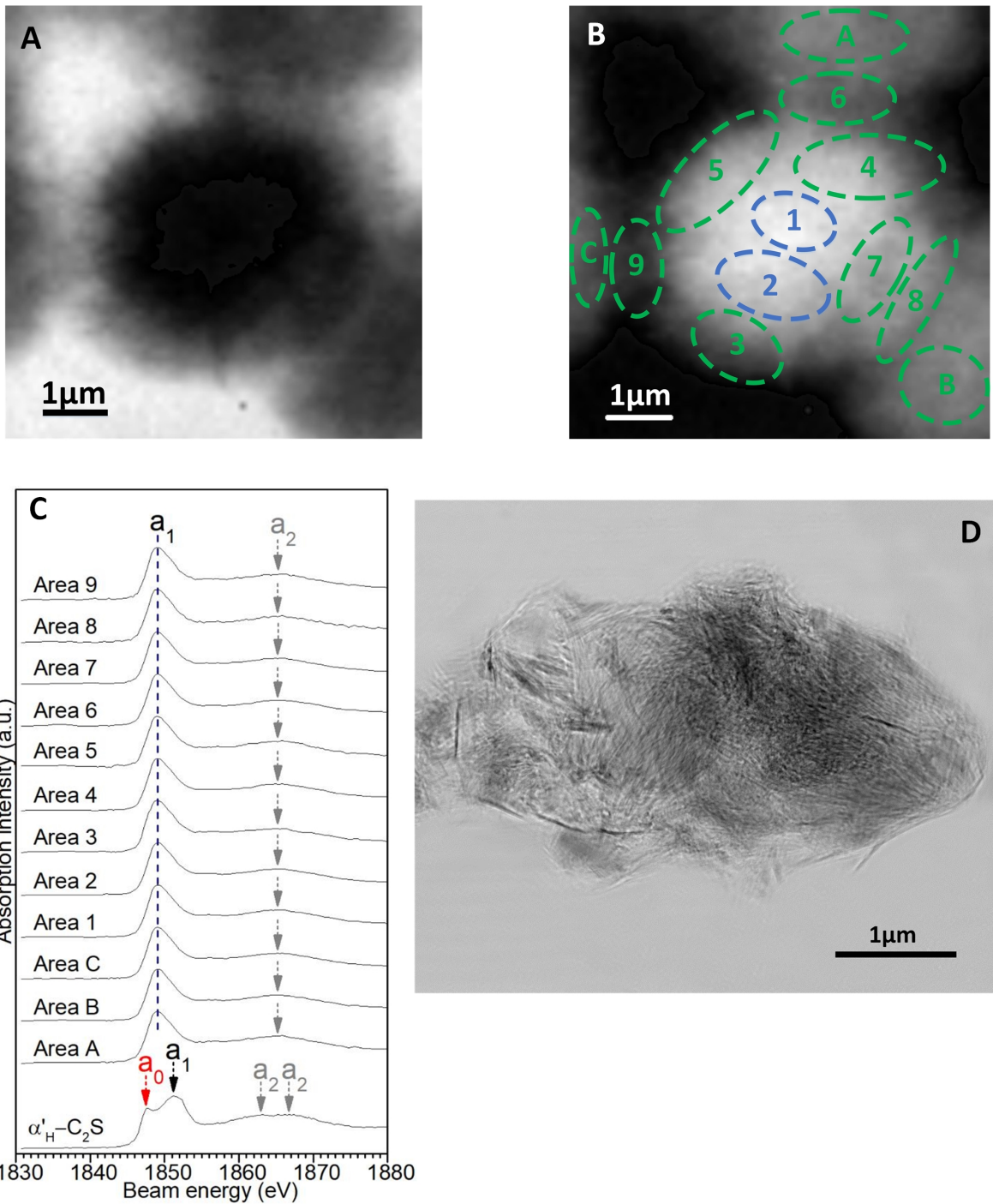


Figure 4.10 Hydrated $\alpha'_H\text{-C}_2\text{S}$ cured at 25 °C for 40 days: (A) Transmission image of the ROI taken at 1849 eV; (B) selected areas in the Si element map for the XANES spectra; (C) Si K-edge XANES spectra extracted from different areas specified in (B); (D) ptychographic image taken at 800 eV.

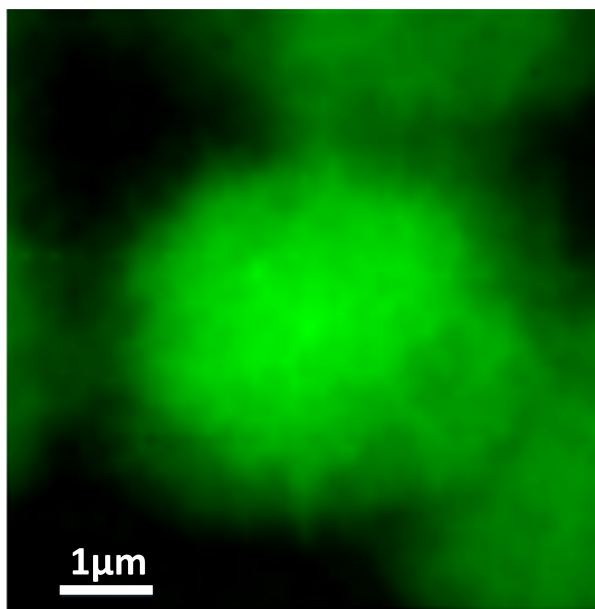


Figure 4.11 RGB overlay map of hydrated $\alpha'_{\text{H}}\text{-C}_2\text{S}$ cured at 25 °C for 40 days in Figure 4.10. Green area is obtained based on Si K-edge XANES spectrum of C-S-H (area 1). The absence of signal of anhydrous $\alpha'_{\text{H}}\text{-C}_2\text{S}$ (e.g., the red area in Figure 4.9D) suggests a fully hydrated particle here.

The ptychographic image (Figure 4.10D) shows the fibrillar C-S-H with a width range of 15-30 nm, which is greater than hydrated $\beta\text{-C}_2\text{S}$ but smaller than hydrated C_3S (41-59 nm) [38], and the inner C-S-H exhibits a looser aggregated microstructure with ~ 17 nm voids compared to the Ip of hydrated $\beta\text{-C}_2\text{S}$. The Ips of hydrated $\beta\text{-C}_2\text{S}$, hydrated C_3S , and hydrated PC with a practical water-to-solid ratio (i.e., <0.6) appear to be small and globular [19]. The larger void of the Ip relative to the Ip of hydrated C_3S [19] at w/s below 0.5 could be induced by the extremely high water-to-solid ratio (10 used in this study), which provides sufficient space for the growth of nanocrystallite during the fast hydration and the differential reactivity from the crystal faces of $\alpha'_{\text{H}}\text{-C}_2\text{S}$. The microstructure of hydrated $\alpha'_{\text{H}}\text{-C}_2\text{S}$ is similar to hydrated C_3S with the same w/s [38] instead of the hydrated $\beta\text{-C}_2\text{S}$ mentioned above. Thus, the morphological difference among the silicates in these diluted systems may be relevant to their hydraulic reactivity. More ptychographic images can be found in Appendix.

4.7 Conclusions

STXM can successfully probe the variation in local degree of silicate polymerization and Ca environment down to a 25 nm scale. Coupling with ptychographic imaging technique, the nano morphological features can be characterized. Ca environment in both anhydrous $\beta\text{-C}_2\text{S}$ and $\alpha'_{\text{H}}\text{-C}_2\text{S}$ are in a distorted cubic symmetric coordination. The Ca coordination of C-S-H in both hydration systems is also highly distorted but octahedral-like. The Ca environment of C-S-H in both hydration systems is similar to 14Å tobermorite but have a shorter-range of ordering. More six-fold coordinated Ca occur in hydrated $\alpha'_{\text{H}}\text{-C}_2\text{S}$ than in hydrated $\beta\text{-C}_2\text{S}$. The Si of both anhydrous phases have distorted tetrahedral coordination. The silicate chain of the Op in both hydration systems polymerizes over time. The C-S-H in the $\alpha'_{\text{H}}\text{-C}_2\text{S}$ hydration system

polymerizes faster than in β -C₂S. The hydraulic reactivity of anhydrous α' _H-C₂S is higher relative to that of β -C₂S.

Ip has a lower degree of silicate polymerization than Op in fully hydrated β -C₂S, which is accompanied with a slightly longer Si-O bond length due to the space constraint for further hydration. Compared to hydrated β -C₂S, the degree of silicate polymerization in hydrated α' _H-C₂S is more uniform.

The C-S-H of hydrated β -C₂S exhibits fine fibrils that intermix with portlandite, and Ip appears to be a dense aggregated microstructure. The morphology of fully hydrated α' _H-C₂S is more uniform, and its inner region is slightly more porous with nano-size voids. Ip and Op are not distinguished in fully hydrated α' _H-C₂S

The study of hydration of two C₂S polymorphs provides insights into advanced applications of the C₂S rich cements and the controllability of the performance of these materials in service. The lower calcination temperature and CO₂ emission of α' _H-C₂S during manufacturing can reduce the environmental impact of cement manufacturing. Due to its high hydraulic reactivity, α' _H-C₂S can be a practical alternative to C₃S and β -C₂S in Portland cement or BYF cement. Therefore, this work is an important step towards the development of hydration mechanism of C₂S-rich cement, which will provide new insight into the performance of these sustainable cements (lower CO₂ emission and energy use) in service. For instance, the degree of silicate polymerization of C-S-H seems to correlate the vulnerability of carbonation of C-S-H [43] [44]. The decomposition rate of C-S-H under carbonation increases with increasing degree of silicate polymerization. Understanding the differential degree of silicate polymerization of C-S-H in different C₂S hydration systems may help to design C₂S-based cementitious materials with a higher resistance to carbonation.

4.8 References

1. Manzano, H., J.S. Dolado and A. Ayuela, Elastic properties of the main species present in Portland cement pastes. *Acta Materialia*, 2009. **57**(5): p. 1666-1674.
2. Gartner, E., Industrially interesting approaches to "low-CO₂" cements. *Cement and Concrete Research*, 2004. **34**(9): p. 1489-1498.
3. Lee, B.Y. and K.E. Kurtis, Proposed acceleratory effect of TiO₂ nanoparticles on Belite hydration: preliminary results. *Journal of the American Ceramic Society*, 2012. **95**(1): p. 365-368.
4. Cuesta, A., E.R. Losilla, M.A. Aranda, J. Sanz and G. Ángeles, Reactive belite stabilization mechanisms by boron-bearing dopants. *Cement and Concrete Research*, 2012. **42**(4): p. 598-606.
5. Jelenic, I. and A. Bezjak, On the hydration kinetics of alpha-'-modifications and beta-modifications of dicalcium silicate. *Cement and Concrete Research*, 1981. **11**(3): p. 467-471.
6. Ishida, H., Y. Okada and T. Mitsuda, Highly reactive β -dicalcium silicate: II, Hydration behavior at 25° C followed by 29Si nuclear magnetic resonance. *Journal of the American Ceramic Society*, 1992. **75**(2): p. 359-363.

7. Geng, G., R.J. Myers, A.L. Kilcoyne, J. Ha and P.J. Monteiro, Ca L₂, 3-edge near edge X-ray absorption fine structure of tricalcium aluminate, gypsum, and calcium (sulfo) aluminate hydrates. *American Mineralogist*, 2017. **102**(4): p. 900-908.
8. Naftel, S.J., T.K. Sham, Y.M. Yiu and B.W. Yates, Calcium L-edge XANES study of some calcium compounds. *Journal of Synchrotron Radiation*, 2001. **8**: p. 255-257.
9. Fleet, M.E. and X.Y. Liu, Calcium L₂,L₃-edge XANES of carbonates, carbonate apatite, and oldhamite (CaS). *American Mineralogist*, 2009. **94**(8-9): p. 1235-1241.
10. Ko, J.P., X-ray Absorption Near-edge Structure (XANES) of calcium L₂, L₃ edges of various calcium compounds and X-ray Excited Optical Luminescence (XEOL) studies of luminescent calcium compounds. *X-Ray Absorption Fine Structure--XAFS*, 2007. **13**(882): p. 538-540.
11. Geng, G., J. Li, Y.-S. Yu, D.A. Shapiro, D.A. Kilcoyne and P.J. Monteiro, Nanometer-resolved spectroscopic study reveals the conversion mechanism of CaO· Al₂O₃· 10H₂O to 2CaO· Al₂O₃· 8H₂O and 3CaO· Al₂O₃· 6H₂O at an elevated temperature. *Crystal Growth & Design*, 2017. **17**(8): p. 4246-4253.
12. Jost, K.H., et al., Redetermination of the structure of beta-dicalcium silicate. *Acta Crystallographica Section B: Structural Crystallography and Crystal Chemistry*, 1977. **33**(6): p. 1696-1700.
13. Bonaccorsi, E., S. Merlino and A.R. Kampf, The crystal structure of tobermorite 14 Å (Plombierite), a C-S-H phase. *Journal of the American Ceramic Society*, 2005. **88**(3): p. 505-512.
14. Li, J., G. Geng, R.J. Myers and Y.-S.S. Yu, David A; Carraro, Carlo; Maboudian, Roya; Monteiro, Paulo J.M. , The chemistry and structure of calcium (alumino) silicate hydrate: A study by XANES, ptychographic imaging, and wide- and small- angle scattering. *Cement and Concrete Research*, 2019.
15. Skinner, L.B., S.R. Chae, C.J. Benmore, H.R. Wenk and P.J.M. Monteiro, Nanostructure of calcium silicate hydrates in cements. *Physical Review Letters*, 2010. **104**(19).
16. Bae, S., R. Taylor, D. Hernandez-Cruz, S. Yoon, D. Kilcoyne and P.J.M. Monteiro, Soft X-ray spectromicroscopic investigation of synthetic C-S-H and C₃S hydration products. *Journal of the American Ceramic Society*, 2015. **98**(9): p. 2914-2920.
17. Kirkpatrick, R.J., G.E. Brown, N. Xu and X.D. Cong, Ca X-ray absorption spectroscopy of C-S-H and some model compounds. *Advances in Cement Research*, 1997. **9**(33): p. 31-36.
18. Cong, X. and R.J. Kirkpatrick, ¹⁷O and ²⁹Si MAS NMR study of β-C₂S hydration and the structure of calcium-silicate hydrates. *Cement and concrete research*, 1993. **23**(5): p. 1065-1077.
19. Richardson, I.G., The calcium silicate hydrates. *Cement and Concrete Research*, 2008. **38**(2): p. 137-158.
20. Gartner, E., I. Maruyama and J. Chen, A new model for the CSH phase formed during the hydration of Portland cements. *Cement and Concrete Research*, 2017. **97**: p. 95-106.
21. Li, D., G.M. Bancroft, M.E. Fleet and X.H. Feng, Silicon K-Edge XANES spectra of silicate minerals. *Physics and Chemistry of Minerals*, 1995. **22**(2): p. 115-122.
22. Fleet, M.E., S. Muthupari, M. Kasrai and S. Prabakar, Sixfold coordinated Si in alkali and alkali-CaO silicophosphate glasses by Si K-edge XANES spectroscopy. *Journal of Non-Crystalline Solids*, 1997. **220**(1): p. 85-92.

23. Li, D., G.M. Bancroft, M. Kasrai, M.E. Fleet, R.A. Secco, X.H. Feng, K.H. Tan and B.X. Yang, X-ray absorption spectroscopy of silicon dioxide (SiO₂) polymorphs - the structural characterization of opal. *American Mineralogist*, 1994. **79**(7-8): p. 622-632.
24. Cabaret, D., M. Le Grand, A. Ramos, A.M. Flank, S. Rossano, L. Galois, G. Calas and D. Ghaleb, Medium range structure of borosilicate glasses from Si K-edge XANES: a combined approach based on multiple scattering and molecular dynamics calculations. *Journal of Non-Crystalline Solids*, 2001. **289**(1-3): p. 1-8.
25. Geng, G., R. Taylor, S. Bae, D. Hernandez-Cruz, D.A. Kilcoyne, A.H. Emwas and P.J.M. Monteiro, Atomic and nano-scale characterization of a 50-year-old hydrated C3S paste. *Cement and Concrete Research*, 2015. **77**: p. 36-46.
26. Li, Q.G., Y.; Geng, G.; Bae, S.; Monteiro, P. J. M.; CaCl₂-accelerated hydration of tricalcium silicate: A STXM study combined with ²⁹Si MAS NMR. *Journal of Nanomaterials*, 2015. **2015**: p. 1-10.
27. Mumme, W., R. Hill, G. Bushnell-Wye and E. Segnit, Rietveld crystal structure refinements, crystal chemistry and calculated powder diffraction data for the polymorphs of dicalcium silicate and related phases. 1995.
28. Soyer-Uzun, S., S.R. Chae, C.J. Benmore, H.R. Wenk and P.J.M. Monteiro, Compositional evolution of calcium silicate hydrate (C-S-H) structures by total x-ray scattering. *Journal of the American Ceramic Society*, 2012. **95**(2): p. 793-798.
29. Calas, G., G.E. Brown, G.A. Waychunas and J. Petiau, X-ray absorption spectroscopic studies of silicate-glasses and minerals. *Physics and Chemistry of Minerals*, 1987. **15**(1): p. 19-29.
30. Nicoleau, L. and M.A. Bertolim, Analytical model for the alite (C3S) dissolution topography. *Journal of the American Ceramic Society*, 2016. **99**(3): p. 773-786.
31. Durgun, E., H. Manzano, R.J.M. Pellenq and J.C. Grossman, Understanding and controlling the reactivity of the calcium silicate phases from first principles. *Chemistry of Materials*, 2012. **24**(7): p. 1262-1267.
32. Henderson, G.S., A Si K-edge EXAFS/XANES study of sodium-silicate glasses. *Journal of Non-Crystalline Solids*, 1995. **183**(1-2): p. 43-50.
33. Richardson, I.G., Tobermorite/jennite- and tobermorite/calcium hydroxide-based models for the structure of C-S-H: applicability to hardened pastes of tricalcium silicate, beta-dicalcium silicate, Portland cement, and blends of Portland cement with blast-furnace slag, metakaolin, or silica fume. *Cement and Concrete Research*, 2004. **34**(9): p. 1733-1777.
34. Yu, P., R.J. Kirkpatrick, B. Poe, P.F. McMillan and X.D. Cong, Structure of calcium silicate hydrate (C-S-H): Near-, mid-, and far-infrared spectroscopy. *Journal of the American Ceramic Society*, 1999. **82**(3): p. 742-748.
35. Cong, X.D. and R.J. Kirkpatrick, Si-29 MAS NMR study of the structure of calcium silicate hydrate. *Advanced Cement Based Materials*, 1996. **3**(3-4): p. 144-156.
36. Richardson, I.G. and G.W. Groves, Microstructure and microanalysis of hardened ordinary Portland-cement pastes. *Journal of Materials Science*, 1993. **28**(1): p. 265-277.
37. L'Hôpital, E., B. Lothenbach, K. Scrivener and D. Kulik, Alkali uptake in calcium alumina silicate hydrate (CASH). *Cement and Concrete Research*, 2016. **85**: p. 122-136.
38. Bae, S., R. Taylor, D. Shapiro, P. Denes, J. Joseph, R. Celestre, S. Marchesini, H. Padmore, T. Tyliczszak and T. Warwick, Soft X-ray ptychographic imaging and

- morphological quantification of calcium silicate hydrates (C–S–H). *Journal of the American Ceramic Society*, 2015. **98**(12): p. 4090-4095.
39. Richardson, I.G., The nature of C-S-H in hardened cements. *Cement and Concrete Research*, 1999. **29**(8): p. 1131-1147.
 40. Richardson, I.G., The nature of the hydration products in hardened cement pastes. *Cement & Concrete Composites*, 2000. **22**(2): p. 97-113.
 41. Müller, R., J. Neubauer and F. Götz–Neunhoeffler, Effects of phosphate rich raw materials on the crystallographic and hydraulic properties of dicalcium silicate. *Proceedings of the 11th Int. Cong. On the Chem. of Cement, Durban, South Africa*, 2003: p. 1045-1053.
 42. Ludwig, H.-M. and W. Zhang, Research review of cement clinker chemistry. *Cement and Concrete Research*, 2015. **78**: p. 24-37.
 43. Li, J., Yu, Q., Huang, H. and Yin, S., Effects of Ca/Si ratio, aluminum and magnesium on the carbonation behavior of calcium silicate hydrate. *Materials*, 2019, 12(8), p.1268.
 44. Sevelsted, T. F., and Skibsted, J. Carbonation of C–S–H and C–A–S–H samples studied by ^{13}C , ^{27}Al and ^{29}Si MAS NMR spectroscopy. *Cement and concrete research*, 2015, 71, 56-65.

5. Chemistry and structure of calcium (alumino) silicate hydrate

The use of supplementary cementitious materials (SCMs), e.g., fly ash, ground granulated blast-furnace slag, silica fume, and calcined clay, is a well-established approach to enhancing the physical and mechanical properties of PC-based concrete and reducing the environmental impacts of concrete production. Many commonly used SCMs, including as fly ash, ground granulated blast-furnace slag, and metakaolin, are Al-bearing. The incorporation of Al promotes the formation of higher polymerization degree of the aluminosilicate chain of calcium (alumino)silicate hydrate (C-(A-)S-H), however the influence of aluminum incorporation on the atomic and nano structures of C-(A-)S-H has not been solved. For instance, the nature of a mystery phase containing six-fold coordinated Al, which is termed third aluminate hydrate (TAH), has not been well understood. In this chapter, the atomic and nano structures of C-(A-)S-H are studied using scanning transmission X-ray microscopy and X-ray ptychographic imaging. The influence of Ca-to-Si ratio, Al-to-Si ratio, and equilibrium temperature on the structures of C-(A-)S-H are unveiled.

5.1 Ca coordination of calcium (alumino) silicate hydrate

Ca/Si* = 0.6-1.6, Al/Si* = 0, and equilibrium at 20 °C

The XANES spectra of the C-(A-)S-H samples at Ca L_{2,3}-edge are shown in Figures 5.1 and 5.2. The XANES spectra resemble typical L_{2,3}-edge spectra of d⁰ compounds, e.g., Ca²⁺ and K⁺. Again, they correspond to the electronic excitation of Ca atoms from 2p⁶3d⁰ to 2p⁵3d¹ orbitals. Due to the loss of degeneracy of 2p orbitals by spin-orbit coupling, two major peaks are observed, L₃ (2p_{3/2}, a₂ peak) and L₂ (2p_{1/2}, b₂ peak) [1] [2] [3]. Minor peaks (a₁ and b₁) exist to the left of each major peak, which originate from crystal field splitting. These peaks are clearly observed when the coordination configuration is of a certain symmetry, e.g., octahedral or cubic. The energy separations (splitting energies, $\Delta L_3 = a_2 - a_1$ and $\Delta L_2 = b_2 - b_1$) in two doublets between the adjacent major and minor peaks relate to the strength of the crystal field effects, which depend on the ligand type and distortion of the symmetry [2]. A small leading peak a₀ originates from the mixing of states due to multipole interactions of core holes with valence electrons, combined with 3d spin-orbit splitting effects [3].

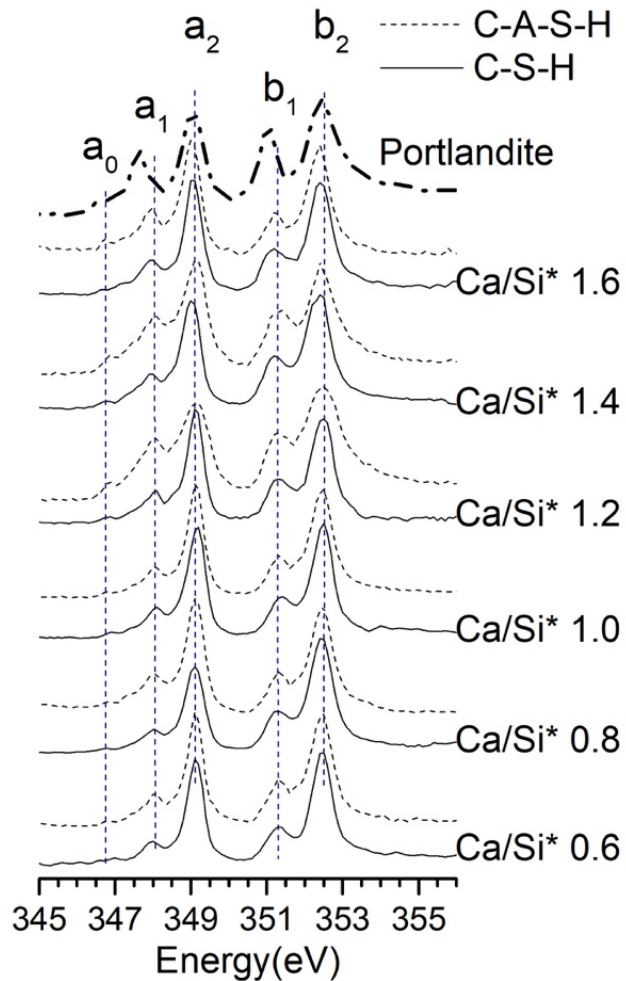


Figure 5.1. Ca L_{2,3}-edge XANES spectra of synthetic C-S-H (solid lines) and C-A-S-H products with Al/Si* = 0.05 (dashed lines) after 182 days of equilibrium at 20 °C. Ca/Si* = bulk Ca/Si ratio, Al/Si* = bulk Al/Si ratio

The spectra indicate that Ca possesses an octahedral-like coordination symmetry in all samples. However, this symmetry of these Ca is clearly distorted since the a₁ and b₁ peaks are not as intense and sharp as those in the XANES spectra of portlandite, where Ca is in an ideal octahedral coordination symmetry. The pre-edge peak a₀ is less resolvable in C-S-H samples than in C-A-S-H samples due to the poorer ordering of C-S-H. The Ca in the studied samples are not cubic-coordinated, otherwise an extra minor peak would be observed between a₁ and a₂ peaks (katoite-like) [4].

For samples with Ca/Si* ranging from 0.6 to 1.4, the splitting energies of C-S-H are consistently near 1.1 eV (see Table 5.1), suggesting that most Ca in C-S-H are in similar coordination symmetry. The low peak intensity ratios between minor and major peaks suggest that there is no tendency to form a well-crystallized phase as Ca/Si increases [5] [1] [6] [7]. In addition, a strong splitting is not observed in C-S-H with Ca/Si* = 1.6 when the scanned step is refined to ~20 nm. The absence of strong splitting suggests that the small amount of portlandite in bulk X-ray

diffraction (XRD) results [8] forms as distinct (micro)crystallites, and does not regularly intermix with C-(A-)S-H at the length scale of 20 nm. This interpretation is consistent with the previous assignment of a Ca/Si ratio of 1.38 to this C-S-H phase in this sample, with the remaining Ca in this sample assigned to a distinct portlandite phase (Ca/Si* = 1.6) [9]. The results are also consistent with the interpretation that the Ca/Si* = 1.6 sample is not fully equilibrated [10], because at this composition and at equilibrium phase pure C-S-H is stable. Therefore, the Ca L_{2,3}-edge spectra are fully explained by a defective tobermorite-based model [11], i.e., the low splitting energy at Ca L_{2,3}-edge originates mainly from the seven-fold coordinated Ca-O sheet in the calcium silicate basal layer of C-S-H, and has minor contribution from the octahedral coordinated zeolitic Ca ([Ca(H₂O)₆]²⁺ and/or [Ca(OH)(H₂O)₅]⁺ that is charge-balanced in the interlayer. As Ca/Si increases, there is no increasing trend of the peak intensity ratios between minor and major peaks, suggesting that the increased amount of the interlayer Ca is six-fold coordinated in a highly distorted octahedral symmetry, which is consistent with the present interpretation. The interlayer [Ca(H₂O)₆]²⁺ at Ca/Si ≤ 1.5 and [Ca(OH)(H₂O)₅]⁺ at Ca/Si* = 1.6 suggested by Gartner et al. [12] are both with highly distorted octahedral symmetry, which is again consistent with the present interpretation. Furthermore, a pair distribution function work reported that the interlayer Ca in C-S-H with high Ca/Si ratios (>1.2) is more likely octahedrally coordinated [13].

The major peak positions (a₂ and b₂) in the XANES spectra for C-S-H with Ca/Si* = 0.6-1.2 are generally equivalent, suggesting a comparable oxidation degree of Ca and a similar average coordination number of Ca-O in C-S-H at low Ca/Si*. For Ca/Si* of 1.4 and 1.6, the major peak positions are 0.05-0.1 eV lower than those at Ca/Si* ≤ 1.2, suggesting that more six-fold coordinated zeolitic Ca species are charge-balanced in the interlayer or on the surface of C-S-H in this higher Ca/Si* range. The occurrence of seven- and/or six-fold Ca sites in C-S-H(I) is in good agreement with 11Å- and 14Å-tobermorite, the Ca-O coordination numbers of which are mostly six or seven [14] [15] [12]. The reported X-ray photoelectron spectroscopy experiments exhibit similar results, namely, a Ca 2p_{3/2} binding energy of C-S-H [16] that is independent of the bulk Ca/Si ratio.

Table 5.1. Absorption features in the XANES spectra of C-(A-)S-H samples at Ca L_{2,3}-edge. The estimated absolute errors are ± 0.01 eV in energy positions and ± 0.0002 units in intensity ratios.

Al/Si*	Ca/Si*	Energy (eV)								
		a ₀	a ₁	a ₂	a ₁ /a ₂	ΔL ₃	b ₁	b ₂	b ₁ /b ₂	ΔL ₂
Equilibrium at 20 °C										
0	0.6	347	348.0	349.1	0.0648	1.1	351.4	352.5	0.0944	1.1
	0.8	346.8	348.0	349.1	0.0618	1.1	351.35	352.45	0.0647	1.1
	1.0	348.8	348.0	349.1	0.0495	1.1	351.4	352.5	0.0756	1.1
	1.2	346.8	348.05	349.1	0.089	1.05	351.4	352.5	0.089	1.1
	1.4	346.8	347.95	349.0	0.0695	1.05	351.3	352.4	0.0935	1.1
	1.6	346.8	347.95	349.05	0.0842	1.1	351.25	352.4	0.1015	1.15
0.05	0.6	346.7	348.0	349.1	0.0992	1.1	351.4	352.5	0.1278	1.1
	0.8	346.8	348.0	349.1	0.0794	1.1	351.4	352.5	0.1382	1.1
	1.0	346.8	348.05	349.1	0.0798	1.05	351.45	352.5	0.1334	1.05
	1.2	346.8	348.0	349.1	0.144	1.1	351.4	352.5	0.1159	1.1
	1.4	346.8	348.0	349.1	0.0902	1.1	351.35	352.45	0.1501	1.1
	1.6	346.8	348.05	349.1	0.155	1.05	351.35	352.45	0.1482	1.1
Equilibrium at 7 °C										
0	1.0	347*	348.0*	349.1	-	1.1	351.4	352.5	0.017	1.1
0.05	1.0	347*	348.0*	349.1	0.0134	1.1	351.4	352.5	0.053	1.1
0.1	1.0	346.8*	348.0*	349.1	0.0433	1.1	351.4	352.5	0.0856	1.1
Equilibrium at 50 °C										
0	1.0	346.8	348.0	349.1	0.0814	1.1	351.35	352.5	0.0931	1.15
0.05	1.0	346.8	348.0	349.1	0.1188	1.1	351.4	352.5	0.1581	1.1
0.1	1.0	346.8	348.0	349.1	0.1303	1.1	351.4	352.5	0.171	1.1
Equilibrium at 80 °C										
0	1.0	346.8	348.0	349.1	0.0861	1.1	351.4	352.5	0.1688	1.1
0.05	1.0	346.8	348.0	349.1	0.1458	1.1	351.4	352.5	0.2241	1.1
0.1	1.0	346.8	348.0	349.1	0.1718	1.1	351.4	352.5	0.2557	1.1

*weak peak, peak position is not clearly identified.

Ca/Si* = 0.6-1.6, Al/Si* = 0.05, and equilibrium at 20 °C

Comparable peak positions are observed in the XANES spectra Ca L_{2,3}-edge for the C-S-H and C-A-S-H samples equilibrated at 20 °C, indicating that minor Al incorporation (Al/Si* = 0.05) does not greatly modify the coordination of Ca-O complexes in their molecular structures, regardless of Ca/Si ratio. At Ca/Si* of 1.4 and 1.6, the major peaks in the C-A-S-H spectra are positioned at a slightly higher energy than in the C-S-H spectra. This effect to the higher ordering of CaO₇ is assigned to the aluminum incorporation by elongating the calcium aluminosilicate basal layers. Compared to the peak intensity ratios (a₁/a₂ and b₁/b₂) of C-S-H, the C-A-S-H XANES spectra exhibit marginally higher values, which suggests an increase in the long-range order of CaO₇ sheet due to Al incorporation. However, Al incorporation does not

modify the coordination symmetry of Ca-O complexes in C-(A-)S-H structure since its splitting energies are still comparable to C-S-H.

Figure 5.2 shows the XANES spectra Ca L_{2,3}-edge of Ca-O complexes in C-(A-)S-H and in other hydrated cement phases including ettringite(C₆A \bar{S} ₃H₃₂), monosulfoaluminate(C₄A \bar{S} H₁₂), CAH₁₀, C₂AH₈, and katoite [17]. Katoite was reported to form in the C-A-S-H products that were analyzed here by L'Hôpital et al. using bulk XRD, thermogravimetric analysis, and ²⁷Al NMR measurements [10]. Yet the absence of the additional peak (a₁₀) in this C-A-S-H phase on the sub-20 nm scale suggests that katoite does not intermix C-A-S-H on this length scale. The major peak positions (a₂ and b₂) of C-A-S-H samples are identical to C₂AH₈ and monosulfoaluminate, which both have Ca coordination numbers of seven, and the major peak positions are ~0.2 eV lower than CAH₁₀ and ettringite, which have Ca coordination numbers of eight. Therefore, the coordination number of Ca in the CaO_x sheet of C-A-S-H is assigned to seven – the average coordination number of Ca in C-A-S-H is thus slightly smaller than seven due to the existence of minor quantities of octahedral Ca in the interlayer.

The absence of the leading a₁₀ and b₁₀ peaks in the Ca L_{2,3}-edge spectra, which are the characteristic peaks of AFm phases (hydrocalumite-like structure), suggested that AFm-like phases do not exist in C-A-S-H products. Furthermore, the Ca-O(H) complexes in C-A-S-H interlayer or on its surface are in octahedral-like coordination, although highly distorted. Renaudin et al. [18] proposed that calcium hydroxide, aluminum hydroxide, and an AFm-type calcium aluminate hydrate main layer may form in the interlayer of C-A-S-H. Andersen et al. [19] proposed that phases with octahedral coordinated Al may precipitate on C-A-S-H surfaces or as separate phases. The type of Ca found in AFm-type calcium aluminate hydrates is not identified in our Ca L_{2,3}-edge spectra on the sub-20nm scale, indicating that TAH is either not Ca-bearing or its Ca coordination environment is structurally analogous to the Ca in C-(A-)S-H (mainly seven-fold coordinated).

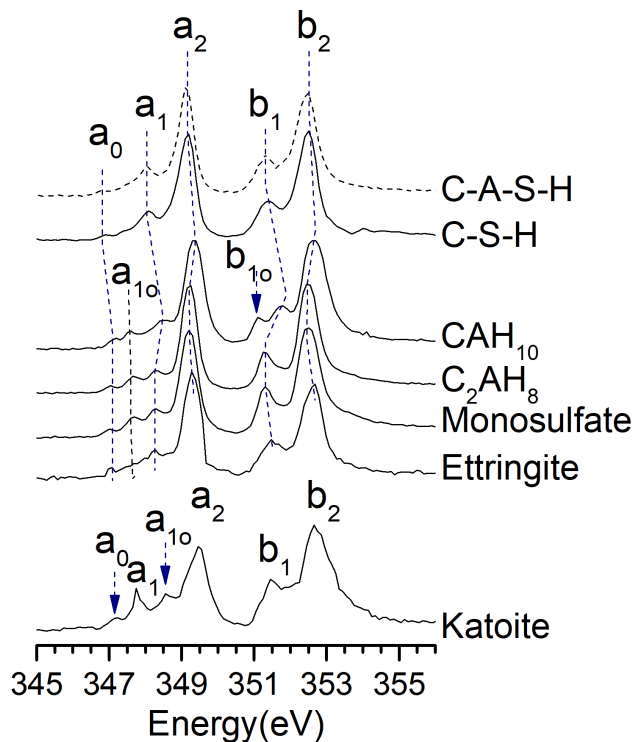


Figure 5.2. Ca $L_{2,3}$ -edge XANES spectra of C-S-H (solid lines, $\text{Ca/Si}^* = 1.0$) and C-A-S-H (dashed lines, $\text{Ca/Si}^* = 1.0$, $\text{Al/Si}^* = 0.05$) after 182 days of hydration at 20 °C. Spectra of CAH_{10} , C_2AH_8 , monosulfoaluminate (monosulfate, $\text{C}_4\text{A}\bar{\text{S}}\text{H}_{12}$), ettringite ($\text{C}_6\text{A}\bar{\text{S}}_3\text{H}_{32}$) and katoite (C_3AH_6) are taken from [23]. $\text{Ca/Si}^* = \text{bulk Ca/Si}$.

Ca/Si* = 1, Al/Si* = 0-0.1, and equilibrium at 7-80 °C

The peak positions in the Ca $L_{2,3}$ -edge XANES spectra (shown in Figure 5.3 and Table 5.1) for the C-(A-)S-H products equilibrated at temperature ranging from 7 °C to 80 °C are found to be similar. Therefore, the coordination numbers of Ca-O complexes in these products are independent of equilibration temperature in this range. The coordination symmetry of $[\text{Ca}(\text{H}_2\text{O})_6]^{2+}$ and/or $[\text{Ca}(\text{OH})(\text{H}_2\text{O})_5]^+$ in the interlayer of C-(A-)S-H is also clearly distorted regardless of the equilibration temperature. The marginal increase in the relative intensity of the minor to major peaks (a_1/a_2 and b_1/b_2) with an increased equilibration temperature is observed in this range of equilibrium temperature and is attributed to an increased long-range order of CaO_7 sheets in the C-(A-)S-H structure; the increment of relative peak intensity is more pronounced at 80 °C, indicating an increased structural ordering in this product at 80 °C. This result is consistent with existing literature [8], where the degree of stacking of calcium silicate basal layers in the c-direction of C-(A-)S-H at 80 °C was observed to significantly increase. At each equilibration temperature, the relative intensity ratio of minor to major peaks slightly increases as Al incorporation increases, which suggests that CaO_7 sheets in C-A-S-H are more long range ordered than those in C-S-H. This effect is attributed to the more polymerized aluminosilicate chains in the C-A-S-H samples.

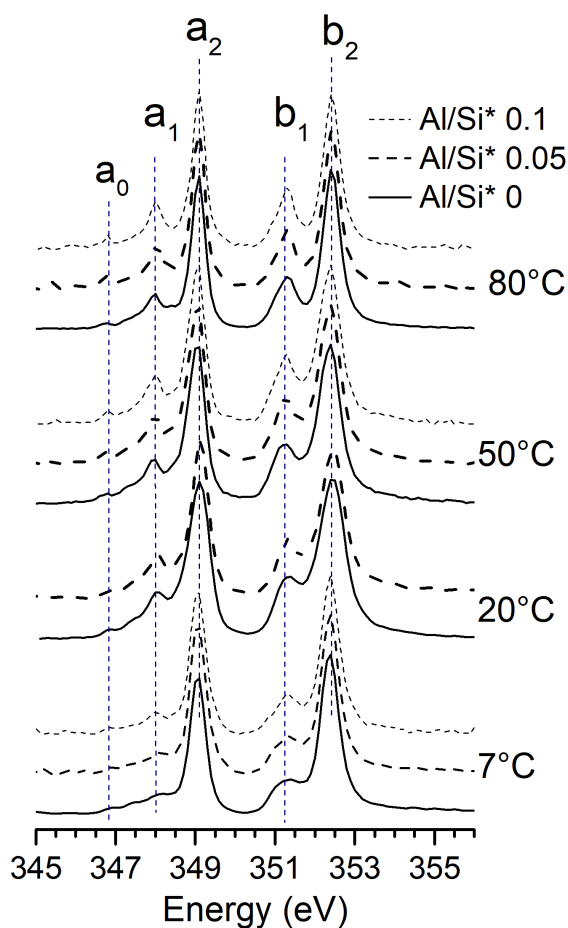


Figure 5.3. Ca $L_{2,3}$ -edge XANES spectra of C-S-H (solid lines, $Al/Si^* = 0$, $Ca/Si^* = 1.0$), C-A-S-H (long-dashed lines, $Al/Si^* = 0.05$, $Ca/Si^* = 1.0$), and C-A-S-H (short-dashed lines, $Al/Si^* = 0.1$, $Ca/Si^* = 1.0$) at different equilibration temperatures. $Ca/Si^* = \text{bulk } Ca/Si$. $Al/Si^* = \text{bulk } Al/Si$.

5.2 Chemical environment of Si

Ca/Si* = 0.6-1.6, Al/Si* = 0, and equilibrium at 20 °C

Figure 5.4 shows the XANES spectra at Si K-edge of C-(A-)S-H at equilibrium temperature of 20 °C. The major peak a_1 (Si K-edge) at 1848.7 – 1849.7 eV is assigned to the electronic transition from 1s to antibonding 3p-like state (t_2) in tetrahedral coordinated Si (dipole allowed) [20]. The minor peaks a_2 (at ~1860-1867 eV) and a_3 (1853 eV) are attributable to multi-scattering effect from more distant atom shells through photo-electron interaction, particularly the second coordination shell, and its energy is governed by the interatomic distance [21]. The peak positions and energy difference between a_1 and a_2 peaks are listed in Table 5.2. A pre-edge peak presenting the transition of Si 1s electrons to the antibonding 3s orbital (dipole-forbidden) is only observed in the $Ca/Si^* = 1.6$ C-S-H sample, suggesting the distortion of tetrahedral sites in its silicate chains.

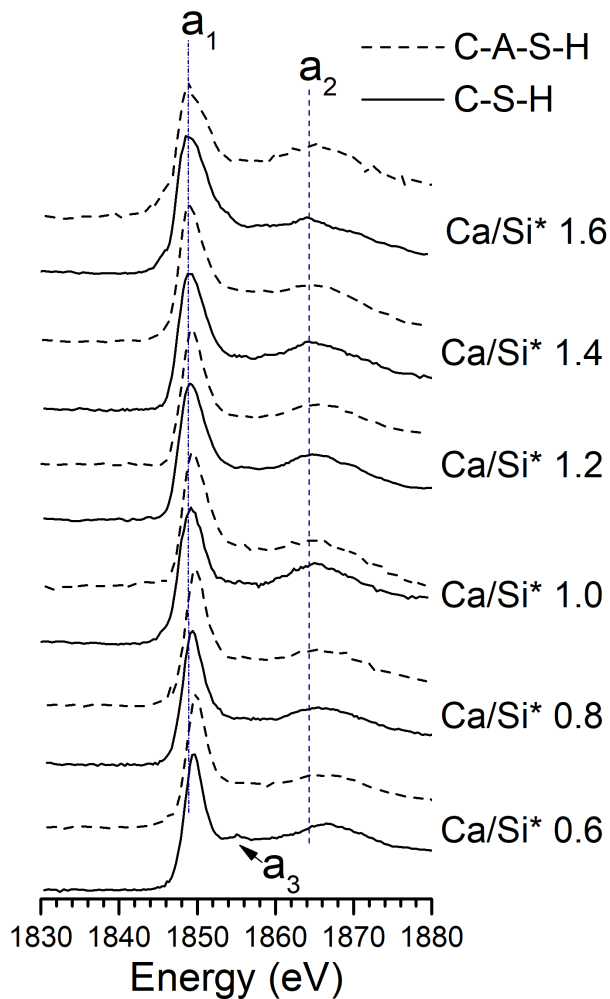


Figure 5.4. Si K-edge XANES spectra of C-S-H (solid lines) and C-A-S-H with $Al/Si^* = 0.05$ (dashed lines) after 182 days of equilibration at 20 °C. $Ca/Si^* = \text{bulk } Ca/Si$. $Al/Si^* = \text{bulk } Al/Si$. Blue lines are guides of peak shifts.

As the Ca/Si ratio increases, the Si K-edge gradually shifts to lower energy by up to 1 eV, as shown in Figure 5.5. This effect is caused by the progressive increase in the electron shielding from more Ca and a reduction in the effective Si-O bond strength. The positive correlation between the location of the Si K-edge and the degree of silicate polymerization (i.e., mean chain length of silicate chains, MCL) in the C-S-H samples is consistent with previous studies of silicate minerals [20] [21].

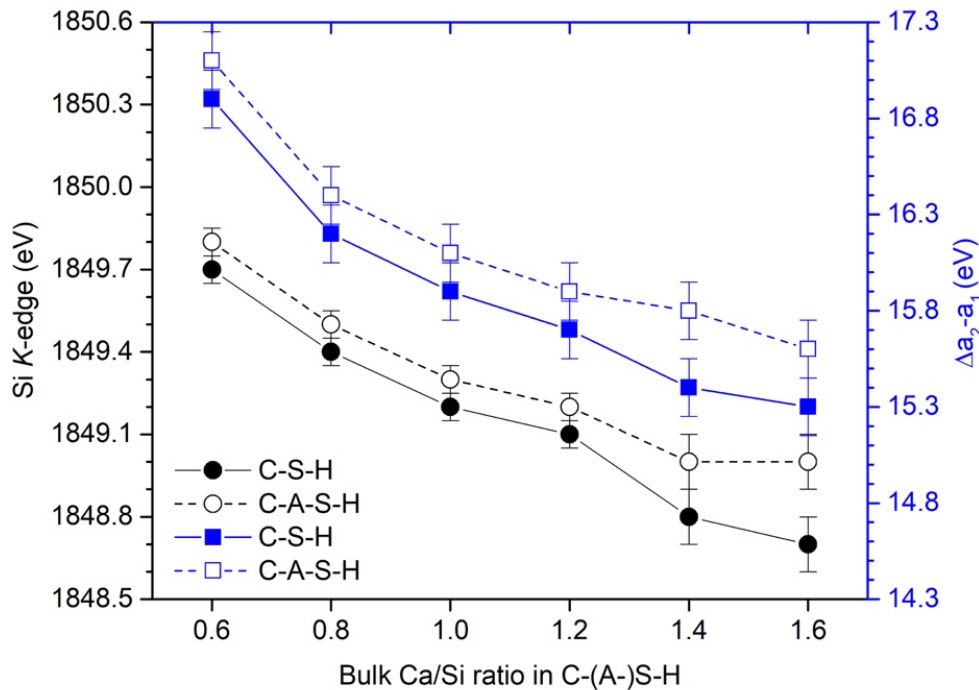


Figure 5.5. Si K-edge energy and energy difference between major and minor peak ($\Delta a_2 - a_1$) as a function of Ca/Si^* ratio of C-S-H (solid lines) and C-A-S-H with $\text{Al/Si}^* = 0.05$ (dashed lines) after 182 days of equilibration at 20 °C.

The major and minor peak positions (a_1 and a_2) of C-S-H increase as the Ca/Si ratio decreases, suggesting a contraction of average Si-O bond lengths [22] [23] [24] [25] [25, 26]. This trend is consistent with PDF analysis which showed slightly decreased average Si-O bond lengths as the Ca/Si^* decreases [27]. The inverse correlation between Si-O bond length and degree of silicate polymerization in the C-S-H samples with varying Ca/Si ratio is consistent with previous findings in many silicate minerals [25]. In general, the Si-O-Si bond angle is inversely correlated to Si-O bond length [28] (and thus directly related to the degree of silicate polymerization in C-S-H). Therefore, the shifted position of the Si K-edge to higher energies here implies that Si-O-Si bond angles in C-S-H increases as Ca/Si ratio decreases. The Si K-edge peak a_1 sharpens with a decreased Ca/Si ratio, suggesting an increased long-range ordering of silicate tetrahedra [29]. This interpretation is consistent with previous studies on C-S-H materials, namely, as Ca/Si ratio decreases, (1) the ordering of Si-O-Si bond angles increases [30]; (2) the Si-O-Si bond angle broadens [31]; (3) the Si $2p_{3/2}$ and $2s$ binding energies increase [32] [16]; and (4) the MCL of silicate chains in C-S-H increases [33]. Therefore, the energy difference between a_1 and a_2 peaks ($\Delta a_2 - a_1$) correlates to changing degrees of silicate polymerization in these silicate chains (see Figure 5.5).

$\text{Ca/Si}^* = 0.6-1.6$, $\text{Al/Si}^* = 0.05$, and equilibrium at 20 °C

The energies of the Si K-edges in the XANES spectra for the C-A-S-H samples increase by 0.1 to 0.3 eV with respect to C-S-H samples at each Ca/Si ratio increment (i.e., from $\text{Ca/Si}^* = 0.6$ to 0.8, etc.) due to the increase in degree of polymerization of aluminosilicate chains (Figures 5.4

and 5.5). The trend of an increased MCL with an increased amount of Al in C-(A-)S-H is well known [13]. As the MCL in C-(A-)S-H increases, the electron shielding on Si from zeolitic Ca decreases, which corresponds to Si atoms effectively becoming more negatively charged. Increased energies of the positions of Si K-edges in the XANES spectra imply slight contractions of Si-O bonds in C-(A-)S-H. At $\text{Ca/Si}^* = 1.4$ and 1.6 , the increment of Si K-edge of C-A-S-H products compared to C-S-H is 0.2 and 0.3 eV, respectively, which is slightly greater than that of C-A-S-H at lower Ca/Si ratio. This fact implies that aluminates tetrahedra link silicate dimers together and that Al prefers to occupy bridging sites, a significant proportion of which are vacant in C-S-H at Ca/Si ratios > 1 .

Cross-linked Q^3 species are not clearly identified in C-A-S-H samples equilibrated at 20°C , which is consistent with ^{29}Si NMR results of the same samples [10]. The Si K-edge peak, a_1 , (1849 eV - 1849.8 eV) of C-A-S-H is broadened relative to C-S-H and corresponds to $\text{Q}^2(1\text{Al})$ sites. As mentioned earlier, the energy of Si K-edge is dependent on the Si-O bond length and on the degree of silicate polymerization, while the position of a_2 peak is governed by the interatomic distance [34] [35] [21] [36]. Therefore, the energy difference between the a_1 and a_2 peaks, Δa_2-a_1 , is related to the degree of polymerization (i.e., MCL) and to the Si-O bond length of C-(A-)S-H. The ascending trends of Δa_2-a_1 and Si K-edge of C-A-S-H as the Ca/Si ratio decreases follows the same correlation of C-S-H, suggesting that the MCL increases with decreasing Ca/Si ratio. The value of Δa_2-a_1 in C-A-S-H at each Ca/Si ratio is also slightly larger than the value of Δa_2-a_1 in C-S-H (Figure 5.5), which implies the increase in MCL by Al incorporation.

Table 5.2. Peak positions and energy differences of Si K-edge XANES spectra of C-(A-)S-H equilibrated at 20°C . The estimated absolute errors are ± 0.05 units in positions of peak a_1 and at Ca/Si = 0.6 - 1.2 , ± 0.1 units in position of peak a_1 at Ca/Si = 1.4 - 1.6 , and ± 0.15 units in position of peak a_2 and energy differences between peaks a_1 and a_2 .

Ca/Si*	Peak a_1 (eV)	Peak a_2 (eV)	Δa_2-a_1 (eV)
Al/Si*=0			
0.6	1849.7	1866.6	16.9
0.8	1849.4	1865.6	16.2
1.0	1849.2	1865.1	15.9
1.2	1849.1	1864.8	15.7
1.4	1848.8	1864.6	15.4
1.6	1848.7	1864.0	15.3
Al/Si*=0.05			
0.6	1849.8	1866.9	17.1
0.8	1849.5	1865.9	16.4
1.0	1849.3	1865.4	16.1
1.2	1849.2	1865.1	15.9
1.4	1849.0	1864.8	15.8
1.6	1849.0	1864.6	15.6

Ca/Si* = 1, Al/Si* = 0-0.1, and equilibrium at 7-80 °C

At each equilibration temperature, in addition to the increase in energy difference, Δa_2-a_1 , the Si K-edge of C-(A-)S-H shifts to higher energy with an increased Al/Si* ratio (Figure 5.6 and Table 5.3). This increase suggests an elongation of aluminosilicates chains and marginal shortening of Si-O bonds, both resulting from Al incorporation. The shoulder at ~ 1853.8 - 1855.8 eV (peak a_4)

suggests that Q^3 and/or $Q^3(1Al)$ sites occur in the C-A-S-H sample equilibrated at 80 °C [22]. The position of the Si K-edge of C-A-S-H is shifted to a markedly higher energy at 80 °C due to the occurrence of these Q^3 and $Q^3(1Al)$ sites.

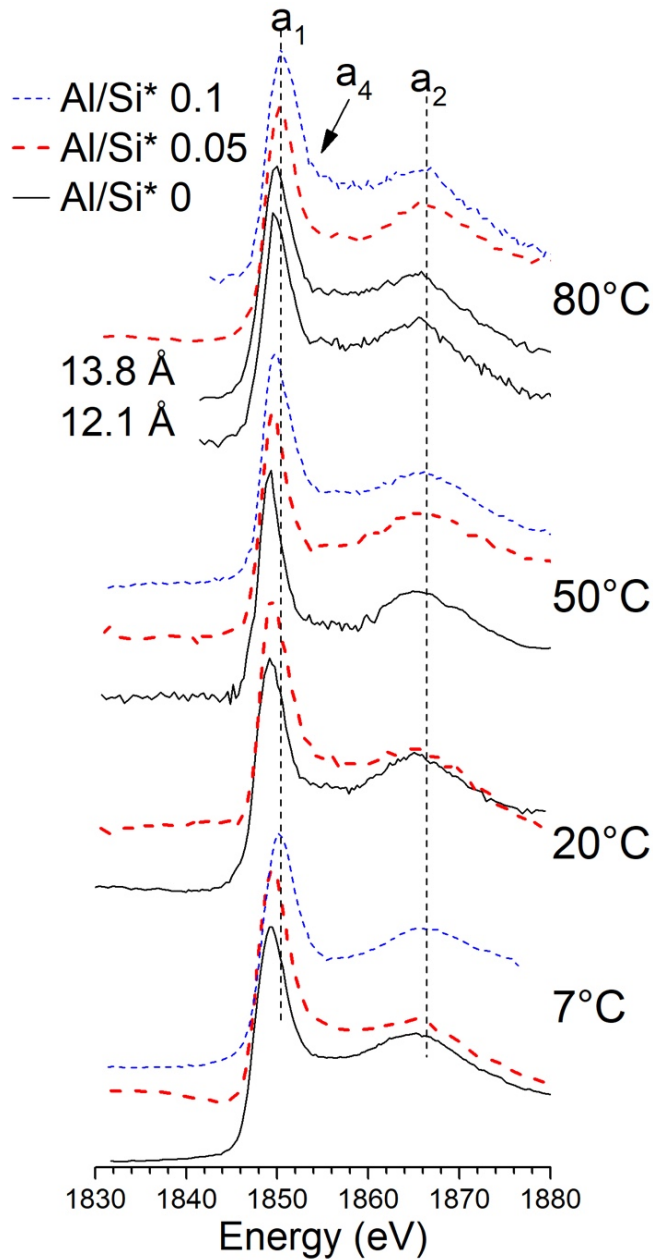


Figure 5.6. Si K-edge XANES spectra of C-S-H (solid lines, $Ca/Si^* = 1.0$), C-A-S-H (red long-dashed lines, $Al/Si^* = 0.05$, $Ca/Si^* = 1.0$), and C-A-S-H (blue short-dashed lines, $Al/Si^* = 0.1$, $Ca/Si^* = 1.0$) at different equilibration temperatures. The two C-S-H phases exist in the 80 °C sample, which are labeled with their average basal spacings. $Ca/Si^* =$ bulk Ca/Si . $Al/Si^* =$ bulk Al/Si .

Table 5.3. Features of Si K-edge XANES spectra for C-(A-)S-H samples ($\text{Ca/Si}^* = 1$) equilibrated at different temperatures. The estimated absolute errors are ± 0.05 units in positions of peak a_1 for C-(A-)S-H equilibrated at 7 °C - 50 °C, ± 0.1 units in position of peak a_1 at for C-(A-)S-H equilibrated at 80 °C, and ± 0.15 units in position of peak a_2 and energy differences between peaks a_1 and a_2 .

Al/Si*	Peak a_1 (eV)	Peak a_2 (eV)	$\Delta a_2 - a_1$ (eV)
Equilibrium at 7 °C			
0	1849.4	1865.3	15.9
0.05	1849.6	1865.6	16.0
0.1	1850.0	1866.2	16.2
Equilibrium at 20 °C			
0	1849.2	1865.1	15.9
0.05	1849.3	1865.4	16.1
Equilibrium at 50 °C			
0	1849.3	1865.1	15.8
0.05	1849.6	1865.7	16.1
0.1	1849.9	1866.1	16.2
Equilibrium at 80 °C			
0 (12.1 Å)	1849.6	1865.6	16.0
0 (13.8 Å)	1849.7	1865.8	16.1
0.05	1850.2	1866.5	16.3
0.1	1850.4	1866.9	16.5

The basal spacing shown in parentheses was measured by wide-angle X-ray scattering (WAXS, see Table 5.4). $\text{Al/Si}^* = \text{bulk Al/Si}$.

The Si K-edge and $\Delta a_2 - a_1$ of C-(A-)S-H products do not systematically vary across the equilibration temperature range of 7 to 80 °C, but positively correlate with the MCL of C-(A-)S-H (see Figure 5.7). The trend is consistent with the relationship between the energies, Ca/Si ratio and MCL of C-(A-)S-H at 20 °C, i.e., the energies increase with increasing MCL and a decreased Si-O bond length. Two distinct Si K-edge spectra are differentiated in C-S-H products synthesized at 80 °C, which are assigned to tobermorite-like structures with average basal spacing of 13.8 Å and 12.1 Å (See Table 5.4); the latter is more abundant in the product, which is consistent with [37]. The relatively higher Si K-edge and $\Delta a_2 - a_1$ of C-S-H with 13.8 Å average basal spacing suggests that it has a longer MCL than the C-S-H phase with an average basal spacing of 12.1 Å.

Table 5.4 Average (002) basal spacing and chemical composition in molar ratio of the C-(A-)S-H samples, and phases in solid assemblages of C-(A-)S-H systems

Initial molar ratio		Measured molar ratio			Average basal spacing, $d_{(002)}$ (Å) ± 0.05	Katoite	Strätlingite	Portlandite
Ca/Si*	Al/Si*	Ca/Si	Al/Si	Ca/(Al+Si)				
Temperature 20 °C								
0.8	0	0.80	-	0.8	13.63	-	-	-
	0.05	0.81	0.051	0.77	13.74	-	-	-
1.0	0	0.98	-	0.98	12.49	-	-	-
	0.05	0.99	0.05	0.94	12.80	-	-	-
1.6	0	1.38	-	1.38	9.56	-	-	Minor
	0.05	1.43	0.05	1.36	12.40	-	-	Minor
Temperature 7 °C								
1.0	0	0.99	-	0.99	11.87	-	-	-
	0.05	0.98	0.044	0.94	12.49	Minor	-	-
	0.1	0.98	0.09	0.90	13.19	Minor	Minor	-
Temperature 50 °C								
	0	0.99	-	0.99	12.63	-	-	-
	0.05	0.99	0.05	0.94	12.60	-	-	-
	0.1	0.96	0.086	0.88	13.63	Minor	-	-
Temperature 80 °C								
	0	0.99	-	0.99	12.13, 13.76	-	-	-
	0.05	0.99	0.05	0.94	11.43	-	-	-
	0.1	0.99	0.1	0.90	11.37	-	-	-

Final bulk molar ratios are reproduced from [4, 55]

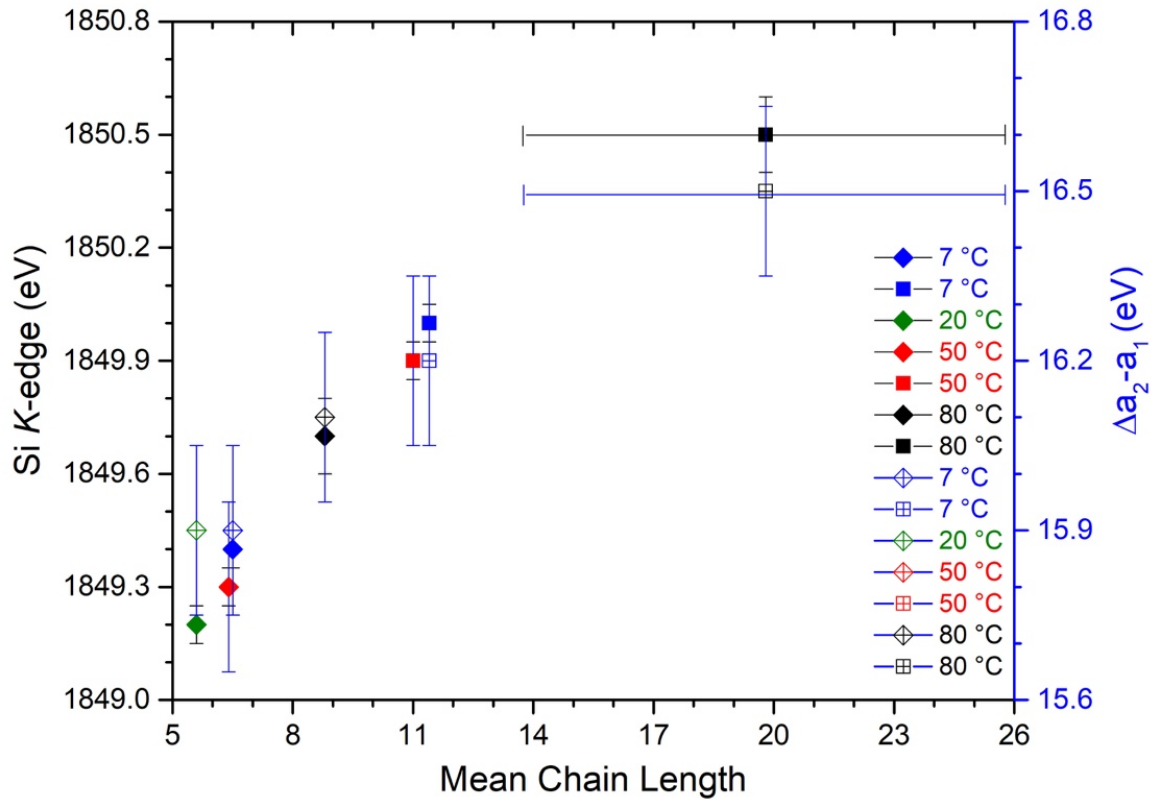


Figure 5.7. Si K-edge energy and energy difference between major and minor peak ($\Delta a_2 - a_1$) as a function of the MCL of C-(A-)S-H equilibrated at 7-80 °C. The uncertainty of MCL (reproduced from [38]) is ± 1.25 , except for the Al/Si* = 0.1 sample equilibrated at 80 °C, where the uncertainty of the MCL is represented by error bars. Al/Si* = 0.05 samples are marked as diamond and Al/Si* = 0.1 samples are marked as square. Al/Si* = bulk Al/Si. The large uncertainty of MCL of C-(A-)S-H at 80 °C is due to the large error of fitted Q^3 peaks in their ^{29}Si NMR spectra. The MCL is unitless.

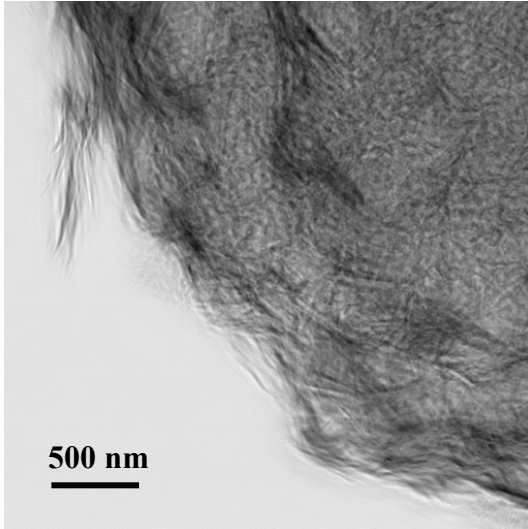
5.3 Morphology of C-(A-)S-H

Effect of Ca/Si and Al inclusion at 20 °C

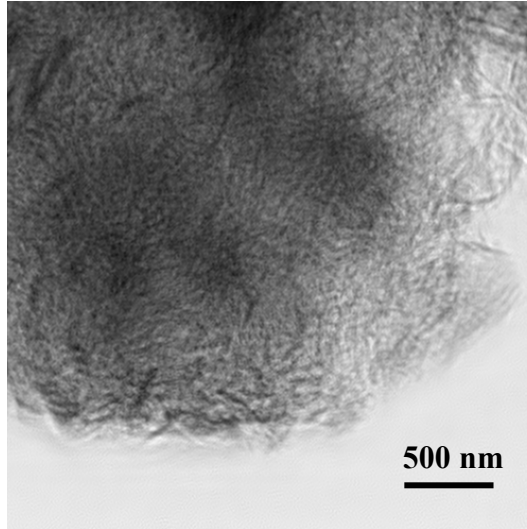
Ptychographic image of C-S-H (Ca/Si* = 1, equilibrated at 20 °C) shows that this product exhibits a crumpled foil-like morphology (Figure 5.8A). The foils at the fringe of the particle represent high length-to-width aspect ratio. The interior of the particle is a network of multiple densely-packed foils. It is expected that the features in this image represent the nature of C-S-H under ambient pressure. Richardson and Groves [39] observed similar morphological features in water-activated blast furnace slag/PC paste by TEM. The C-S-H outer product formed in hydrated $\beta\text{-C}_2\text{S}$, C_3S , and PC pastes in studies using TEM [40] [41] [42] [43] [44] and ptychographic imaging [45] [46] present fibers with more linear directional features. This is

possibly due to much higher lime concentrations in the pore solutions of these materials and/or much greater space constraints (much lower water-to-solid ratio).

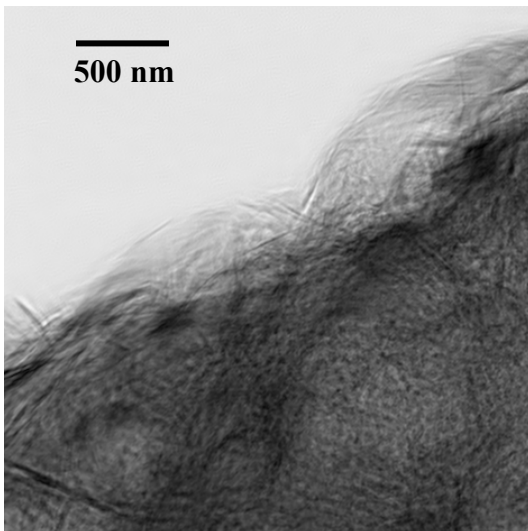
A $\text{Ca/Si}^*=1$ $\text{Al/Si}^*=0$ 20°C



B $\text{Ca/Si}^*=1$ $\text{Al/Si}^*=0.05$ 20°C



C $\text{Ca/Si}^*=0.6$ $\text{Al/Si}^*=0.05$ 20°C



D $\text{Ca/Si}^*=1.6$ $\text{Al/Si}^*=0.05$ 20°C

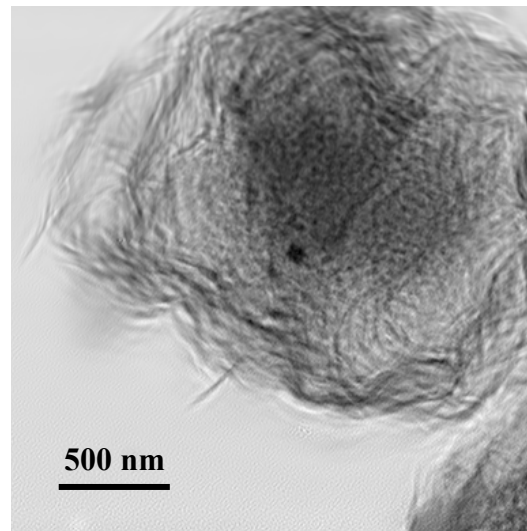


Figure 5.8. Ptychographic magnitude images of C-(A-)S-H equilibrated at 20°C for 182 days: A) $\text{Ca/Si}^* = 1.0$, $\text{Al/Si}^* = 0$; B) $\text{Ca/Si}^* = 1.0$, $\text{Al/Si}^* = 0.05$; C) $\text{Ca/Si}^* = 0.6$, $\text{Al/Si}^* = 0.05$; and D) $\text{Ca/Si} = 1.6$, $\text{Al/Si}^* = 0.05$. $\text{Ca/Si}^* = \text{bulk Ca/Si}$. $\text{Al/Si}^* = \text{bulk Al/Si}$.

A recent TEM study showed that the C-S-H precipitated at $\text{Ca/Si}^*=1$ and using a similar water-to-solid ratio is also foil-like. The slight morphological difference of the C-S-H phase in that study relative to the present work can be attributed to different drying and vacuum conditions [47]. The morphology of C-S-H in hydrated C_3S in that study transitioned from foils to fibers as Ca concentration in solution increases [33].

Figure 5.9 shows the small angle scattering curves obtained from ptychographic image. A plateau is observed in C-S-H and C-A-S-H equilibrated at 20 °C. suggesting the presence of concentrated packing of 'platelet' building blocks and strong polydispersion [44]. The calculated average thickness of this C-S-H platelet based on a lamellar model to be ~7 nm (from ptychographic magnitude image); therefore, considering the basal spacing measured in Table 5.4. the average number of layers of the C-S-H platelets in the c-direction is ~5.6. A TEM study shows that C-S-H equilibrated at 20 °C from CaO-SiO₂-H₂O system is also foil-like at Ca/Si = 0.75-1.42, and the thickness of the foil is ~ 5-8 nm [33]. The distinction in thickness from the present work is expected due to different drying processes, vacuum conditions, and hydration ages.

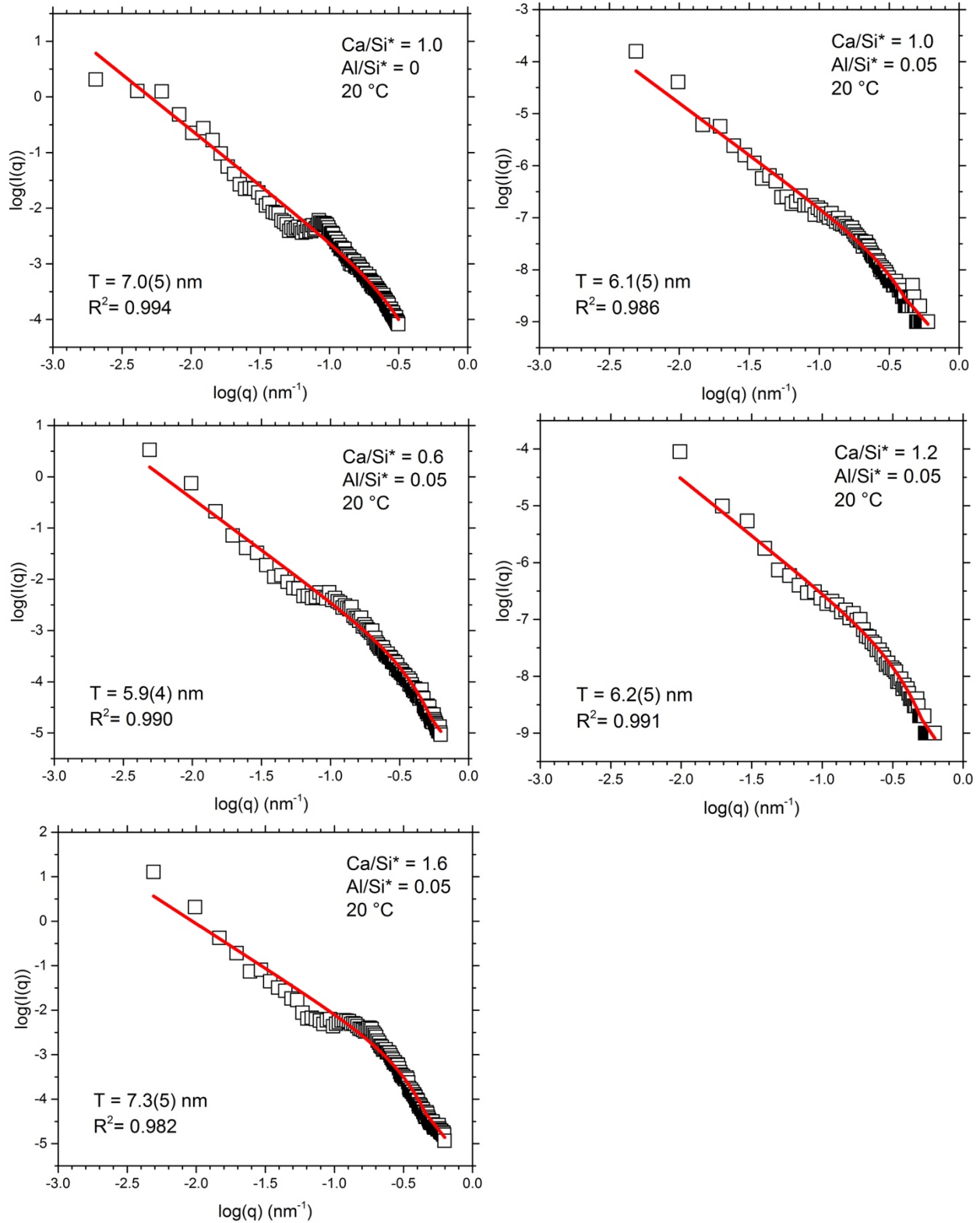


Figure 5.9 Small angle scattering curves obtained from ptychographic images of C-(A)-S-H equilibrated at 20 °C. Fitted layer thickness (T) and coefficient of determination (R^2) of the fitting are indicated in the plots. The data were fitted with a Guinier–Porod lamellar model, more

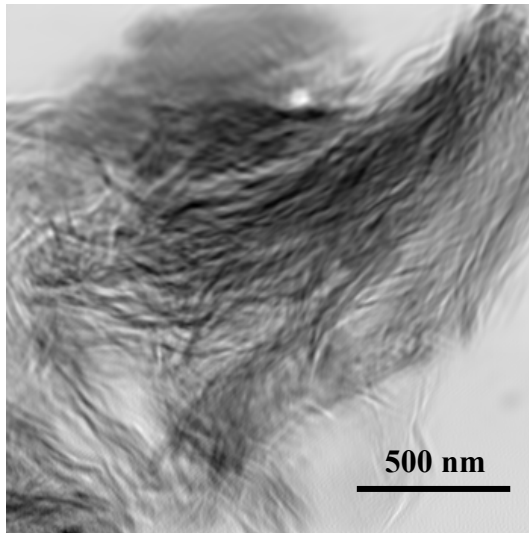
details can be found in the appendix (Chapter 8). Estimated standard deviation of the thickness is shown in parentheses. Ca/Si^* = bulk Ca/Si molar ratio. Al/Si^* =bulk Al/Si molar ratio

Incorporation of Al into the C-A-S-H phase at 20 °C does not greatly alter its morphology, which is also identified as a network of crumpled foils. It appears similar to the outer product of water-activated slag hydrated for 3.5 years [48]. Variation in morphology of C-A-S-H ($\text{Al/Si}^* = 0.05$, equilibrated at 20 °C) is not observed at $\text{Ca/Si}^* = 0.6, 1, 1.2, \text{ or } 1.6$ (Figure 5.8), suggesting that the Ca/Si ratio does not significantly govern the nano-morphology of C-A-S-H equilibrated at 20 °C. The calculated average thickness of C-A-S-H platelets at this temperature is 5.9-7.3 nm, which does not vary greatly as a function of the Ca/Si ratio, therefore the average number of layers of the C-A-S-H platelets ranges from ~ 4.3 to ~ 5.9 . TEM micrographs by Rodriguez et al. [33] show that C-S-H synthesized in the $\text{CaO-SiO}_2\text{-H}_2\text{O}$ system at 20 °C always appears to be foil-like regardless of Ca/Si ratio. The slight morphological difference between the two studies can be attributed to the Al inclusion, drying process and other factors (e.g., vacuum condition and water-to-solid ratio).

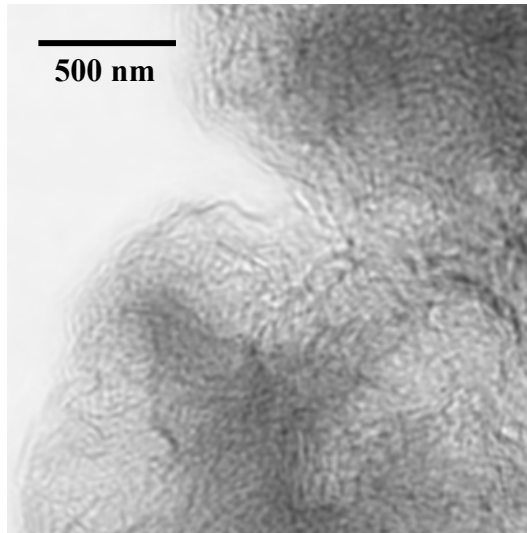
Effects of temperature and cross-linking

The C-A-S-H phases ($\text{Ca/Si}^* = 1, \text{ Al/Si}^* = 0.05$) precipitated using equilibration temperatures of 7 to 50 °C are morphologically similar (Figure 5.10), while the morphological features of C-A-S-H phases appear to be significantly different at 80 °C (Figure 5.11). The average thickness of C-A-S-H platelet is 5.3-6.5 nm for the C-A-S-H samples equilibrated at 7-50 °C, while the average thickness of C-A-S-H for 80 °C samples is 14.5- 14.7 nm (Figure 5.12). Thus, the average number of stacked calcium silicate basal layers of the C-A-S-H platelets is ~ 4.8 -5.3 for the 7-50 °C samples, while the average number of layers is 12.7- 12.9 for the 80 °C samples. C-A-S-H samples with different Al/Si^* ratios at 80 °C all present foil-predominant network, and the C-A-S-H at $\text{Al/Si}^* = 0.1$ presents much thicker and wider agglomeration of foil structure than that at $\text{Al/Si}^* = 0.05$. This observation shows that the Al incorporation at 80 °C significantly alters the morphology of C-(A-)S-H. This effect is likely related to the increased crystalline order of this sample, although it may also be caused by its cross-linking of aluminosilicate chains and noticeably increased degree of C-A-S-H chain polymerization.

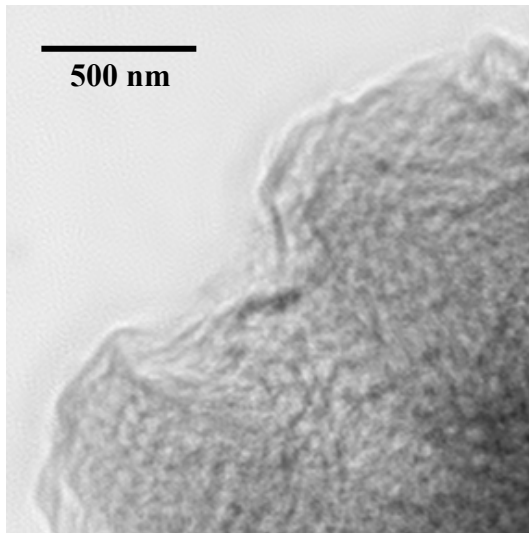
A Ca/Si*=1 Al/Si*=0.05 7 °C



B Ca/Si*=1 Al/Si*=0.05 20 °C



C Ca/Si*=1 Al/Si*=0.05 50 °C



D Ca/Si*=1 Al/Si*=0.05 80 °C

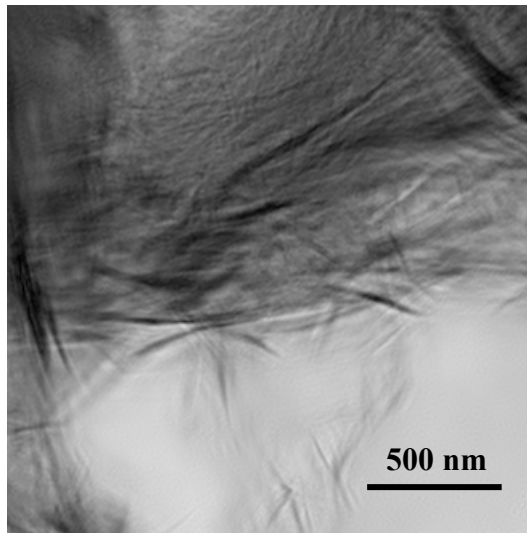
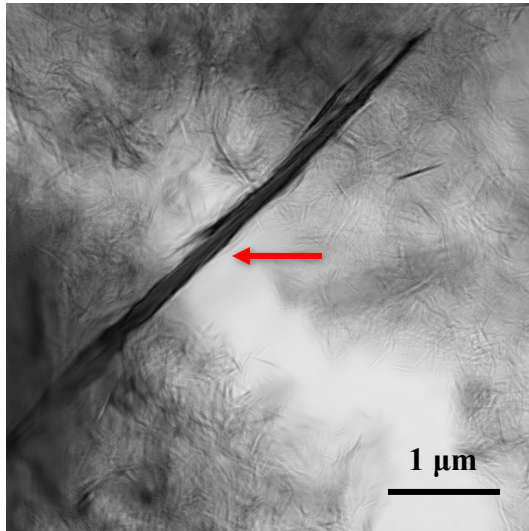
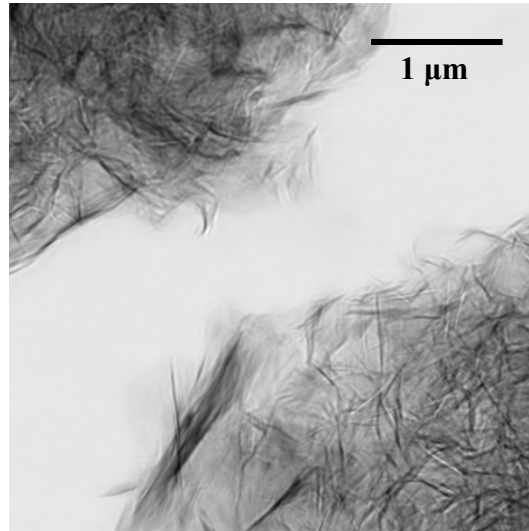


Figure 5.10. Ptychographic magnitude images of C-A-S-H with Ca/Si* = 1 and Al/Si* = 0.05; A) equilibrated for 365 days at 7 °C; B) equilibrated for 182 days at 20 °C; C) equilibrated for 56 days at 50 °C; D) equilibrated for 56 days at 80 °C.

A Ca/Si* = 1 Al/Si* = 0 80 °C



B Ca/Si* = 1 Al/Si* = 0.05 80 °C



C Ca/Si* = 1 Al/Si* = 0.1 80 °C

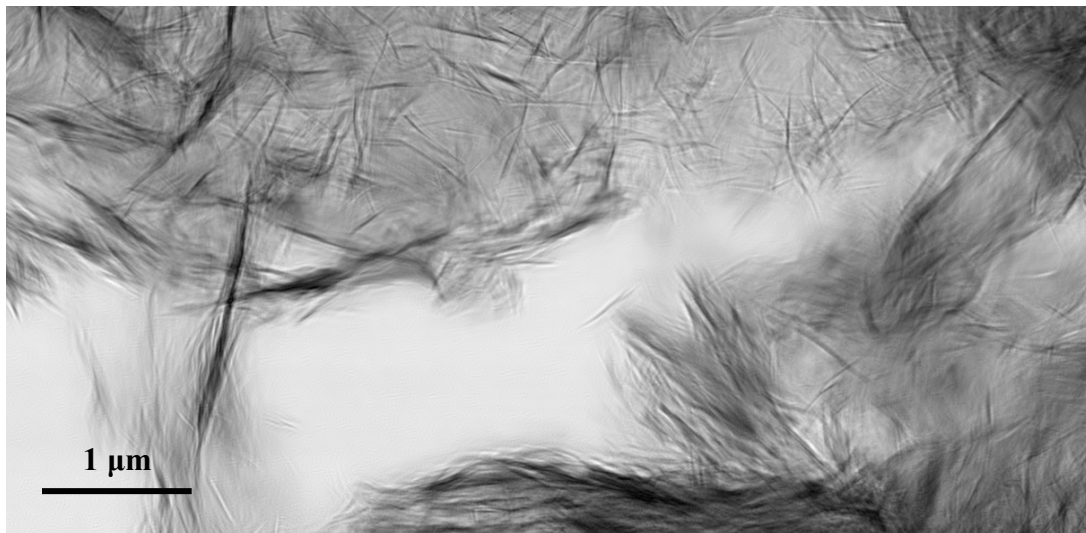


Figure 5.11. A) Ptychographic magnitude images of C-(A-)S-H equilibrated for 56 days at 80 °C: A) Ca/Si* = 1, Al/Si* = 0; B) Ca/Si* = 1, Al/Si* = 0.05; C) Ca/Si* = 1, Al/Si* = 0.1. Tobermorite crystal with an average basal spacing of 13.8 Å is indicated by a red arrow. Ca/Si* = bulk Ca/Si molar ratio. Al/Si* = bulk Al/Si molar ratio.

For samples equilibrated at 80 °C, the C-S-H foils are thinner and shorter than the C-A-S-H foils (both samples have Ca/Si* = 1.0). However, these foils are coarser than the C-(A-)S-H foils equilibrated at 7 °C -50 °C (Ca/Si* = 1.0); the average basal spacing of the foils equilibrated at 80 °C is 12.1 Å. SAS calculations confirm this significant change in morphology, which give an average stacked C-S-H platelet thickness for the 80 °C sample of 8.5 nm and an average number of calcium silicate basal layers of ~7. The coarse fibers with variable lengths ranging from hundreds of nanometers to a few microns in C-S-H at 80 °C correspond to a tobermorite-like structure with an average basal spacing of ~13.8 Å. The change in morphology in terms of elevated temperature is different from C-S-H gels in hydrated C₃S paste at 80 °C [42], which can

be explained by the difference in the lime concentration of pore solution, space constraint and reaction kinetics.

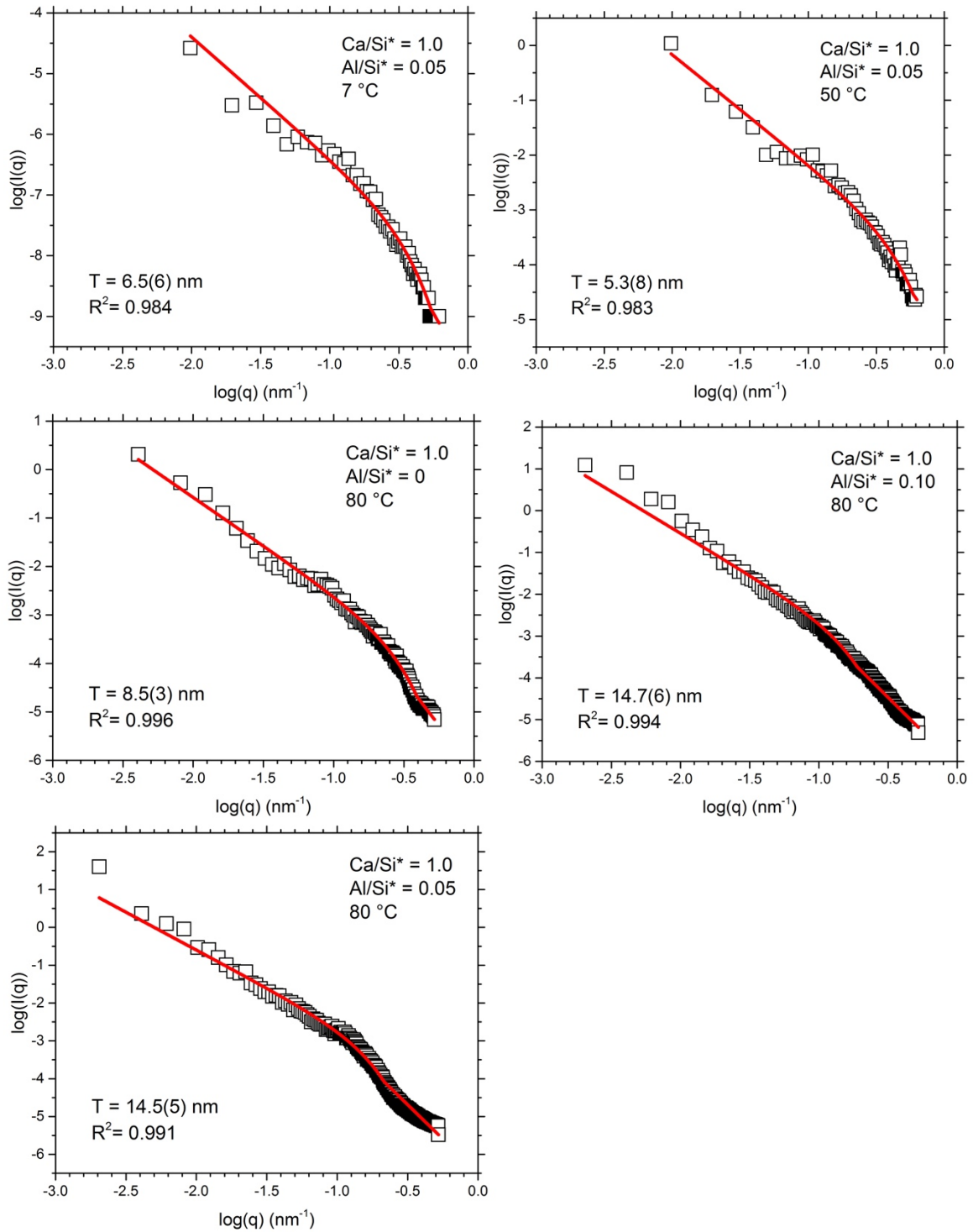


Figure 5.12. Small angle scattering curves obtained from ptychographic images of C-(A-)S-H equilibrated at 7 °C, 50 °C, and 80 °C. Fitted layer thickness (T) and coefficient of determination

(R^2) of the fitting are indicated in the plots. The data were fitted with a Guinier–Porod lamellar model, more details can be found in the appendix (Chapter 8). Estimated standard deviation of the thickness of the layer is shown in parentheses. $\text{Ca/Si}^* = \text{bulk Ca/Si molar ratio}$. $\text{Al/Si}^* = \text{bulk Al/Si molar ratio}$

5.4 A molecular-to-nanoscale model of C-A-S-H

A molecular-to-nanoscale model (Figure 5.13) of the hypothetical C-A-S-H structure at equilibration temperature of 7 °C to 80 °C is proposed based on the results of coordination environment, morphology, and model fitting of SAS in terms of the stacked calcium silicate basal layer structure. C-A-S-H equilibrated at 7 °C - 50 °C is structurally analogous to defective tobermorite, which contains CaO_7 sheets flanked with “dreierketten” – tetrahedral aluminosilicate chains – on one side and counter-ions (highly distorted six-fold coordinated Ca and five-fold coordinated Al) and water in an interlayer on the other. In this temperature range, cross-linked sites do not exist, and Al is preferably incorporated at bridging sites (Q^2_B) of the aluminosilicate chains. The basal spacing of C-A-S-H structure varies from ~12 to 14 Å with varying Ca/Si ratios due to the Al-uptake and zeolitic content (Ca ions and water). The stacked thickness of lamellar building blocks of C-A-S-H at 7 °C - 50 °C ranges from 5.3 to 7.3 nm, representing ~4-6 stacked layers along the c-axis. Therefore, the building blocks constitute a network of crumpled densely-packed foils at the nanoscale.

Tetrahedral-coordinated Al also substitutes into cross-linked sites (Q^3) of chains in C-A-S-H equilibrated at 80 °C, which decreases the basal spacing to ~11.4 Å and significantly increases the polymerization of aluminosilicate chains. The elevated equilibration temperature does not alter the coordination symmetry of Ca species in C-A-S-H structure but triggers a longer-range of ordering of CaO_7 sheets. The average thickness of C-A-S-H building blocks at 80 °C is ~14.6 nm, denoting ~13 stacked calcium silicate basal layers along the c-axis. The coarser C-A-S-H building blocks constitute a foil-predominant network with less curvature and wider and thicker agglomeration at the nanoscale.

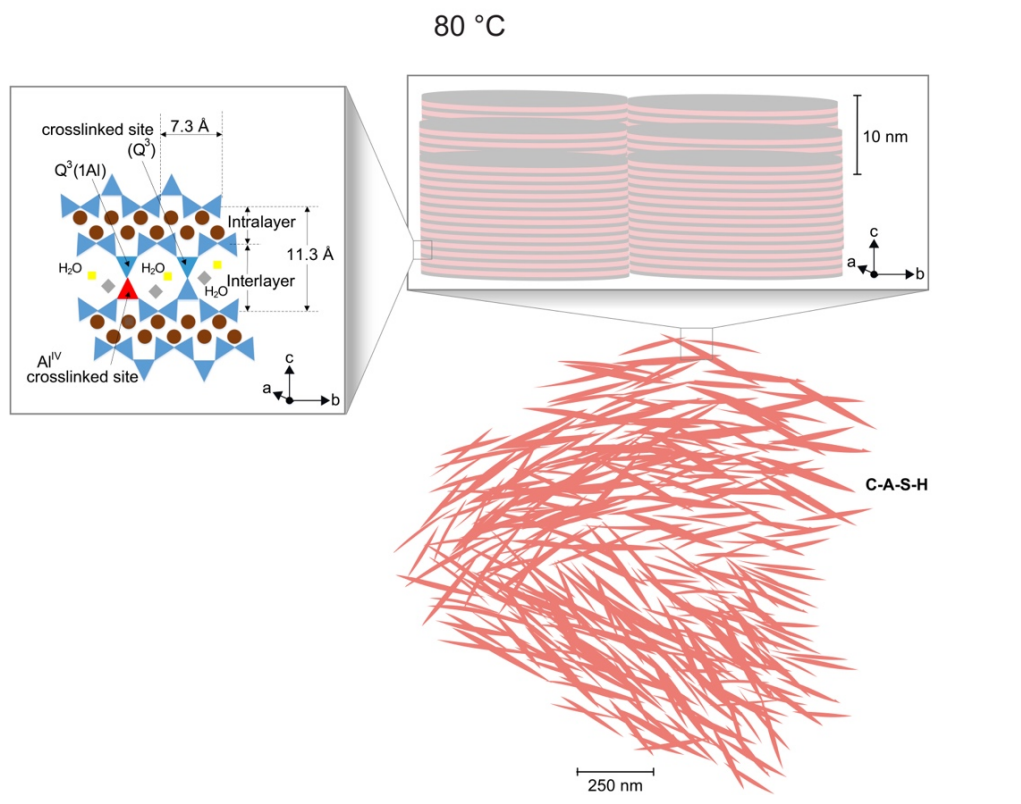
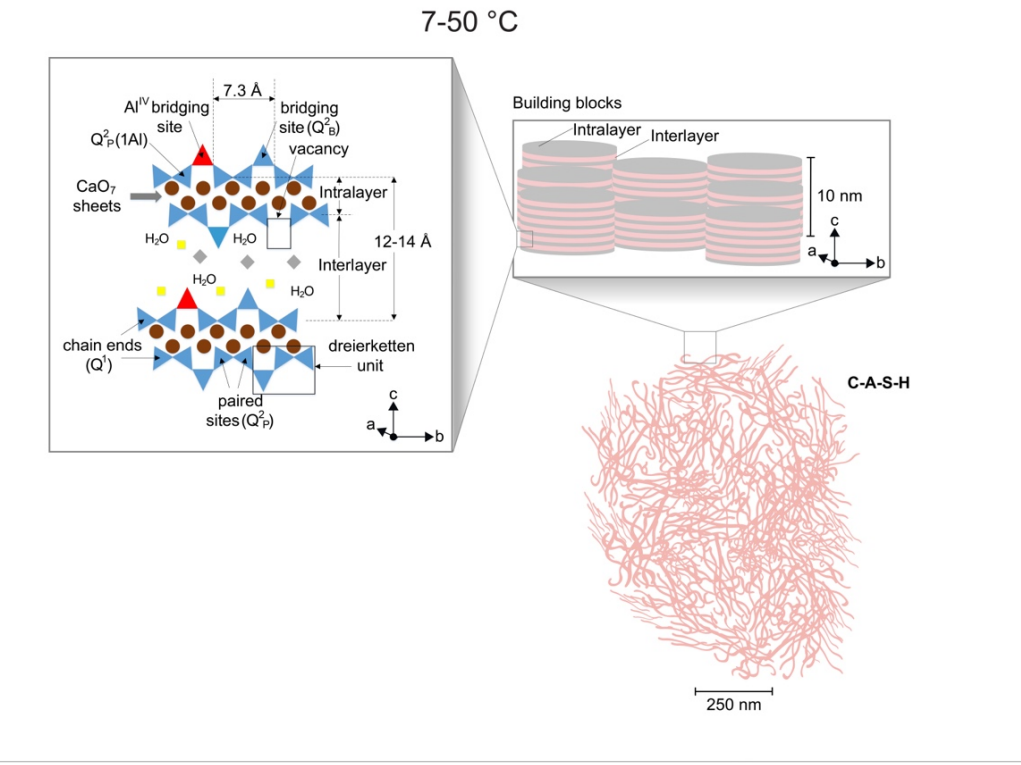


Figure 5.13. Schematic diagram of nanocrystalline synthetic C-A-S-H (equilibration temperature of 7-50 °C and 80 °C). The brown circles represent Ca species in the CaO_7 sheets, and the blue

and red triangles denote SiO_4 and AlO_4 tetrahedron sites, respectively. The grey diamonds and yellow squares are charge-balancing cations (e.g., Ca species and five-fold coordinated Al species) in the interlayer. The pink and grey alternating stacked layers of the nano building blocks represent the interlayer and intralayer, respectively. The rouge foils denote the networking structure of the synthetic C-A-S-H at the nanoscale.

5.5 Conclusions

This chapter has presented a synchrotron-based X-ray micro-spectroscopy study of C-(A-)S-H with different bulk Ca/Si and Al/Si molar ratios, that were equilibrated at temperatures at 7 °C, 20 °C, 50 °C, and 80 °C. Apart from the seven-fold coordinated Ca in the intralayer of C-(A-)S-H, the extra Ca that enters the interlayer are more likely six-fold coordinated in a highly distorted octahedral symmetry. The ordering of the Ca environment increases as the Al content and equilibration temperature increase. Calcium environments in C-(A-)S-H are similar to tobermorite. The coordination symmetry of Ca is highly distorted irrespective bulk Ca/Si molar ratio, Al uptake, and equilibration temperature.

The Si K-edge shifts to higher energy with increased mean chain length of (alumino)silicate chains. The energy separation between major and minor peak at the Si K-edge positively correlates with the degree of polymerization of its aluminosilicate chains. The Si-O bond length increases as the bulk Ca/Si molar ratio increases. Al incorporation leads to contraction of Si-O bonds in silicate tetrahedra in C-A-S-H. AFm-like species are not interstratified in the interlayer structure or precipitate on the external surface of C-A-S-H. The TAH is either not Ca-bearing or its Ca is structurally similar to the synthetic C-(A-)S-H. Aluminum is preferably incorporated at bridging sites and is also accommodated in cross-linked bridging sites at equilibrium temperature of 80 °C.

C-S-H at bulk Ca/Si molar ratio of 1 formed at 20 °C preferably presents crumpled nano foils with various lengths. The aluminum incorporation of C-S-H at equilibrium temperature of 7-50 °C and bulk Ca/Si ratio do not change its morphology. C-A-S-H equilibrated at 80 °C present coarser foils, and the foils are much thicker and longer with more Al inclusion. The building-block of all C-(A-)S-H samples is lamellar. C-A-S-H is morphologically similar with comparable lamellar thickness irrespective of Ca/Si ratio or equilibration temperature at 7-50 °C. The lamellar thickness of C-S-H equilibrated at equilibrium temperature of 80 °C is slightly enhanced, and the lamellar thickness is much greater with Al inclusion at equilibrium temperature of 80 °C.

These results provide new insight into the morphology of C-(A-)S-H and the possible nature of TAH in C-A-S-H products, the coordination of Ca-O, and the environment of Si in C-(A-)S-H with different compositions and synthesized at different equilibration temperatures. Therefore, this chapter yields an improved understanding of C-(A-)S-H chemistry, which will enhance the understanding of the performance of hydrated PC blends in service.

5.6 References

1. Naftel, S.J., T.K. Sham, Y.M. Yiu and B.W. Yates, Calcium L-edge XANES study of some calcium compounds. *Journal of Synchrotron Radiation*, 2001. **8**: p. 255-257.
2. Ko, J.P., X-ray Absorption Near-edge Structure (XANES) of calcium L_{2,3} edges of various calcium compounds and X-ray Excited Optical Luminescence (XEOL) studies of luminescent calcium compounds. *X-Ray Absorption Fine Structure--XAFS*, 2007. **13**(882): p. 538-540.
3. Degroot, F.M.F., J.C. Fuggle, B.T. Thole and G.A. Sawatzky, 2p x-ray absorption of 3d transition-metal compounds - an atomic multiplet description including the crystal-field. *Physical Review B*, 1990. **42**(9): p. 5459-5468.
4. Geng, G., R.J. Myers, A.L. Kilcoyne, J. Ha and P.J. Monteiro, Ca L_{2,3}-edge near edge X-ray absorption fine structure of tricalcium aluminate, gypsum, and calcium (sulfo) aluminate hydrates. *American Mineralogist*, 2017. **102**(4): p. 900-908.
5. Pellenq, R.J.-M., A. Kushima, R. Shahsavari, K.J. Van Vliet, M.J. Buehler, S. Yip and F.-J. Ulm, A realistic molecular model of cement hydrates. *Proceedings of the National Academy of Sciences*, 2009. **106**(38): p. 16102-16107.
6. Fleet, M.E. and X.Y. Liu, Calcium L_{2,3}-edge XANES of carbonates, carbonate apatite, and oldhamite (CaS). *American Mineralogist*, 2009. **94**(8-9): p. 1235-1241.
7. Hanhan, S., A.M. Smith, M. Obst and A.P. Hitchcock, Optimization of analysis of soft X-ray spectromicroscopy at the Ca 2p edge. *Journal of Electron Spectroscopy and Related Phenomena*, 2009. **173**(1): p. 44-49.
8. L'Hôpital, E., B. Lothenbach, K. Scrivener and D. Kulik, Alkali uptake in calcium alumina silicate hydrate (CASH). *Cement and Concrete Research*, 2016. **85**: p. 122-136.
9. Kirkpatrick, R.J., G.E. Brown, N. Xu and X.D. Cong, Ca X-ray absorption spectroscopy of C-S-H and some model compounds. *Advances in Cement Research*, 1997. **9**(33): p. 31-36.
10. L'Hôpital, E., B. Lothenbach, D. Kulik and K. Scrivener, Influence of calcium to silica ratio on aluminium uptake in calcium silicate hydrate. *Cement and Concrete Research*, 2016. **85**: p. 111-121.
11. Richardson, I.G. and G.W. Groves, Microstructure and microanalysis of hardened ordinary Portland-cement pastes. *Journal of Materials Science*, 1993. **28**(1): p. 265-277.
12. Gartner, E., I. Maruyama and J. Chen, A new model for the CSH phase formed during the hydration of Portland cements. *Cement and Concrete Research*, 2017. **97**: p. 95-106.
13. L'Hôpital, E., B. Lothenbach, G. Le Saout, D. Kulik and K. Scrivener, Incorporation of aluminium in calcium-silicate-hydrates. *Cement and Concrete Research*, 2015. **75**: p. 91-103.
14. Faucon, P., A. Delagrave, J. Petit, C. Richet, J. Marchand and H. Zanni, Aluminum incorporation in calcium silicate hydrates (CSH) depending on their Ca/Si ratio. *The Journal of Physical Chemistry B*, 1999. **103**(37): p. 7796-7802.
15. Geng, G.Q., R.J. Myers, M.J.A. Qomi and P.J.M. Monteiro, Densification of the interlayer spacing governs the nanomechanical properties of calcium-silicate-hydrate. *Scientific Reports*, 2017. **7**.
16. Black, L., K. Garbev, G. Beuchle, P. Stemmermann and D. Schild, X-ray photoelectron spectroscopic investigation of nanocrystalline calcium silicate hydrates synthesised by reactive milling. *Cement and Concrete Research*, 2006. **36**(6): p. 1023-1031.
17. Geng, G., J. Li, Y.-S. Yu, D.A. Shapiro, D.A. Kilcoyne and P.J. Monteiro, Nanometer-resolved spectroscopic study reveals the conversion mechanism of CaO·Al₂O₃·10H₂O

- to $2\text{CaO} \cdot \text{Al}_2\text{O}_3 \cdot 8\text{H}_2\text{O}$ and $3\text{CaO} \cdot \text{Al}_2\text{O}_3 \cdot 6\text{H}_2\text{O}$ at an elevated temperature. *Crystal Growth & Design*, 2017. **17**(8): p. 4246-4253.
18. Renaudin, G., J. Russias, F. Leroux, F. Frizon and C. Cau-dit-Coumes, Structural characterization of C–S–H and C–A–S–H samples—part I: long-range order investigated by Rietveld analyses. *Journal of Solid State Chemistry*, 2009. **182**(12): p. 3312-3319.
 19. Andersen, M.D., H.J. Jakobsen and J. Skibsted, A new aluminium-hydrate species in hydrated Portland cements characterized by ^{27}Al and ^{29}Si MAS NMR spectroscopy. *Cement and Concrete Research*, 2006. **36**(1): p. 3-17.
 20. Li, D., G.M. Bancroft, M.E. Fleet and X.H. Feng, Silicon K-edge XANES spectra of silicate minerals. *Physics and Chemistry of Minerals*, 1995. **22**(2): p. 115-122.
 21. Li, D., G.M. Bancroft, M. Kasrai, M.E. Fleet, X.H. Feng, K.H. Tan and B.X. Yang, High-resolution Si K-edge and L_{2,3}-edge XANES of alpha-quartz and stishovite. *Solid State Communications*, 1993. **87**(7): p. 613-617.
 22. Cabaret, D., M. Le Grand, A. Ramos, A.M. Flank, S. Rossano, L. Galois, G. Calas and D. Ghaleb, Medium range structure of borosilicate glasses from Si K-edge XANES: a combined approach based on multiple scattering and molecular dynamics calculations. *Journal of Non-Crystalline Solids*, 2001. **289**(1-3): p. 1-8.
 23. Henderson, G.S., A Si K-edge EXAFS/XANES study of sodium-silicate glasses. *Journal of Non-Crystalline Solids*, 1995. **183**(1-2): p. 43-50.
 24. Henderson, G.S. and M.E. Fleet, The structure of titanium silicate glasses investigated by Si K-edge X-ray absorption spectroscopy. *Journal of Non-Crystalline Solids*, 1997. **211**(3): p. 214-221.
 25. Bianconi, A., M. Dellariccia, P.J. Durham and J.B. Pendry, Multiple-scattering resonances and structural effects in the x-ray-absorption near-edge spectra of Fe-Ii and Fe-Iii hexacyanide complexes. *Physical Review B*, 1982. **26**(12): p. 6502-6508.
 26. Bunker, G., Introduction to XAFS: a practical guide to X-ray absorption fine structure spectroscopy. Cambridge University Press, 2010.
 27. Soyer-Uzun, S., S.R. Chae, C.J. Benmore, H.R. Wenk and P.J.M. Monteiro, Compositional evolution of calcium silicate hydrate (C-S-H) structures by total x-ray scattering. *Journal of the American Ceramic Society*, 2012. **95**(2): p. 793-798.
 28. Smith, K.A., R.J. Kirkpatrick, E. Oldfield and D.M. Henderson, High-resolution silicon- ^{29}Si nuclear magnetic resonance spectroscopic study of rock-forming silicates. *American Mineralogist*, 1983. **68**(11-12): p. 1206-1215.
 29. Hill, R. and G. Gibbs, Variation in $d(\text{TO})$, $d(\text{T}\cdots\text{T})$ and $\angle\text{TOT}$ in silica and silicate minerals, phosphates and aluminates. *Acta Crystallographica Section B: Structural Crystallography and Crystal Chemistry*, 1979. **35**(1): p. 25-30.
 30. Yu, P., R.J. Kirkpatrick, B. Poe, P.F. McMillan and X.D. Cong, Structure of calcium silicate hydrate (C-S-H): Near-, mid-, and far-infrared spectroscopy. *Journal of the American Ceramic Society*, 1999. **82**(3): p. 742-748.
 31. Garbev, K., P. Stemmermann, L. Black, C. Breen, J. Yarwood and B. Gasharova, Structural features of C-S-H(I) and its carbonation in air - A Raman spectroscopic study. Part I: Fresh phases. *Journal of the American Ceramic Society*, 2007. **90**(3): p. 900-907.
 32. Black, L., K. Garbev, P. Stemmermann, K.R. Hallam and G.C. Allen, Characterisation of crystalline C-S-H phases by X-ray photoelectron spectroscopy. *Cement and Concrete Research*, 2003. **33**(6): p. 899-911.

33. Rodriguez, E.T., I.G. Richardson, L. Black, E. Boehm-Courjault, A. Nonat and J. Skibsted, Composition, silicate anion structure and morphology of calcium silicate hydrates (C-S-H) synthesised by silica-lime reaction and by controlled hydration of tricalcium silicate (C3S). *Advances in Applied Ceramics*, 2015. **114**(7): p. 362-371.
34. Li, D., M.E. Fleet, G.M. Bancroft, M. Kasrai and Y.M. Pan, Local-Structure of Si and P in $\text{SiO}_2\text{-P}_2\text{O}_5$ and $\text{Na}_2\text{O-SiO}_2\text{-P}_2\text{O}_5$ Glasses - a XANES Study. *Journal of Non-Crystalline Solids*, 1995. **188**(1-2): p. 181-189.
35. Li, D., G.M. Bancroft, M. Kasrai, M.E. Fleet, R.A. Secco, X.H. Feng, K.H. Tan and B.X. Yang, X-ray-absorption spectroscopy of silicon dioxide (SiO_2) polymorphs - the structural characterization of opal. *American Mineralogist*, 1994. **79**(7-8): p. 622-632.
36. Li, D., G.M. Bancroft, M. Kasrai, M.E. Fleet, X.H. Feng and K.H. Tan, High-resolution Si and P K-edge and L-edge XANES spectra of crystalline SiP_2O_6 and amorphous $\text{SiO}_2\text{-P}_2\text{O}_5$. *American Mineralogist*, 1994. **79**(7-8): p. 785-788.
37. Geng, G., R.J. Myers, J. Li, R. Maboudian, C. Carraro, D.A. Shapiro and P.J. Monteiro, Aluminum-induced dreierketten chain cross-links increase the mechanical properties of nanocrystalline calcium aluminosilicate hydrate. *Scientific Reports*, 2017. **7**: p. 44032.
38. Myers, R.J., E. L'Hopital, J.L. Provis and B. Lothenbach, Effect of temperature and aluminium on calcium (alumino)silicate hydrate chemistry under equilibrium conditions. *Cement and Concrete Research*, 2015. **68**: p. 83-93.
39. Richardson, I.G. and G.W. Groves, Microstructure and microanalysis of hardened cement pastes involving ground granulated blast-furnace slag. *Journal of Materials Science*, 1992. **27**(22): p. 6204-6212.
40. Richardson, I.G., The nature of C-S-H in hardened cements. *Cement and Concrete Research*, 1999. **29**(8): p. 1131-1147.
41. Richardson, I.G., The calcium silicate hydrates. *Cement and Concrete Research*, 2008. **38**(2): p. 137-158.
42. Richardson, I.G., Tobermorite/jennite- and tobermorite/calcium hydroxide-based models for the structure of C-S-H: applicability to hardened pastes of tricalcium silicate, beta-dicalcium silicate, Portland cement, and blends of Portland cement with blast-furnace slag, metakaolin, or silica fume. *Cement and Concrete Research*, 2004. **34**(9): p. 1733-1777.
43. Richardson, I.G., The nature of the hydration products in hardened cement pastes. *Cement & Concrete Composites*, 2000. **22**(2): p. 97-113.
44. Rodger, S. A., & Groves, G. W. Electron microscopy study of ordinary Portland cement and ordinary Portland cement-pulverized fuel ash blended pastes. *Journal of the American Ceramic Society*, 1989, **72**(6), 1037-1039.
45. Bae, S., R. Taylor, D. Shapiro, P. Denes, J. Joseph, R. Celestre, S. Marchesini, H. Padmore, T. Tyliczszak and T. Warwick, Soft X-ray ptychographic imaging and morphological quantification of calcium silicate hydrates (C-S-H). *Journal of the American Ceramic Society*, 2015. **98**(12): p. 4090-4095.
46. Li, J., G. Geng, W. Zhang, Y.-S. Yu, D.A. Shapiro and P.J. Monteiro, The Hydration of β - and α' -H-dicalcium silicates: An X-ray spectromicroscopic study. *ACS Sustainable Chemistry & Engineering*, 2019. **7**(2): p. 2316-2326.
47. Fonseca, P. and H.M. Jennings, The effect of drying on early-age morphology of C-S-H as observed in environmental SEM. *Cement and Concrete Research*, 2010. **40**(12): p. 1673-1680.

48. Richardson, I., A. Brough, G. Groves and C. Dobson, The characterization of hardened alkali-activated blast-furnace slag pastes and the nature of the calcium silicate hydrate (CSH) phase. *Cement and Concrete Research*, 1994. **24**(5): p. 813-829.

6. Mechanical properties of alkali incorporated C-(A-)S-H

Presently most of the feasible approaches to the improvement of the microstructure of cementitious materials have already been implemented. Thus, for the improvement of mechanical properties and durability of cementitious materials, there is an urgent need to find scientific and technically-viable improvements at the atomic and nano scales. Improving the nanomechanical properties of the principal binding phase of cementitious materials, namely calcium (alumino) silicate hydrate (C-(A-)S-H) is one of the most promising approaches. High-pressure X-ray diffraction (HP-XRD) is a powerful technique to determine the mechanical properties of cement-related phases at molecular to nano scale [1]. The influences of Ca/Si molar ratio, and cross-linking sites on the nanomechanical properties of C-(A-)S-H have been investigated. Yet, the influence of alkali incorporation on the nanomechanical properties of C-(A-)S-H has not been studied. In this chapter, the nanomechanical properties of alkali incorporated C-(A-)S-H is unveiled using HP-XRD under hydrostatic pressure. The results are used to validate the existing molecular model of alkali incorporated C-(A-)S-H.

6.1 HP-XRD of alkali incorporated C-(A-)S-H

Figure 6.1 presents powder diffractograms of sodium incorporated C-S-H (C-N-S-H) and sodium incorporated C-A-S-H (C-N-A-S-H) at each point of hydrostatic pressure. Parameters of unit cells of C-N-S-H and C-N-A-S-H are fitted with tobermorite monoclinic B1Im space group at different pressures. The samples measured at ambient pressure were filled in glass capillaries without any external load. The fitted lattice parameters of both phases at ambient pressure are listed in Table 6.1. At ambient pressure, the basal spacing ((002) reflection) of C-N-S-H is 12.28 Å, which is smaller than that of water-cured C-S-H ($d_{(002)}=12.63\text{Å}$) at Ca/Si=1 synthesized under the same conditions [2]. The reduced basal spacing can be partially attributed to the substitution of interlayer Ca^{2+} and $\text{Ca}(\text{OH})^+$ by Na^+ since the hydrated Na^+ ion is 0.5 Å smaller than hydrated Ca^{2+} in radius. The substitution of Ca^{2+} and $\text{Ca}(\text{OH})^+$ by Na^+ favors the re-organization of calcium silicate basal layer, namely more available Ca for the formation of CaO7 sheet. Thus, the (002) peak in C-N-S-H is sharper and more intense than water-cured C-S-H at equilibrium temperature of 50 °C [2], suggesting a higher range of ordering along the c-axis of C-N-S-H relative to C-S-H at the same equilibrium temperature. The reduced basal spacing and increased long-range order of (002) of C-N-A-S-H relative to C-A-S-H at ambient pressure can be also explained by the same mechanisms. The highly ordered C-N-S-H and C-N-A-S-H along the c-axis relative to water-cured C-(A-)S-H favor higher range of pressure (up to 10 GPa) in this study since pressure-induced disordering of structure significantly lowers the intensity and sharpness of (002), which leads to large errors of c length and bulk modulus in water-cured C-(A-)S-H [1]. The unlabeled peaks are mainly weak reflections of C-N-(A-)S-H or peaks of ruby, steel gasket, and secondary product katoite ($\text{Ca}_3\text{Al}_2(\text{OH})_{12}$).

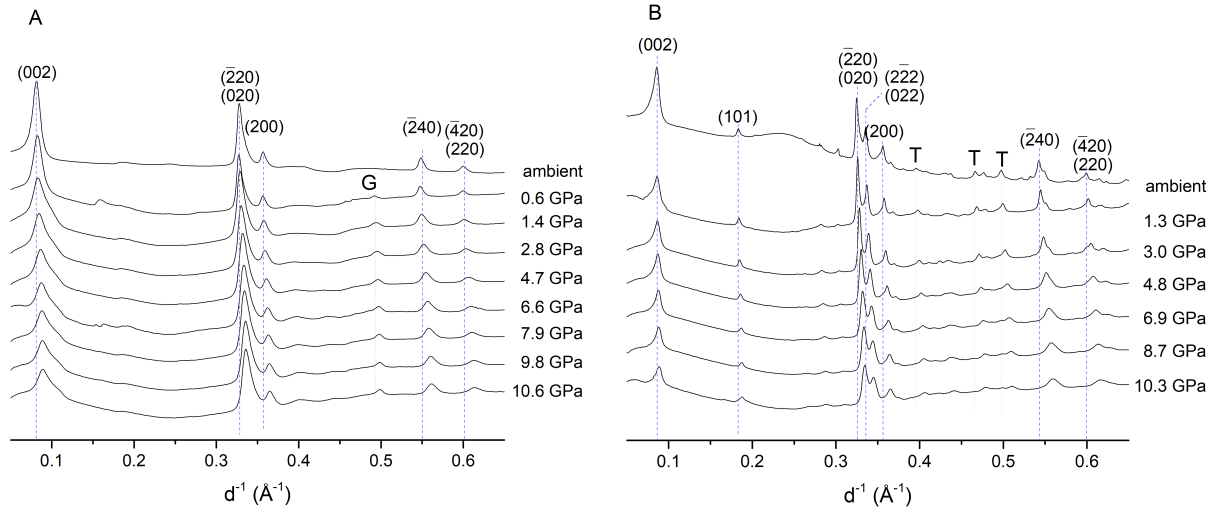


Figure 6.1. X-ray diffractograms of (A) C-N-S-H (Ca/Si=1) and (B) C-N-A-S-H (Ca/Si=1, Al/Si=0.1) up to ~10 GPa. Vertical blue dashed lines correspond to the C-N-(A-)S-H peak positions at ambient pressure. The uncertainty of determined pressure in (A) and (B) was ~0.15 GPa. G: gasket and T: thermonatrite. Ruby spheres were not on the beam path.

Table 6.1 Rietveld refinement of lattice parameters (a , b , c , and γ) at ambient pressure. The uncertainties of the lattice parameters are determined as 0.01 Å for a , b , and c , and 0.1° for γ .

	Ca/Si	Al/Si	a (Å)	b (Å)	c (Å)	γ	V (Å ³)
C-N-S-H	1	0	6.695(9)	7.288(9)	24.55(8)	122.98(9)	1005(6)
C-N-A-S-H	1	0.1	6.717(5)	7.368(8)	23.27(5)	123.26(8)	963(3)

At elevated hydrostatic pressure (measured by a ruby fluorescence system), the absolute intensity of all peaks of the samples decreased, and peak broadening was observed. This peak broadening phenomenon is due to the increasing disorder of lattice structures induced by stress under high-pressure [3], which is commonly observed in HP-XRD measurements. Monotonically increasing peak positions were observed with increasing hydrostatic pressure since the lattice structures were compressed along all directions. This shift in peak positions corresponds to a reduction in the interplanar distance, namely increasing $1/d$ of reflection peaks. Reflections of (002), (-220), (020), (200), (-240), (-420), and (220) from monoclinic 11 Å tobermorite were selected to determine the lattice parameters of both samples, and (-222) and (022) for C-N-A-S-H only. Lattice parameter γ of the unit cell of C-N-S-H was relatively constant under pressure up to 10 GPa, suggesting no distortion on its ab -plane. However, γ of C-N-A-S-H slightly decreased with increased hydrostatic pressure, indicating the ab -planar distortion.

Biot strain along each lattice direction with increased hydrostatic pressure is shown in Figure 6.2. The Biot strain was calculated as $(L-L_0)/L_0$, where L and L_0 are the lattice parameters along each direction at loaded and ambient pressures, respectively. The incompressibility along each lattice direction is defined as the slope of Biot strain as a function of hydrostatic pressure. The a - and b -axes monotonically contract with increased pressure up to ~10 GPa. Despite the fact that C-N-A-

S-H is more long-range ordered along the c-axis relative to C-N-S-H, the incompressibility of ab-plane of C-N-S-H and C-N-A-S-H are approximately $-1/450 \text{ GPa}^{-1}$ and $-1/330 \text{ GPa}^{-1}$, respectively, suggesting a significantly higher ab-planar incompressibility compared to all water-cured C-(A-)S-H and tobermorite [4] [5] [6], which were measured using the same method at the same beamline. The axes incompressibility and volume incompressibility in the present study and previous studies are compared in Table 6.2. Although the number of vacancies at bridging sites in C-S-H at different Ca/Si ratios and Al incorporations are variable, measured ab-planar incompressibility of C-(A-)S-H ranges from $-1/253$ to $-1/324 \text{ GPa}^{-1}$.

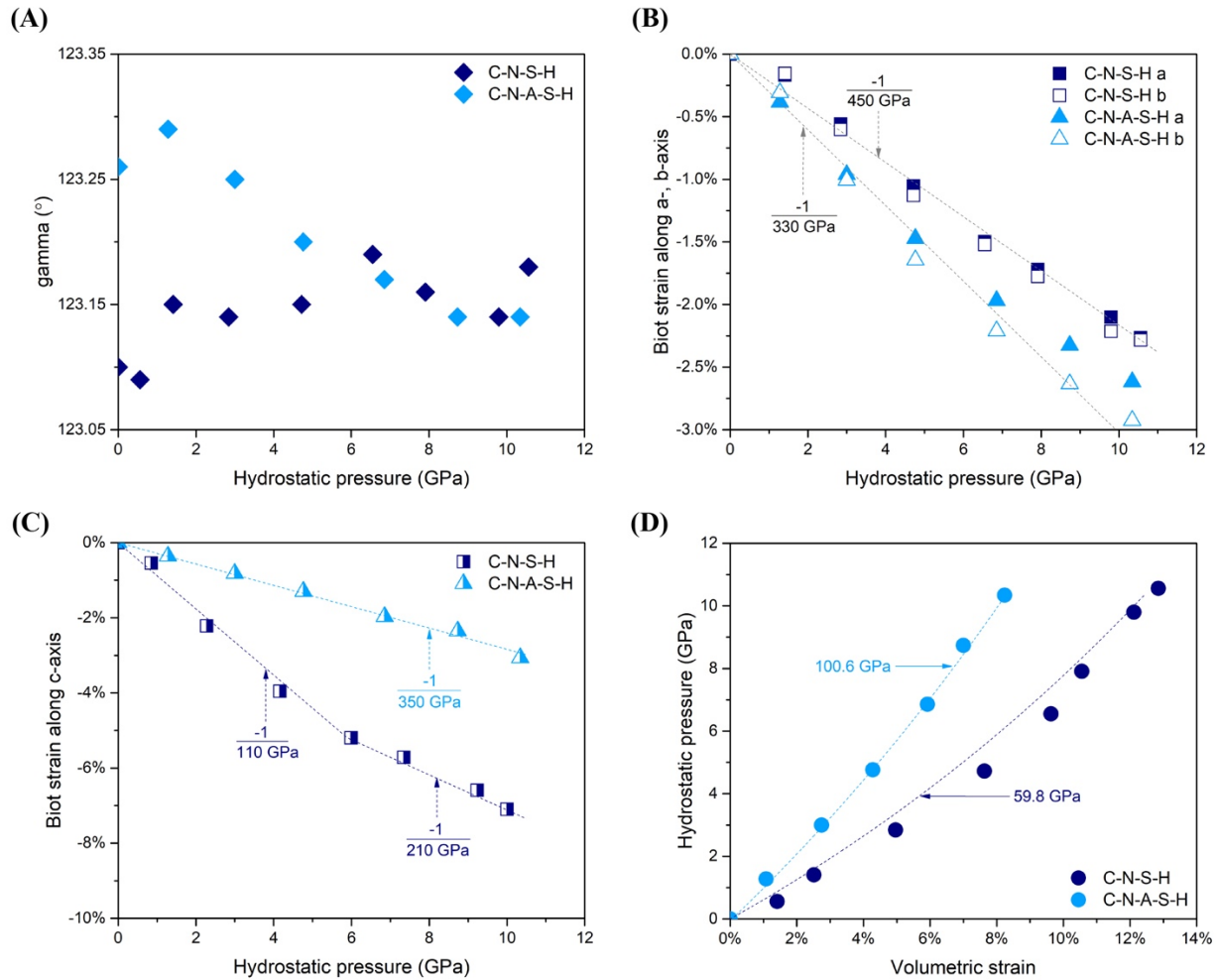


Figure 6.2. The mechanical response of C-N-(A-)S-H to hydrostatic pressure. (A) γ of unit cell. (B) Biot strains along the a- and b- axis. (C) Biot strain along the c-axis are plotted as functions of hydrostatic pressure. The slopes of the dashed lines, incompressibility, along each axis are indicated in the plot. In (C), the c-axis of C-N-S-H can be fitted with two linear trendlines, with an inflection point at $\sim 5 \text{ GPa}$, whereas the c-axis of C-N-A-S-H can be fitted with one linear trendline. (D) Volumetric strain as a function of hydrostatic pressure. The fitted second order BM-EoS is illustrated by dashed lines, and the fitted initial bulk moduli K_0 are indicated. In Figure 3C, the coefficient of determination R^2 of the fitting of the second order BM-EoS is above 0.99 with standard error of 2 GPa. The uncertainty of determined pressure in (A)-(D) is $\sim 0.15 \text{ GPa}$.

Table 6.2 Incompressibility of the a-, b-, and c-axes and bulk modulus K_0 of C-(A-)S-H and tobermorite in previous and the present studies.

	Ca/(Al+Si)	Al/(Al+Si)	Equilibrium		$d_{(002)}$ (Å)	Inverse of incompressibility along (GPa^{-1})			K_0 (GPa) ^a
			Temperature	Day		a-axis	b-axis	c-axis	
Non-cross-linked									
C-N-S-H	1.0	-	50 °C	56	12.28	-426	-413	-110, -210 ^b	60
C-S-H (Ca/Si=0.8)	0.8	-	20 °C	182	14.45	-287	-324	-100, -170 ^b	58
C-S-H (Ca/Si=1.0)	1.0	-	20 °C	182	11.05	-283	-303	-160, -280 ^b	69
C-S-H (Ca/Si=1.4)	1.4	-	20 °C	182	9.95	-298	-289	-200, -310 ^b	77
C-S-H (Ca/Si=0.97)	0.97	-	-	-	12.7	-253	-263	-52	34
C-S-H (Ca/Si=1.0)	1.0	-	80 °C	56	13.8	-283	-301	-71, -166 ^b	36
C-S-H (Ca/Si=1.0)	1.0	-	80 °C	56	12.2	-283	-301	-134	50
14 Å Tobermorite	0.83	-	-	-	14.0	-257	-355	-89	47
Cross-linked									
C-N-A-S-H (Al/Si = 0.1)	0.91	0.091	50 °C	56	11.63	-370	-331	-352	101
C-A-S-H (Al/Si=0.05)	0.95	0.048	80 °C	56	11.55	-299	-304	-197	64
C-A-S-H (Al/Si=0.1)	0.91	0.091	80 °C	56	11.45	-285	-281	-263	71
11 Å Normal Tobermorite	0.77	0.074	-	-	11.35	-306	-316	-159	71
11 Å Anomalous Tobermorite	0.67	-	-	-	11.40	-226	-290	-202	63
11 Å Al-Tobermorite	0.8	0.165	-	-	11.44	-276	-269	-129	55

^a Measured K_0 were all fitted using second-order BM-EoS (see Equations 3.1 and 3.2).

^b The first and second values are the inverse of incompressibility before and after, respectively, the inflection points of the trendlines.

The Na-uptake induced ab-planar stiffening in C-N-(A-)S-H indicated a structural change in the (alumino)silicate chains. This result can be explained through partial replacement of one interlayer Ca^{2+} in water-cured C-S-H with two Na^+ in C-N-S-H and C-N-A-S-H and the partial replacement of one interlayer $\text{Ca}(\text{OH})^+$ with another Na^+ in C-N-S-H and C-N-A-S-H. Compared to water-cured C-S-H and C-A-S-H at constant Ca/(Al+Si) ratio, the replaced interlayer Ca^{2+} and $\text{Ca}(\text{OH})^+$ by Na^+ induce a higher Ca fraction of the calcium silicate basal layer, leading to a shorter silicate chain (more dimers and more chain ends) on the CaO_7 ab-plane, as evidenced by previous ^{29}Si NMR characterization [7]. The shielding of Si by Na is weaker than by Ca, resulting a reorganization of Si environment, e.g., Si-O-Si bonds.

The lower ab-planar incompressibility of C-N-A-S-H relative to C-N-S-H can be explained by the Al incorporation, which induced more bridging and cross-linking sites, thus reducing the number of chain-end to be charge-balanced by Na [7]. The change in Si environment of C-(A-)S-H by alkali incorporation was evidenced by considerably change in chemical shift in previous ^{29}Si NMR studies [7] [8].

Biot strain along the c-axis of C-N-S-H can be fitted using two linear trendlines (at the slope of $-1/90 \text{ GPa}^{-1}$ and $-1/221 \text{ GPa}^{-1}$) with an inflection point at $\sim 5 \text{ GPa}$ (Figure. 6.2C), suggesting a stiffening trend along the c-axis. A similar stiffening trend was also observed for non-cross-linked C-S-H synthesized at 20 °C and 80 °C, which was accompanied by inflection points at 2-5 GPa [5] [6]. The incompressibility along the c-axis in the high-pressure linear region is $\sim 60\%$ higher compared to the ambient incompressibility. Along the entire pressure range, the c-axis of

C-N-S-H is softer than its a- and b- axes, since no cross-linking sites exist to resist the deformation along c-axis [7]. Thus, the nanomechanical properties of non-cross-linked C-N-S-H are governed by the pressure-induced stiffening along the c-axis (mainly due to the less dense interlayer instead of intralayer), which is also the case for all previously studied C-S-H samples and non-cross-linked 14 Å tobermorite [5] [6] [4]. Note that the pressure range (2-5 GPa) of variation in incompressibility in the c-axis is significantly higher than the typical uniaxial compressive strength of cementitious materials (i.e., 0.2 GPa). The incompressibility along the c-axis in the high-pressure range may not be relevant to the application of C-(N-)(A-)S-H based cementitious materials.

Whereas the incompressibility of C-N-A-S-H along the c-axis can be fitted using only one trendline at a slope of $-1/352 \text{ GPa}^{-1}$, such high incompressibility along the c-axis is attributed to the resistance given from cross-linking sites, which is also the case for cross-linked C-A-S-H samples. The incompressibility along c-axis of C-N-A-S-H is comparable to that along its a- and b- axes, indicated that C-N-A-S-H is nearly isotropic. This phenomenon is in good agreement with the mechanical behaviors of alkali-free (water-cured) C-(A-)S-H at 80 °C measured by HP-XRD and simulation [6] [9].

When comparing the C-N-A-S-H and C-A-S-H samples both at bulk Al/Si = 0.1 and Ca/Si = 1.0, an abnormal mechanical behavior is observed. The incompressibility of C-N-A-S-H is higher than C-A-S-H ($-1/352 \text{ GPa}^{-1}$ versus $-1/263 \text{ GPa}^{-1}$, respectively) along c-axis, despite the fact that C-N-A-S-H has fewer cross-linked tetrahedra (7.9% versus 21.7%, respectively) and a larger basal spacing (11.63 Å versus 11.45 Å, respectively). This is surprising because more cross-linked sites and lower basal spacings are associated with higher incompressibilities [5] [6] [4]. This strange behavior suggests that additional inclusions in the interlayer of C-N-A-S-H stiffen it along the c-axis. Note that only 91% of bulk Al in the raw materials is incorporated on silicate chains of C-N-A-S-H [7]. The species and location of the other 9% of bulk Al are controversial: Myers et al. suggested that Al₅ are likely incorporated in the interlayer [10] while Al₆ may occur as a separate phase (so-called third aluminate hydrate (TAH); the first and second aluminates are ettringite and monosulfoaluminate hydrate, respectively) [11]. As outlined in the previous chapter. The TAH is either not Ca-bearing or its Ca is structurally similar to the synthetic C-(A-)S-H. The hydrated ion radius of Al is $\sim 4.75 \text{ Å}$, which is much larger than hydrated Ca⁺ and Na⁺, meaning that the interlayer is less dense with Al in the interlayer. And the amount of interlayer Al is very limited (<1% of Si content), thus such considerable stiffening is unlikely be explained by the incorporation of Al in the interlayer. This increased incompressibility of C-N-A-S-H along the c-axis is assigned to the incorporation of hydrated Na⁺ ions in its interlayer, where more zeolitic content is filled relative to C-A-S-H, e.g., two hydrated Na⁺ ions may partially replace a zeolitic Ca²⁺ in the presence of NaOH solution (see Figure 6.3).

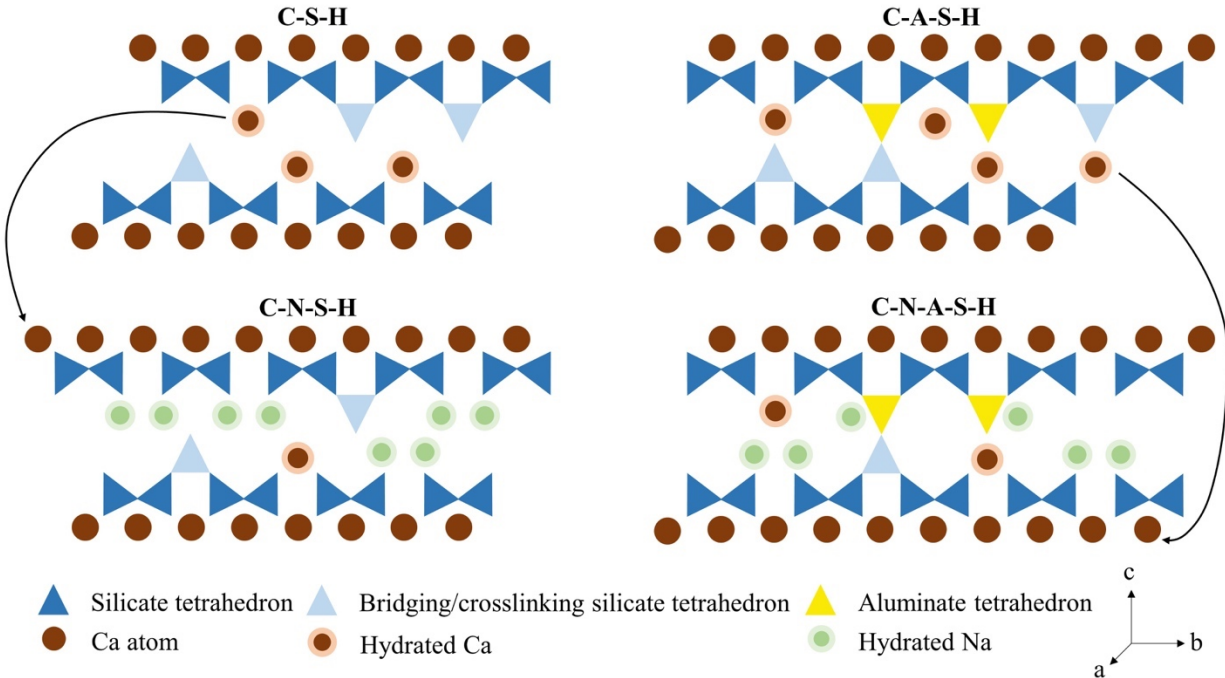


Figure 6.3. Schematic redistribution of charge balanced Ca^{2+} and/or $\text{Ca}(\text{OH})^+$ (shaded brown circles) from the interlayer to the CaO_7 intralayer (solid brown circle) in C-N-S-H and C-N-A-S-H. Dark blue and light blue triangles represent paired and bridging tetrahedral sites respectively, and yellow triangles represent aluminum incorporated tetrahedral sites. Shaded green circles are hydrated Na^+ ions. Some O atoms at silicate tetrahedra are also charge-balanced by H^+ (not shown in the figure).

The experimentally determined K_0 of C-N-S-H and C-N-A-S-H are 59.8 ± 2 GPa and 100.6 ± 2 GPa, respectively, using the second-order BM-EoS, and are 42.1 ± 5 GPa and 97.6 ± 7 GPa, respectively, using the third-order BM-EoS. The mean chain lengths of C-N-S-H and C-N-A-S-H were shorter than alkali-free C-(A-)S-H [7] [12] while the K_0 of alkali-incorporated C-(A-)S-H phases are higher than alkali-free C-(A-)S-H (see Figure 6.4). The correlation between K_0 and mean chain length suggested that “defect-driven” hypothesis, which claims mechanical properties of C-S-H increases with longer range order of silicate chain [5], is implausible, consistent with findings from the previous study.

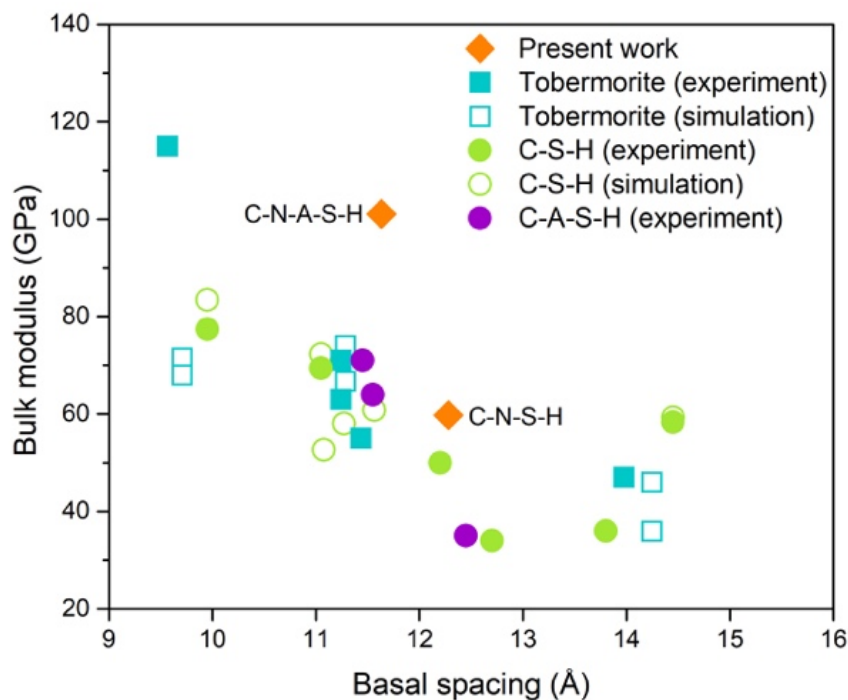


Figure 6.4. Correlation between basal spacing ($d_{(002)}$) and initial bulk modulus (K_0) of tobermorite, Al-tobermorite, C-(A-)S-H [5] [6] [2] [4], and C-N-(A-)S-H in the present study. All measured K_0 values were fitted using the second order BM-EoS (Equation 3.2).

Puertas et al. simulated the mechanical properties of C-N-(A-)S-H using defected 11 Å and 14 Å tobermorite models [13]. The simulated K_0 of C-(N-)A-S-H with (alumino)silicate chain lengths of 2 and 5-11 using defected 14 Å tobermorite model (non-cross-linked) were 26 GPa and 35-41 GPa, respectively. The simulated K_0 is significantly lower than the measured K_0 of non-cross-linked C-N-S-H, 42-59 GPa, with mean chain length (MCL) of ~ 3 in the present study, namely C-N-S-H herein is mainly a mixture of dimers (MCL = 2) and pentamers (MCL = 5).

A large deviation between experiment and this simulation was also found for C-N-A-S-H. The simulated K_0 of C-N-A-S-H with (alumino)silicate chain lengths of 2 and 5-11 using defected 11 Å tobermorite (cross-linked) were 22 GPa and 55-68 GPa, respectively. The simulated K_0 was significantly lower than our experimental value of C-N-A-S-H, which is a mixture of cross-linked and non-cross-linked structures with MCL of ~ 7 .

The potential set used in Puertas et al. [13] was derived from crystalline C-S-H phases with additional potential set of Na and Al from zeolite; the force field method is very sensitive to partial charge values. The large deviation between simulated and experimental results indicate that the potential set of Na and Al is not suitable for C-N-(A-)S-H. Using charge-balancing mechanism and non-cross-linked 14 Å tobermorite model, Ozcelik and White [14] predicted that K_0 of C-N-S-H slightly decreased from 54 GPa to 52 GPa through the substitution of a Ca^{2+} by a Na^+ and a H^+ , which was explained by the comparable local charge density between C-S-H and C-N-S-H. The predicted value is comparable to our experimental result of C-N-S-H. However, the predicted increase in K_0 of C-N-A-S-H from C-N-S-H was only 14 GPa, which is much

lower than our experimental difference ~ 41 GPa. This large deviation is attributed to the omission of cross-linking sites and possibly also the interlayer Al species in C-N-A-S-H structure in the simulation study. Their relaxed basal spacing of C-N-A-S-H using 14 Å tobermorite model was still ~ 14 Å. However, the interlayer of our cross-linked C-N-A-S-H was significantly denser, with basal spacing of 11.6 Å.

Note that in both simulation studies [13] [14], Al-uptake only occurred at cross-linked and/or bridging sites, Na only charge balanced bridging sites and dangling O of silicate chains were bonded with H. However, the measured amount of incorporated Na in our C-N-A-S-H samples is significantly higher, with Na/Al ratio of ~ 3 , and dangling O can be bonded with Na herein [7] [8]. Thus, the high value of K_0 of C-N-A-S-H measured by HP-XRD can be significantly attributed to steric constraints of interlayer by Na incorporation, and possibly interlayer Al species, in addition to the columnar resistance from cross-linking sites.

An inverse correlation between bulk moduli and basal spacing of water-cured C-(A-)S-H is generally agreed in Figure 6.4. However, C-N-S-H seems not to fall in the basal spacing- K_0 trendline. The measured K_0 of 59.8 GPa for C-N-S-H with basal spacing of 12.28 Å is higher than 50 GPa of C-S-H with basal spacing of 12.2 Å. Dharmawardhana et al. [15] suggested that the mechanical properties of C-(A-)S-H is significantly influenced by zeolitic content, e.g., interlayer Ca and water. This can explain the lower K_0 of anomalous cross-linked 11 Å tobermorite relative to normal cross-linked 11 Å tobermorite, since anomalous tobermorite contains less zeolitic Ca than the normal [16]. Likewise, despite similar basal spacing of C-N-A-S-H relative to 11 Å tobermorite, cross-linked C-N-A-S-H with more interlayer Al species, zeolitic Na and water exhibited a higher bulk modulus. Further studies are needed to verify the reinforcing effect of Al species alone (Al6 and/or Al5) in the interlayer. C-A-S-H samples equilibrated at 7 °C -50 °C do not have any cross-linking sites, four-fold coordinated Al can be incorporated in the silicate chain and the rest Al (Al6 and/or Al5) can be possibly in the interlayer.

6.2 Conclusions

This chapter studied the mechanical behaviors of nano-crystalline C-N-(A-)S-H under hydrostatic pressure using HP-XRD. The experiments probed the lattice deformation of C-N-S-H and C-N-A-S-H and obtained their mechanical properties at molecular-to-nano scale. The study validated existing computational models of C-N-(A-)S-H and provided fundamental knowledge to the understanding of the structure of alkali-incorporated C-(A-)S-H. The results can be used to build more realistic models of these phases at atomistic-to-nano scales and to provide critical information to design C-S-H based materials through a bottom-up approach.

Na-incorporated C-(A-)S-H does not fully fall into the inverse K_0 - $d_{(002)}$ trendline in C-S-H. Na incorporation slightly enhances the mechanical properties of C-S-H by increasing the zeolitic content in the interlayer. Despite that the high pH environment leads to more vacancies at bridging sites along (alumino)silicate chains, the measured the ab-planar incompressibility of C-N-(A-)S-H is not reduced compared to alkali-free C-(A-)S-H and tobermorite. Instead, the partial substitution of interlayer Ca^{2+} and $\text{Ca}(\text{OH})^+$ by Na^+ ions stiffens the ab-plane. The reported mechanical behaviors of C-N-(A-)S-H herein therefore do not agree with defect-driven

hypothesis. Cross-linking is observed in C-N-A-S-H, which leads to a comparable basal spacing to 11 Å tobermorite. The aluminate and silicate cross-linked sites provide resistance to hydrostatic compression along the c-axis, which increases the incompressibility of cross-linked C-N-A-S-H relative to non-cross-linked C-N-S-H along the c-axis. The bulk modulus of cross-linked C-N-A-S-H (Ca/Si=1, Al/Si=0.1) synthesized at 50 °C is 30 GPa higher than that reported for cross-linked tobermorite minerals.

The effects of Na and Al on the mechanical properties of C-S-H studied in the present chapter provide valuable information to build new computational models. The significantly high incompressibility along the c-axis and bulk modulus of cross-linked C-N-A-S-H may be crucial in designing alkali-activated materials and other C-(A-)S-H-based cementitious materials using a ‘bottom-up’ approach.

6.3 References

1. Oh, J.E., S.M. Clark and P.J.M. Monteiro, Does the Al substitution in C-S-H(I) change its mechanical property? *Cement and Concrete Research*, 2011. **41**(1): p. 102-106.
2. Li, J., G. Geng, R.J. Myers and Y.-S.S. Yu, David A; Carraro, Carlo; Maboudian, Roya; Monteiro, Paulo J.M. , The chemistry and structure of calcium (alumino) silicate hydrate: A Study by XANES, ptychographic imaging, and wide- and small- angle scattering. *Cement and Concrete Research*, 2019.
3. Wenk, H.R., L. Lutterotti and S.C. Vogel, Rietveld texture analysis from TOF neutron diffraction data. *Powder Diffraction*, 2010. **25**(3): p. 283-296.
4. Oh, J.E., S.M. Clark, H.R. Wenk and P.J.M. Monteiro, Experimental determination of bulk modulus of 14 angstrom tobermorite using high pressure synchrotron X-ray diffraction. *Cement and Concrete Research*, 2012. **42**(2): p. 397-403.
5. Geng, G.Q., R.J. Myers, M.J.A. Qomi and P.J.M. Monteiro, Densification of the interlayer spacing governs the nanomechanical properties of calcium-silicate-hydrate. *Scientific Reports*, 2017. **7**.
6. Geng, G., R.J. Myers, J. Li, R. Maboudian, C. Carraro, D.A. Shapiro and P.J. Monteiro, Aluminum-induced dreierketten chain cross-links increase the mechanical properties of nanocrystalline calcium aluminosilicate hydrate. *Scientific Reports*, 2017. **7**: p. 44032.
7. Myers, R.J., E. L'Hopital, J.L. Provis and B. Lothenbach, Composition-solubility-structure relationships in calcium (alkali) aluminosilicate hydrate (C-(N,K-)A-S-H). *Dalton Transactions*, 2015. **44**(30): p. 13530-13544.
8. L'Hôpital, E., B. Lothenbach, K. Scrivener and D. Kulik, Alkali uptake in calcium alumina silicate hydrate (CASH). *Cement and Concrete Research*, 2016. **85**: p. 122-136.
9. Yang, J., D. Hou and Q. Ding, Structure, dynamics and mechanical properties of cross-linked calcium aluminosilicate hydrate: a molecular dynamics study. *ACS Sustainable Chemistry & Engineering*, 2018.
10. Myers, R.J., G. Geng, J. Li, E.D. Rodriguez, J.Y. Ha, P. Kidkhunthod, G. Sposito, L.N. Lammers, A.P. Kirchheim and P.J.M. Monteiro, Role of adsorption phenomena in cubic tricalcium aluminate dissolution. *Langmuir*, 2017. **33**(1): p. 45-55.
11. Andersen, M.D., H.J. Jakobsen and J. Skibsted, A new aluminium-hydrate species in hydrated Portland cements characterized by ²⁷Al and ²⁹Si MAS NMR spectroscopy. *Cement and Concrete Research*, 2006. **36**(1): p. 3-17.

12. Myers, R.J., E. L'Hopital, J.L. Provis and B. Lothenbach, Effect of temperature and aluminium on calcium (alumino)silicate hydrate chemistry under equilibrium conditions. *Cement and Concrete Research*, 2015. **68**: p. 83-93.
13. Puertas, F., M. Palacios, H. Manzano, J.S. Dolado, A. Rico and J. Rodriguez, A model for the C-A-S-H gel formed in alkali-activated slag cements. *Journal of the European Ceramic Society*, 2011. **31**(12): p. 2043-2056.
14. Ozcelik, V.O. and C.E. White, Nanoscale charge-balancing mechanism in alkali-substituted calcium-silicate-hydrate gels. *Journal of Physical Chemistry Letters*, 2016. **7**(24): p. 5266-5272.
15. Dharmawardhana, C.C., A. Misra, S. Aryal, P. Rulis and W.Y. Ching, Role of interatomic bonding in the mechanical anisotropy and interlayer cohesion of CSH crystals. *Cement and Concrete Research*, 2013. **52**: p. 123-130.
16. Moon, J.H., J.E. Oh, M. Balonis, F.P. Glasser, S.M. Clark and P.J.M. Monteiro, Pressure induced reactions amongst calcium aluminate hydrate phases. *Cement and Concrete Research*, 2011. **41**(6): p. 571-578.

7. Concluding Remarks

In this thesis, multiple synchrotron-radiation-based X-ray techniques were applied to study C-S-H based cementitious materials and synthetic C-S-H based products. The experimental studies include 1) the hydration of two C_2S polymorphs at different curing ages and the degree of silicate polymerization of C-S-H in the two hydration systems; 2) the atomic structure of synthetic calcium (alumino) silicate hydrate (C-(A-)S-H) products and the morphology of C-(A-)S-H at the microscale; and 3) the structure-mechanical property correlation of alkali incorporated C-(A-)S-H at the nanoscale. These experimental studies are essential to the designing of C-S-H based green cementitious materials, because: A) the degree of silicate polymerization of C-S-H is relevant to the resistance to carbonation and chemical attacks; B) the morphology of C-(A-)S-H correlates the durability and physical and mechanical properties of cementitious materials; and C) the nanomechanical properties of C-(A-)S-H may influence the mechanical properties of cementitious materials at the micro-to-macro scale. In addition to the experimental results and the detailed discussions presented in chapters 4-6, the most significant conclusions are listed.

1. The Ca coordination of C-S-H in both β - C_2S and α'_H - C_2S hydration system is highly distorted and is similar to 14 Å tobermorite but have a shorter-range ordering. More six-fold coordinated Ca occur in hydrated α'_H - C_2S than in hydrated β - C_2S . The Si of both anhydrous phases have asymmetric tetrahedral coordination. The silicate chain of the outer product in both hydration systems polymerizes over time. The hydration products in the α'_H - C_2S system polymerize faster than in β - C_2S . Inner product has a lower degree of silicate polymerization than outer product in fully hydrated β - C_2S , which is accompanied by a slightly longer Si-O bond. Compared with hydrated β - C_2S , the silicate polymerization in hydrated α'_H - C_2S is more homogeneous. The C-S-H of hydrated β - C_2S exhibits fine fibrils that intermix with portlandite, and Ip appears to be a dense aggregated structure. The morphology of fully hydrated α'_H - C_2S is more homogeneous, and its inner region is slightly more porous with nanovoids. Ip and Op are not distinguished in fully hydrated α'_H - C_2S .

2. Calcium environments in synthetic C-(A-)S-H are similar to tobermorite. The coordination symmetry of Ca is highly distorted irrespective Ca/Si, Al uptake, and equilibration temperature. In addition to the seven-fold coordinated Ca in the intralayer of C-(A-)S-H, the extra Ca that enters the interlayer are more likely six-fold coordinated in a distorted octahedral symmetry. The ordering of the Ca environment increases as Al content and equilibration temperature increase. The Si K-edge shifts to higher energy with increased mean chain length of silicate chains. The energy separation between major and minor peak at the Si K-edge positively correlates with the degree of polymerization of its aluminosilicate chains. AFm-like species are not interstratified in the interlayer structure or precipitate on the external surface of C-A-S-H. TAH is either not Ca-bearing or its Ca is structurally similar to C-(A-)S-H. C-(A-)S-H formed at 7–50 °C all preferably presents crumpled foils with various lengths, and are independent of Ca/Si ratio. C-(A-)S-H equilibrated at 80 °C present coarser foils, and the foils are much thicker and longer with more Al inclusion.

3. Na incorporation slightly enhances the mechanical properties of C-(A-)S-H by increasing the zeolitic content (Ca^{2+} and $Ca(OH)^+$) in the interlayer. Despite that the high pH environment leads to more vacancies at bridging sites along (alumino)silicate chains, the measured the ab-planar

incompressibility of C-N-(A-)S-H is not reduced compared to C-(A-)S-H and tobermorite. The reported mechanical behaviors of C-N-(A-)S-H herein therefore do not agree with defect-driven hypothesis. Cross-linking is observed in C-N-A-S-H, which leads to a comparable basal spacing to 11 Å tobermorite. The aluminate and silicate cross-linked sites provide resistance to hydrostatic compression along the c-axis, which increases the incompressibility of cross-linked C-N-A-S-H relative to non-cross-linked C-N-S-H along the c-axis.

Based on the present studies, a few suggestions for the design of high performance green cementitious materials can be addressed: A) α' -C₂S instead of β -C₂S is proposed to be the major C₂S polymorph when preparing C₂S-rich cement since α' -C₂S polymerizes faster; B) Design C-S-H with higher degree of silicate polymerization by increasing curing temperature and by adding aluminosilicate sources; and C) Design high-strength cementitious materials using Al-rich SCMs with moderate Na content to form stiff cross-linking sites at high curing temperature. These suggestions may improve the mechanical properties of green cementitious materials and enhance their resistance to chemical attacks.

A few suggestions for future study can be proposed: A) Since belite is the main compound in belite-ye'elimite-ferrite cement, the influence of ye'elimite on the hydration of belite should be investigated. Hydration of ye'elimite in the presence of calcium sulfates also needs to be understood. B) The coordination environment of Al in C-A-S-H with different chemical compositions and at various equilibrium temperatures and the nature of TAH should be studied. C) Similar to sodium, potassium is also commonly found in Portland cement, SCM, and alkali activators, therefore, the influence of potassium on the structure and nanomechanical properties of C-(A-)S-H need to be understood using HP-XRD. The differential influences between K and Na on the nanomechanical properties of C-(A-)S-H need to be studied.

8. Appendix

8.1 Supplementary images and algorithm

For a better organization of the thesis, some analysis algorithm and additional images are described in this appendix.

Hydration of belite

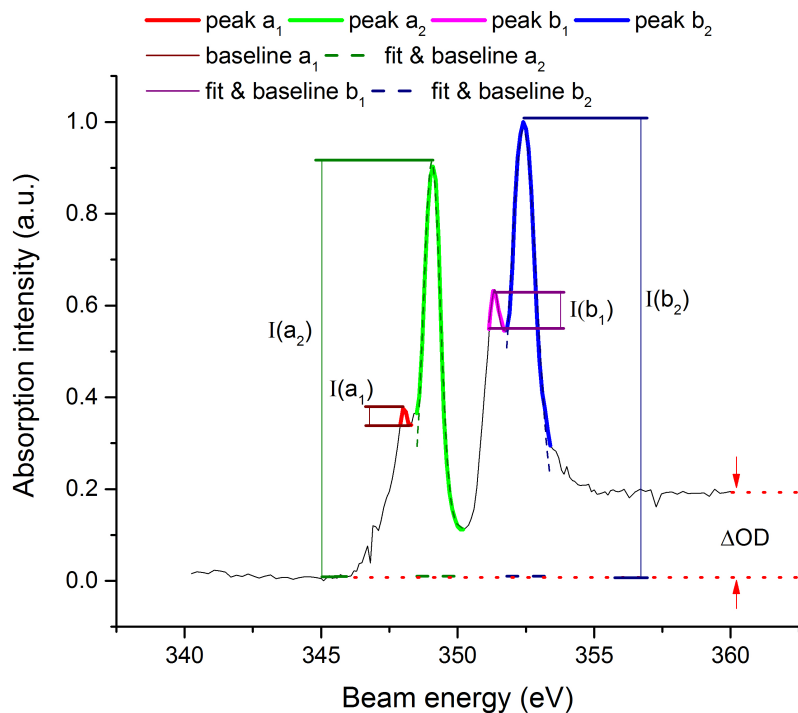


Figure S1. An example of fitting of different peaks in C-S-H in hydrated β -C₂S at 17 days (area 6 in Figure 4.1). The a₂, b₁, and b₂ peaks are taken by fitting a Gaussian shape function. The relative intensity of a₁ peak is manually selected due to the lack of data points for fitting. The relative intensity ratios are suggested to be evaluated at the same optical density difference (ΔOD) [1]. To our knowledge, the use of relative intensity ratios ($I(a_1)/I(a_2)$ and $I(b_1)/I(b_2)$) can minimize the influence of ΔOD or sample thickness and curvy shape of the backgrounds.

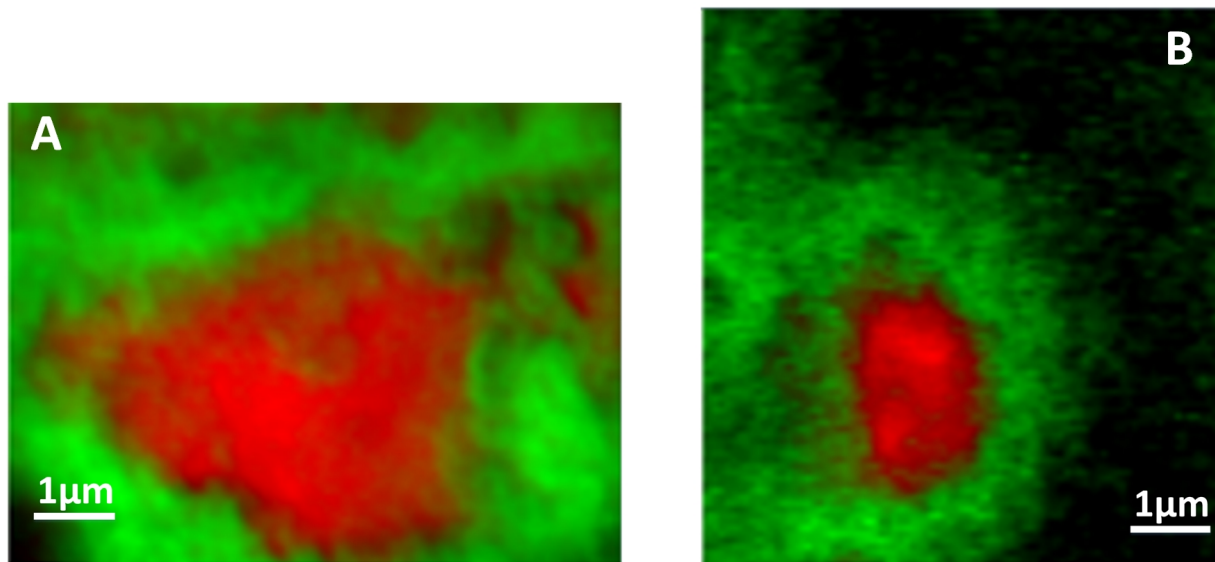


Figure S2. RGB overlay maps near Si K-edge (A) hydrated β -C₂S at 17 days; (B) hydrated α' _H-C₂S at 10 days. The green areas are obtained based on Si K-edge XANES spectrum of C-S-H and the red areas are obtained from reference spectra of (A) anhydrous β -C₂S and (B) anhydrous α' _H-C₂S.

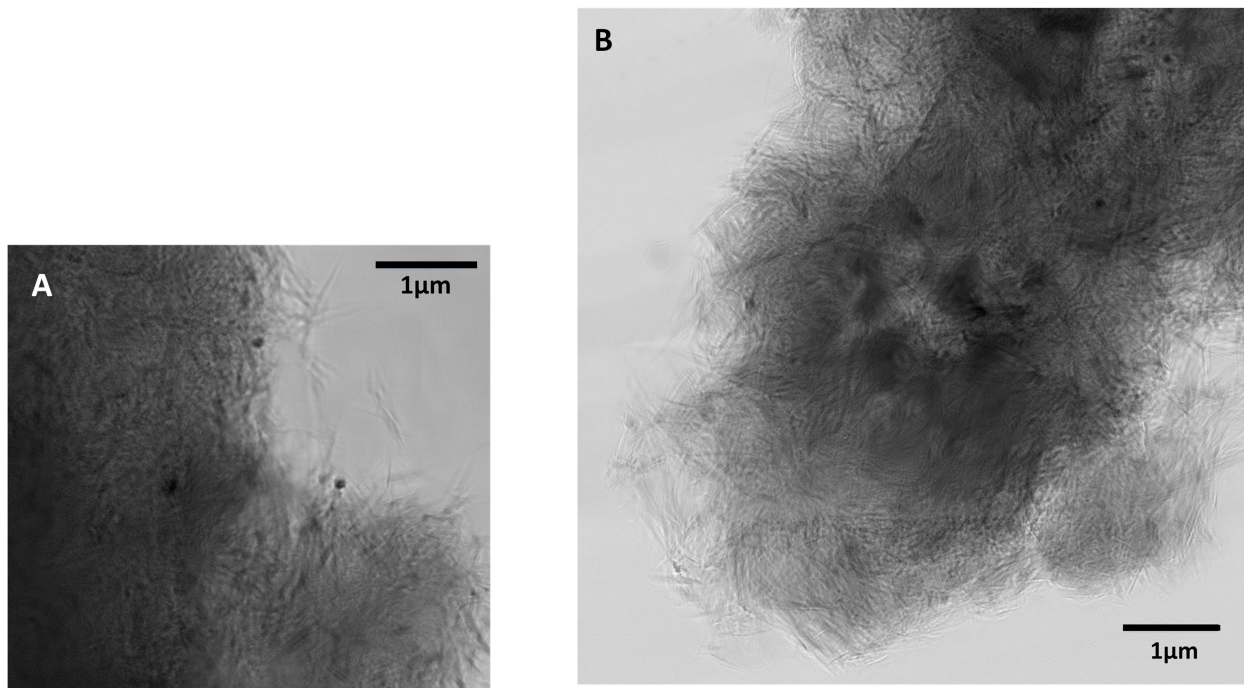


Figure S3. Ptychographic images. (A) hydrated β -C₂S cured for 51 days. (B) hydrated α' _H-C₂S at 40 days.

Nanostructure of C-(A-)S-H

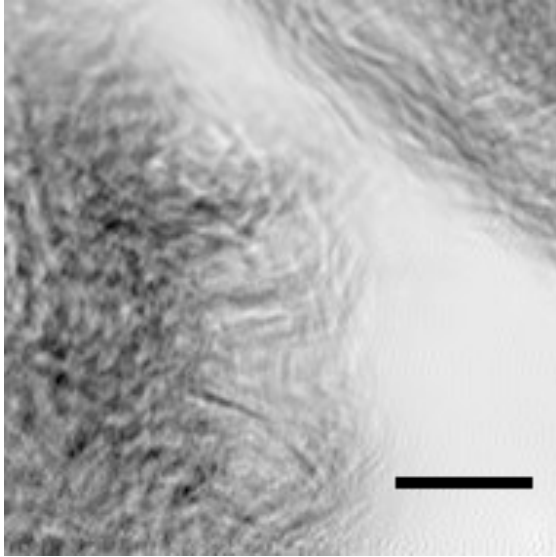


Figure S4. Ptychographic image C-A-S-H ($\text{Ca/Si}^* = 1.2$, $\text{Al/Si}^* = 0.05$, hydration of 182 days at 20°C) Scale bar is 500 nm. $\text{Ca/Si}^* = \text{bulk Ca/Si}$. $\text{Al/Si}^* = \text{bulk Al/Si}$

The calculation of small angle scattering (SAS) from transmission images has been successfully used to quantify morphological information. The algorithm used in the present work has been well-described in [2] and was applied to the ptychographic images. A lamellar Guinier-Porod model [3] was used to fit the calculated SAS. The fitting model contains a low- q Guinier region and a high- q linear Porod region, and the two regions intersect at q_1 :

$$I(q) = \frac{G}{q^s} \exp\left[-\frac{q^2 \times (d-s)}{2q_1^2}\right]; \text{ for } q \geq q_1 \quad (1)$$

$$I(q) = \frac{G}{q^d} \exp\left[-\frac{(d-s)}{2}\right] \times q_1^{(d-s)} \text{ for } q \leq q_1 \quad (2)$$

$$T = \frac{12^{0.5}}{q_1} \left[\frac{(d-s)(3-s)}{2}\right]^{0.5} \quad (3)$$

where q is the scattering variable; $I(q)$ is the scattered intensity; d is the Porod exponent; G is the Guinier scale factor; and T is the thickness of layered scattering materials. The parameter s , 2, is used to model lamellar objects in the case of C-(A-)S-H building blocks.

8.2 References

1. Geng, G., R.J. Myers, A.L. Kilcoyne, J. Ha and P.J. Monteiro, Ca L2, 3-edge near edge X-ray absorption fine structure of tricalcium aluminate, gypsum, and calcium (sulfo) aluminate hydrates. *American Mineralogist*, 2017. **102**(4): p. 900-908.

2. Geng, G., R.J. Myers, J. Li, R. Maboudian, C. Carraro, D.A. Shapiro and P.J. Monteiro, Aluminum-induced dreierketten chain cross-links increase the mechanical properties of nanocrystalline calcium aluminosilicate hydrate. *Scientific Reports*, 2017. **7**: p. 44032.
3. Hammouda, B., A new Guinier–Porod model. *Journal of Applied Crystallography*, 2010. **43**(4): p. 716-719.